Pre-stack Seismic Attribute Analysis of the Mississippian Chert and the Arbuckle Group at the Wellington Field, South-central Kansas

By

Yousuf Fadolalkarem
BSc Geophysics, University of Leeds, 2007

Advisory Committee

_____
George Tsoflias, Chairperson

_____
W. Lynn Watney, Committee member

_____
Ross Black, Committee member

Date Defended _____

The Thesis Committee for Yousuf Fadolalkarem certifies that this is the approved
version of the following thesis:

**Pre-stack Seismic Attribute Analysis of the Mississippian Chert and the
Arbuckle Group at the Wellington Field, South-central Kansas**

Advisory Committee

_____

George Tsoflias, Chairperson

_____

W. Lynn Watney, Committee
member

_____

Ross Black, Committee member

Date Approved: _____

ABSTRACT

At the Wellington Field, south-central Kansas, the Mississippian reservoir is a microporous cherty dolomite, and the deeper Cambrian-Ordovician Arbuckle Group is a thick succession of interbedded dolomudstones, pack-grainstones, vuggy brecciated zones, and thin dolomudstone and shale beds. The Mississippian chert reservoir and individual Arbuckle reservoir units are highly heterogeneous and typically below seismic resolution.

In this study I used 3D pre-stack depth migrated seismic data to map the main structural and stratigraphic features at the Mississippian and the Arbuckle reservoirs. A post-Mississippian normal fault that is striking NE-SW and dipping SE divides Wellington field diagonally into two parts. It cuts through the Mississippian and the Arbuckle Group down to the basement. The normal fault created accommodation space above the Mississippian chert reservoir in the southeastern part of the Wellington Field. The accommodation space allowed for depositing a layer that is thick enough to be resolved resulting in a localized double reflector in the seismic data.

Furthermore, I conducted a pre-stack seismic attribute analysis of the Mississippian chert reservoir and the Arbuckle Group to extend previous work done using post-stack seismic data. The good porosity zones in both the Mississippian and the Arbuckle Group exhibit Class IV AVO response. This AVO classification was employed to identify the porous zones in the Wellington Field 3D seismic volume using the AVO intercept-gradient crossplotting technique.

Simultaneous AVO inversion of pre-stack data showed better results than the model-based inversion of post-stack data for both the Mississippian reservoir and the Arbuckle Group. The inverted P-impedance by simultaneous AVO Inversion showed better correlation with the real P-impedance from well logs, and lower RMS inversion error. Also, Simultaneous AVO

Inversion resolved low impedance zones that were not resolved by post-stack model-based inversion. Thickness resolution limit of simultaneous AVO inversion within the Mississippian chert reservoir was determined using wedge modeling as 10 m, which corresponds to 1/8 of a wavelength. In the Arbuckle, the low impedance zones in the inverted P-impedance volume show good contrast with the surrounding higher impedance zones, which makes it easy to define and trace the low impedance zones around the Wellington Field.

In addition to the P-impedance, simultaneous AVO Inversion provided estimates of S-impedance and density, unlike the post-stack model-based inversion that inverts for P-impedance only. Inverted S-impedance was of good quality, but inverted density had the lowest recovery quality because density recovery depends mainly on the far offset data amplitude that can be easily distorted by noises.

For porosity prediction at Wellington, multi-attribute linear regression analysis employed attributes from simultaneous AVO inversion results and attributes from post-stack seismic data to derive multi-attribute transforms that are used to predict porosity. A multi-attribute transform derived within the Mississippian chert reservoir only provided reliable porosity prediction within the Mississippian chert reservoir, but it did not provide meaningful porosity values outside the Mississippian reservoir. Another multi-attribute transform derived within a larger window, between the top of the Cherokee Group and the top of Reagan Sandstone, provided valid porosity values around the Mississippian chert reservoir that helped in determining the top and the base of the reservoirs. This multi-attribute transform also provided the best porosity prediction for the Arbuckle Group.

Based on the estimated porosity volume and well data, the Mississippian reservoir thins to the northwest. The post-Mississippian normal fault is assumed to have lowered the

southeastern part of the Wellington field area that remained underwater, while the northwestern part of the Wellington field was exposed resulting in the thinning of the Mississippian reservoir by erosion, and the deposition of thicker reworked Mississippian chert. The Arbuckle Group has five main low impedance and high porosity zones that are deeper in the eastern and southeastern parts of the Wellington field. The depth change of the five zones in the Wellington field is attributed to the post-Mississippian normal fault.

ACKNOWLEDGMENTS

TABLE OF CONTENTS

LIST OF FIGURES AND TABLES

FIGURES

TABLES

CHAPTER 1: INTRODUCTION

Mississippian chert reservoirs, such as reservoirs at the Wellington Field in south-central Kansas, are highly heterogeneous, and unit thicknesses are typically below seismic resolution. In the Wellington Field, the Mississippian reservoir is microporous cherty dolomite reservoir that exhibits downward gradational porosity decrease resulting in a corresponding increase in velocity. The deeper Cambrian-Ordovician Arbuckle Group, however, is a thick succession of interbedded dolomudstones, pack-grainstones, vuggy brecciated zones, and thin dolomudstone and shale beds (Watney et al., 2013). The Arbuckle aquifers are highly heterogeneous and compartmentalized with individual reservoir units below seismic resolution. Therefore, it is challenging to identify reservoirs or predict their properties from the seismic data.

Post-stack seismic attribute analysis was employed at the Mississippian chert reservoir at the Wellington Field using well data and 3D pre-stack time migrated (PSTM) seismic data. Different analysis techniques were tested for the Mississippian reservoir characterization by Sirazhiev (2012). Post-stack seismic signal amplitude and frequency relationships with reservoir thickness were investigated. Raw seismic amplitude and amplitude envelope attributes taken at the peak of the Mississippian reflection could be used to predict the thickness of the reservoir in the southeastern part of the Wellington Field. However, the Mississippian cherty dolomite reservoir thins with high variability of porosity distribution to the North and Northwestern part of the Wellington Field. Also, the Mississippian reservoir in the northwestern region of the Wellington Field seismic survey shows higher amplitude and frequency content than the southeastern region. Neither amplitude nor frequency of the post-stack seismic data could be used for predicting the reservoir thickness in this part of the field. Synthetic seismic wedge modeling showed that seismic amplitude attributes provide reliable prediction of reservoir

thickness within the range of 5-25 m, underestimating thicknesses more than 25 m and not resolving thicknesses below 5 m. The resolvable thickness range 5-25 m corresponds to $1/16\lambda$-$5/16\lambda$.

Also, model-based inversion of the post-stack seismic data was performed to estimate the resolving power of post-stack model-based inversion at the Mississippian reservoir. Post-stack model-based inversion results in P-impedance volume only. The inverted P-impedance showed good correlation within the Mississippian reservoir with original P-impedance from the well logs. The inverted P-impedance volume was incorporated in the multi-attribute linear regression analysis described by Hampson et al. (2001) for porosity prediction. The resulting porosity model provided reliable porosity prediction within the Mississippian reservoir, but it was difficult at some places to delineate the top and base of the reservoir.

In this study I conduct pre-stack seismic attribute analysis of the Mississippian reservoir and the Arbuckle Group at the Wellington Field, south-central Kansas, using 3D pre-stack migrated seismic gathers. I examine pre-stack seismic attributes on both real and synthetic seismic data in order to find additional attributes that can help in identifying the porous reservoir zones, and to find out if using pre-stack seismic data for inversion and porosity prediction can improve the reservoir characterization.

This study investigates the AVO class response of the Mississippian reservoir and the porous zones of Arbuckle Group. I examine if the AVO classification can be used for identifying the porous zones around the Wellington Field in both the Mississippian and the Arbuckle. Also, I perform the simultaneous AVO inversion of the pre-stack migrated gathers that inverts for the P-impedance (Z_P), S-wave impedance (Z_S) and density (ρ) simultaneously, unlike the post-stack model-based inversion of post-stack seismic data that inverts for P-impedance only. The

2

resolving power of the resulting inversion volumes is evaluated by correlating the inversion results with real well log real data. Also, I compare the pre-stack simultaneous AVO inversion results and the post-stack model-based inversion results.

For porosity prediction, I incorporate inverted Z_P and Z_S by pre-stack simultaneous AVO inversion, formation porosity well logs and post-stack seismic data in the multi-attribute linear-regression analysis to derive multi-attribute transforms that are used to predict porosity values in the seismic survey volume of the Wellington Field. The reliability of porosity prediction is tested by blind wells that are excluded from the analysis. Also, the porosity prediction is evaluated by correlating predicted porosity traces with formation porosity well logs.

CHAPTER 2: FIELD SITE AND GEOLOGICAL SETTING

2.1: Field Site

The Wellington Field is part of the mature Midcontinent US petroleum province. It is located in Sumner County, south-central KS (Figure 2.1). The field was discovered in 1929. The field area is about 22.6 km^2. More than 250 wells were drilled in the Wellington Field. As of July 2014, the cumulative oil production from the Mississippian chert exceeded 20.7 million barrels of oil. The Wellington Field is experiencing a decrease in secondary production currently with 47 producing wells and 15 water injection wells (KGS, 2014).

2.2: Geological Setting

The local geology of the Wellington Field is composed of interbedded clastics and carbonates with distinct acoustic impedance changes that are favorable for subsurface imaging using seismic reflection. Good agreement is observed between synthetic and field seismic data as shown in Figure 2.2.

The Cambrian-Ordovician Arbuckle Group in Kansas is composed of shallow-shelf dolomite with scattered beds that contain chert and sand. These rocks were deposited by cyclic shallow seas. During this time, thick beds of calcium carbonate sediments were deposited in a shallow marine environment. During regressions, these rocks came into contact with meteoric water resulting in lithification and localized dissolution and extensive dolomitization (Jorgensen, 1989). The Arbuckle Group thickens from north to south in Kansas (Figure 2.3). The Wellington Field is located to the south in the Sedgwick Basin where the Arbuckle is thick, and off of the Kansas uplifts where Arbuckle is usually thin or eroded (Franseen et al., 2000). Favorable reservoir qualities such as fractures and faults are related to deep-seated basement structural elements and are enhanced by localized and stratigraphically specific karstification. The

Arbuckle has complex vertical and lateral heterogeneities including nonporous and porous horizons such as mud-dominated and grain-supported strata containing variable amount of connected and non connected interparticle porosity. Productive zones are controlled by different factors such as depositional facies, dolomitization, silicification, or intra-formational exposure events (Franseen et al., 2003). At the Wellington Field, the Arbuckle overlies thin Reagan Sandstones or basement, and the Arbuckle is overlain by the Simpson shales. The Chattanooga Shale, which is locally absent, was eroded over the portion of the Wellington Field. The Simpson Group is bound by two major unconformities (Watney et al., 2013).

The Mississippian carbonate shelf extended over a large area of the central and southwestern United States (Figure 2.4; Montgomery et al., 1998). During the Osagean, the outer shelf and shelf margin covered southern Kansas. Transgressive- regressive cycles resulted in the deposition of silica and carbonate-rich sediments including the sponge-rich shelf margin deposits along the shelf margin at the location of the Wellington Field (Watney et al., 2001; Franseen, 2006). Locally, biohermal buildups of mud-dominated limestone also developed on the shelf margin with oval or irregular shapes reaching thicknesses up to 48 meters. These bioherms exemplified the topographic relief that existed along the shelf margin/ramp (Montgomery et al., 1998). Carbonate strata with varying abundance of spiculite typify the Mississippian strata at the Wellington Field with accumulations forming low relief dolomitized bioherms. The progradation of these strata along the shelf margin filled in around the larger mud-dominated bioherms and advanced the shelf margin basinward, southward into Oklahoma. Subaerial exposure and meteoric water led to dissolution of spiculites and carbonate skeletal debris and their silicification and often, net porosity formation (Watney et al., 2001). The Mississippian reservoir at the Wellington Field is composed of microporous intercrystalline and vuggy cherty dolomites

with less chert, more dolomitic content and less vuggy pore space compared to the tripolitic chert reservoirs of the surrounding fields. Localized topography associated with buildups and facies change to more interparticle porosity resulted in focused early diagenesis that decreased downward with depth from a surface of subaerial exposure (Montgomery et al., 1998; Watney et al., 2001). Overlying the chert reservoirs are chert conglomerates with thicknesses up to 3 meters. These chert conglomerates have less porosity and permeability values due to dominance of impermeable siliciclastic clay rich that comprise these strata (Montgomery et al., 1998; Watney et al., 2001). The Mississippian is overlain by the Lower Pennsylvanian shales of the Cherokee Group, which provide the seal of the Mississippian reservoir in the Wellington Field (Figure 2.2).

2.3: Reservoir Architecture at the Wellington Field

2.3.1: Mississippian

Based on core analysis at well #15-191-22591 at the Wellington Field, the Mississippian strata consist of a succession of parasequences that are shallowing upward changing from dark shales and shaly carbonates to porous pale yellowish brown cherts and cherty dolomites that are less argillaceous. The reservoir at the Wellington Field has microporous and vuggy cherty dolomites. Comparing to the tripolitic chert reservoirs at the surrounding fields, however, the Mississippian reservoir has less cherty, more dolomitic content, and less vuggy pore space. The upper part of the reservoir is affected by brecciation and karstification due to Pennsylvanian weathering along the Pennsylvanian unconformity (Watney et al., 2013).The lower Pennsylvanian Cherokee Group thick shale provides a cap rock over the Mississippian (Figure 2.2).

According to well logs, the reservoir has a characteristic architecture (Figure 2.5). The Mississippian chert at the Wellington Field is characterized by downward gradational porosity from high porosity values (25%) at the top of the reservoir down to 4-6% at the base of the reservoir. The gradational porosity reduction is caused by depositional shallowing upward and diagenetic alteration due to water infiltration that is limited in depth (Watney et al., 2013). The downward porosity decrease is accompanied by gradational density increase (from 2.31 to 2.67 g/cc) and gradational velocity increase (from 3800 to 5300 m/s) (Figure 2.5). This gradational velocity increase gives a ramp-transition velocity function.

2.3.2: Arbuckle

The lower Ordovician Arbuckle Group is a thick succession of interbedded dolomudstones, pack-grainstones, vuggy brecciated zones, and thin dolomudstone and shale beds (Watney et al., 2013). The Arbuckle was fully penetrated by the two wells #15-191-22591 and #15-191-2259. The Arbuckle Group is divided into 15 flow units based on Lorenz crossplotting, which is a common method in reservoir modeling (Figure 2.6) (Rahimpour-Bonab, et al., 2012; M. FazelAlavi, 2014, personal communication). Based on core analysis at well #15-191-22591, highly permeable vuggy brecciated intervals are frequently present. These intervals are prominent in the lower part of the Arbuckle in the Roubidoux and Gasconade (Figure 2.7) (Watney, et al., 2013). A brecciated zone between the tops of flow units FU14 and FU15 was chosen to be the CO_2 injection zone in the lower part of the Arbuckle at both wells #15-191-22591 and #15-191-22590. This zone is about 25 m thick showing low velocity and high porosity values between the tops of flow units FU14 and FU15 on the well logs in Figure 2.6. This injection zone was perforated at both wells, and a pulse test was conducted which showed communication within the zone between the two wells (Watney et al., 2013). Based on the

analysis of brines obtained by drill stem tests and swabbing perforations, the Arbuckle is composed of three hydrostratigraphic units. The middle hydrostratigraphic unit is dominated by low permeability and low porosity. Based on stable isotope data and brine chemistry, the lower Arbuckle highly permeable interval and the CO_2 injection zone are isolated from the top of the Arbuckle (Watney et al., 2013).
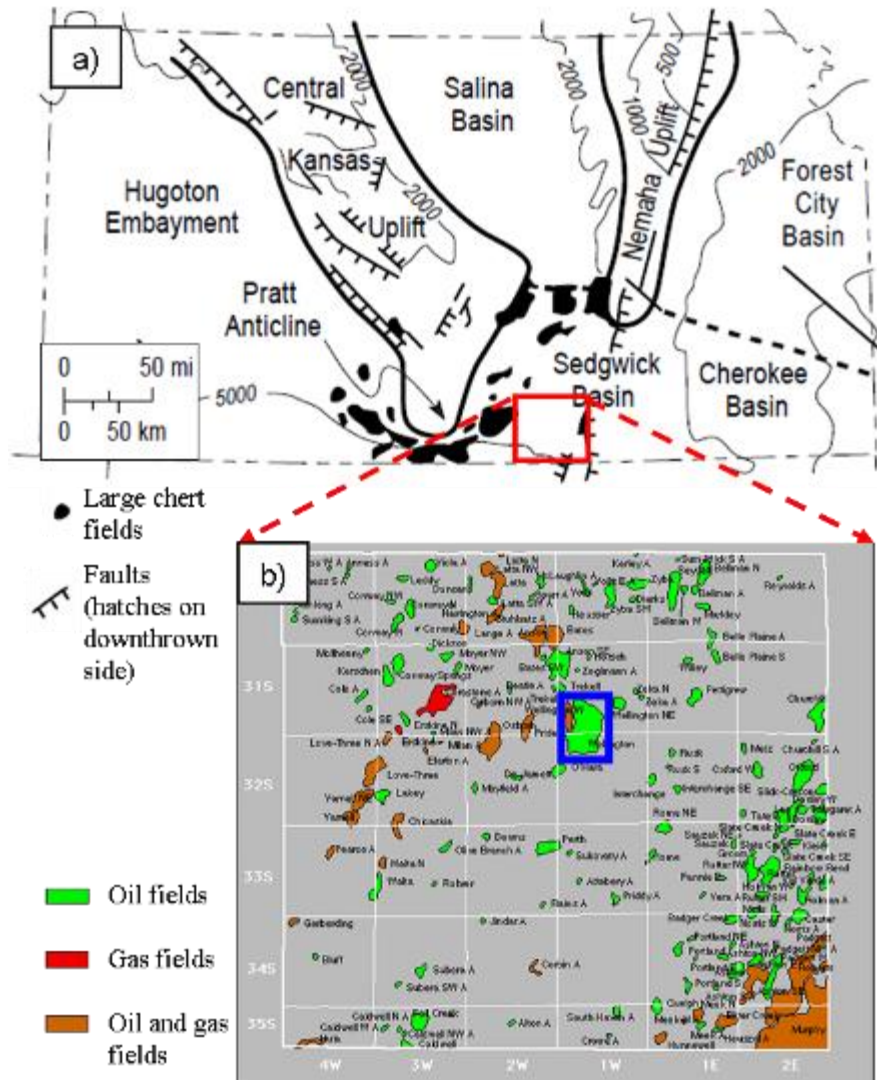
Figure 2.1. Wellington Field location: a) Location of Sumner County (red box) within the major tectonic elements during the late Mississippian-early Pennsylvanian time in Kansas. Modified from Montgomery et al. (1998); b) Oil and gas fields located within Sumner County. The Wellington Field is outlined with the blue box. From Sirazhiev (2012).
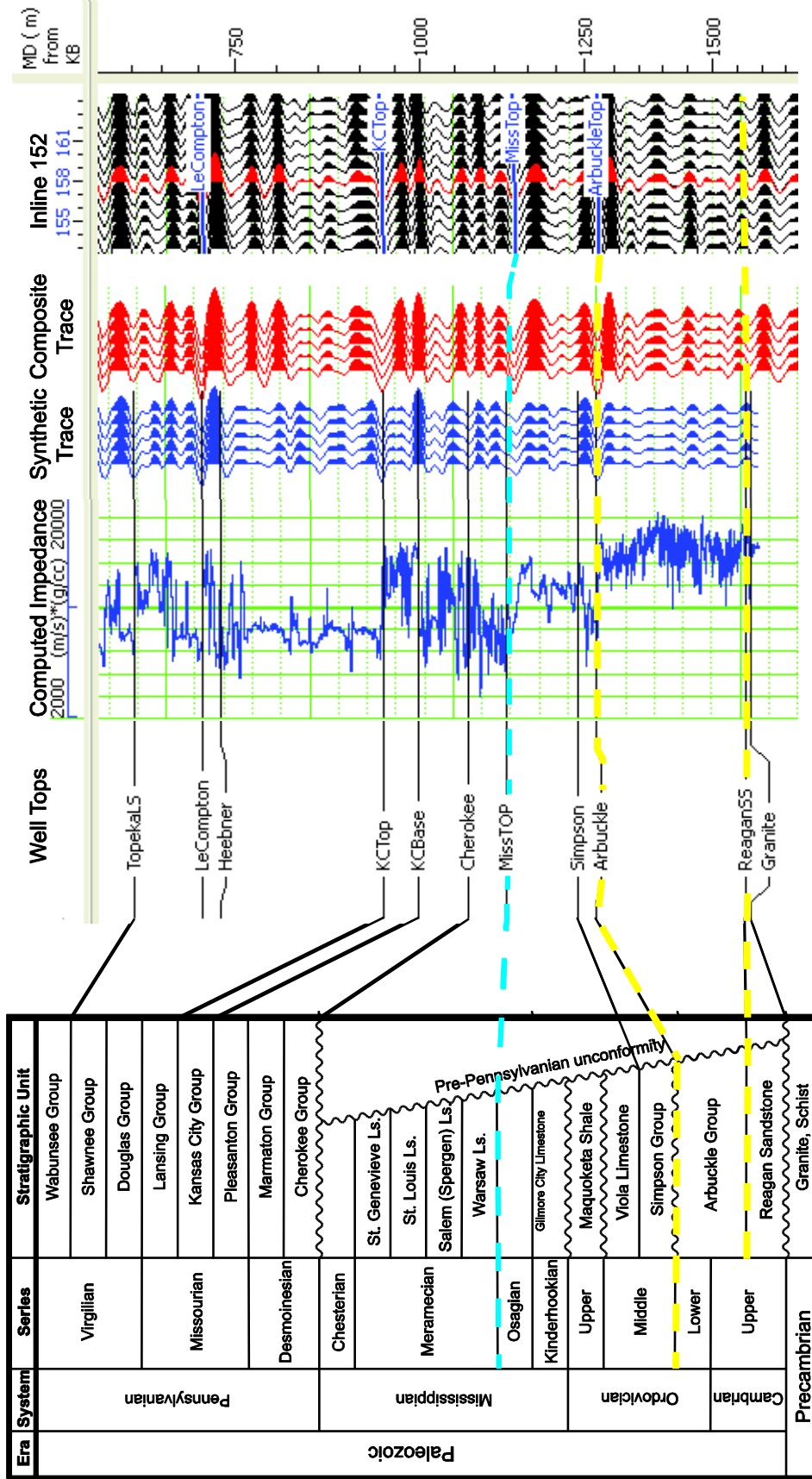
Figure 2.2. From left to right: stratigraphic column for central Kansas (Modified from Nissen et al. (2009)); well tops, impedance log, synthetic seismic traces (blue) and real seismic traces (red) at well #15-191-22591; part of inline #152. The Mississippian reservoir top is identified by the blue dashed line, and the thick Arbuckle Group is between the yellow dashed lines. Modified from From Sirazhiev (2012).
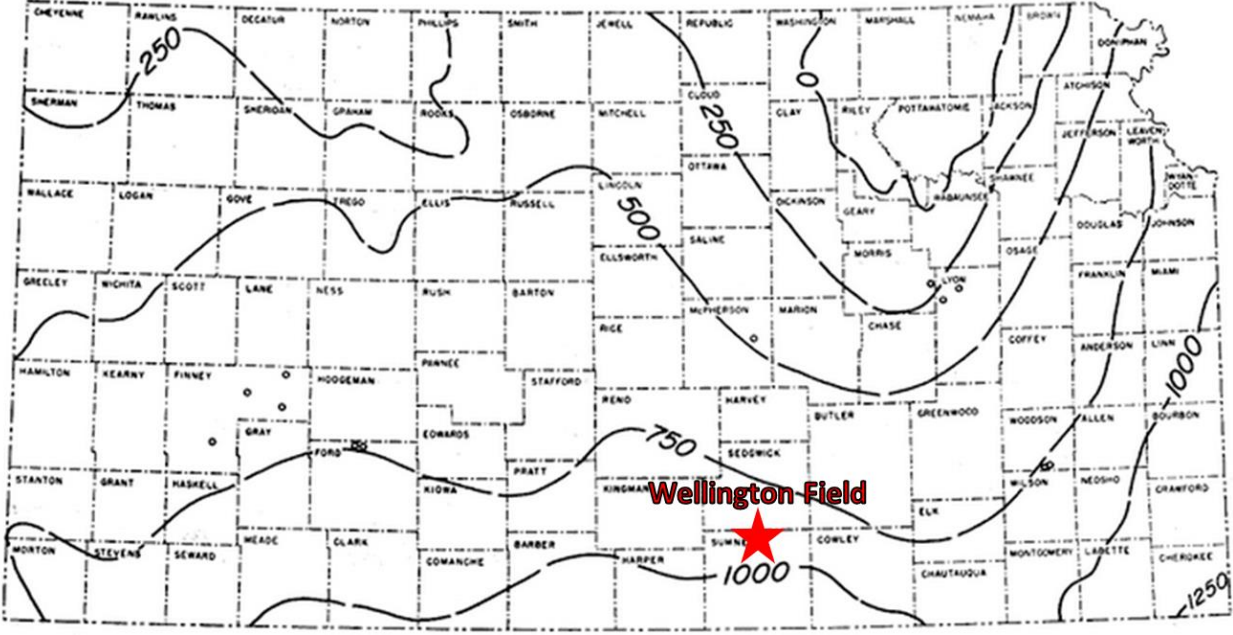
Figure 2.3. Kansas Arbuckle Group isopach map. Modified from Merriam (1963).
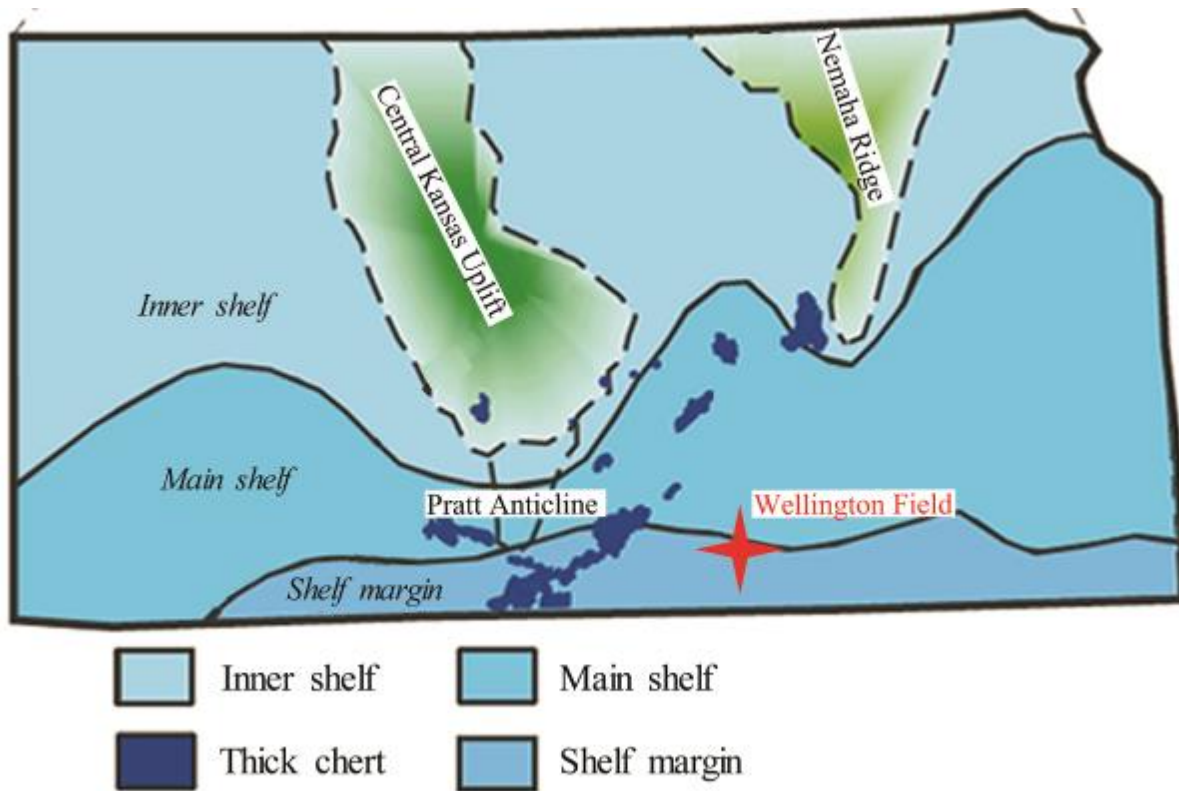
Figure 2.4. Paleogeographic and depositional conditions in Kansas during the Mississippian time. Red star shows the location of the Wellington Field. From Sirazhiev (2012), originally from Franseen (2006).
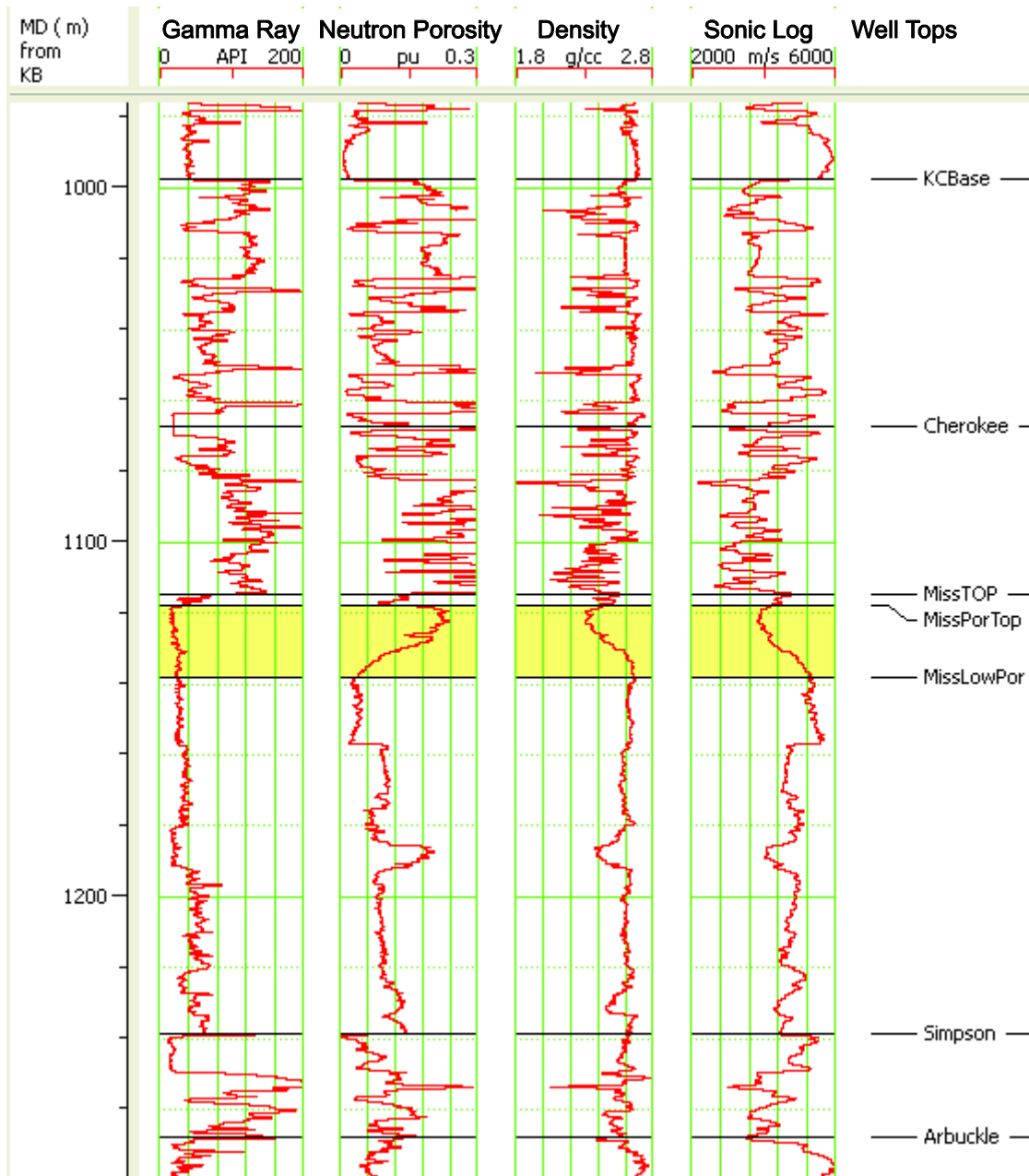
Figure 2.5. Characteristic architecture of the Mississippian chert reservoir at the Wellington Field according to the well logs at well #15-191-22591. Note the interval (highlighted in yellow) with downward porosity reduction (from 25 to 4%) and corresponding gradational velocity (from 3800 to 5300 m/s) and density (from 2.31 to 2.67 g/cc) increases. From Sirazhiev (2012).
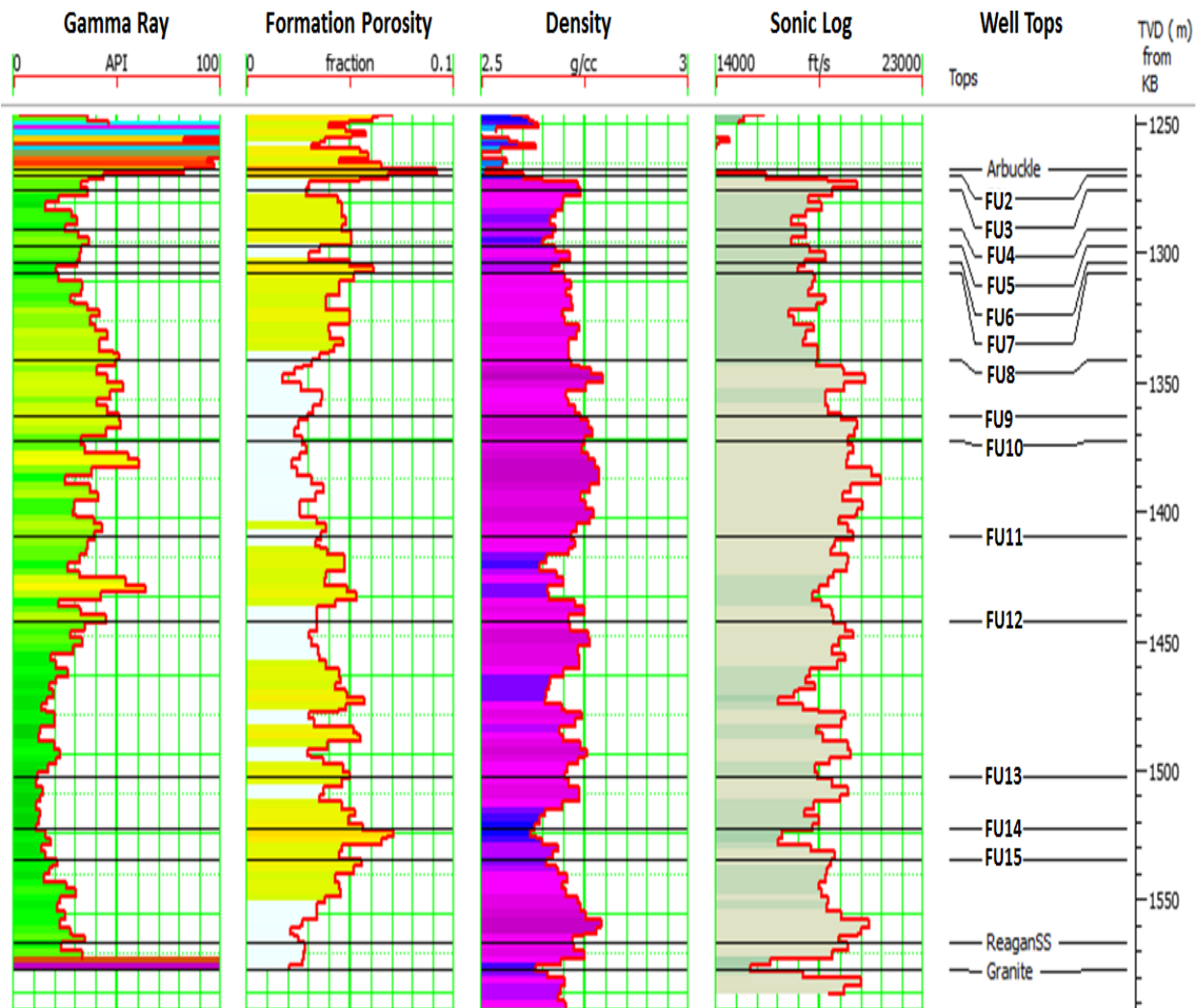
Figure 2.6. Well logs of well #15-121-22591 within the thick Arbuckle Group. The Arbuckle Group is divided into 15 flow units based on Lorenz crossplotting (M. FazelAlavi, 2014, personal communication).
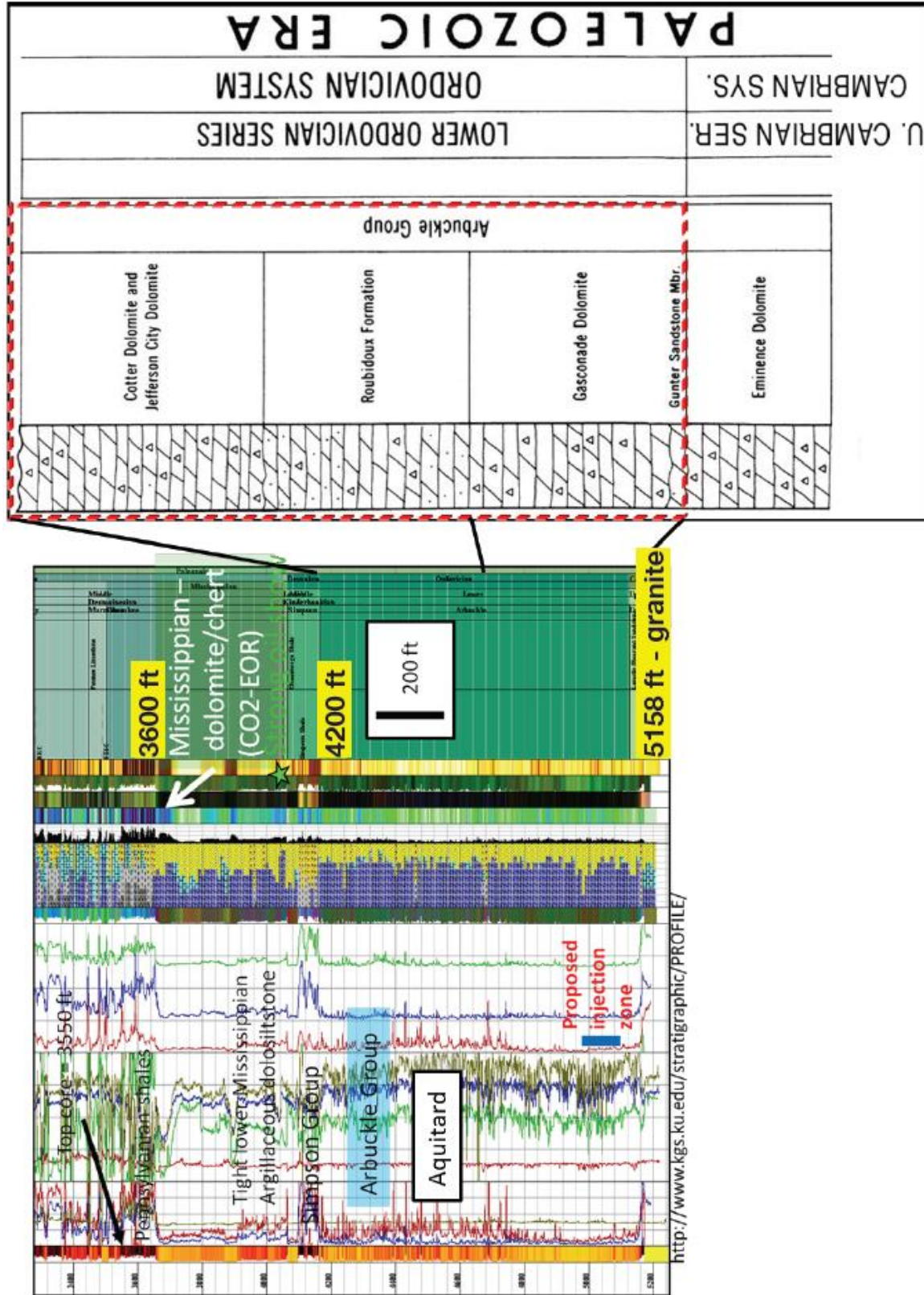
Figure 2.7. The cored interval of well #15-121-22591 with well log, computed lithology and stratigraphic correlations of the Arbuckle Group. From Watney et al. (2013).

CHAPTER 3: SEISMIC DATA INTERPRETATION

3.1: Seismic Data

For conducting pre-stack data analysis, 3D pre-stack time migrated offset gathers were used (Table 3.1). This data was acquired by Paragon Geophysical Services Inc. in 2010 at the Wellington Field. P-wave data processing was performed by FairfieldNodal in 2010-2011. The Wellington Field data was merged while processing with 3D seismic data from the adjacent Anson-Bates Field. The seismic data has a total number of 542 inlines and 251 crosslines. For this study, only the data covering the Wellington Field was utilized. This data set covers an area of about 28.5 km^2 (Figure 3.1). These seismic gathers needed further processing and data conditioning before performing the pre-stack data analysis and inversion. F-K filtering was applied to the gathers to remove low-frequency coherent linear noise that greatly affected amplitude variation with offset (Appendix A). After that, a Trim Statics correction was applied to the data to correct for residual move-out errors that affect the estimation of the gradient and any other related attributes (Appendix B). Then, AVO offset scaling was applied to correct for processing artifacts and amplitude distortion by the previous processing steps applied on the data, which affected the mean gradient trend of the real data (Appendix C). Figure 3.2a shows an offset gather at the location of well #15-121-20789 after processing. For AVO analysis and inversion, the data needed to be converted to angle gathers as shown in Figure 3.2b.

Seismic data	3D pre-stack time migrated gathers
Processing operations done	NMO Correction, Radon Filtering, Time Variable Filtering, Trace Equalization
BANDPASS FILTER	10-128 Hz
CDP Number of Traces	58 traces
Offset Range	from 139 m (456 ft) to 1523.5 m (4997 ft)
Trace Length	1200 ms
Number of inlines	542 (used range 1-289)
Number of crosslines	251 (used range 73-251)
Bin size	25.146 m (82.5 ft)
Polarity	SEG reversed

Table 3.1. Overview of the pre-stack migrated seismic gathers of the Wellington Field.
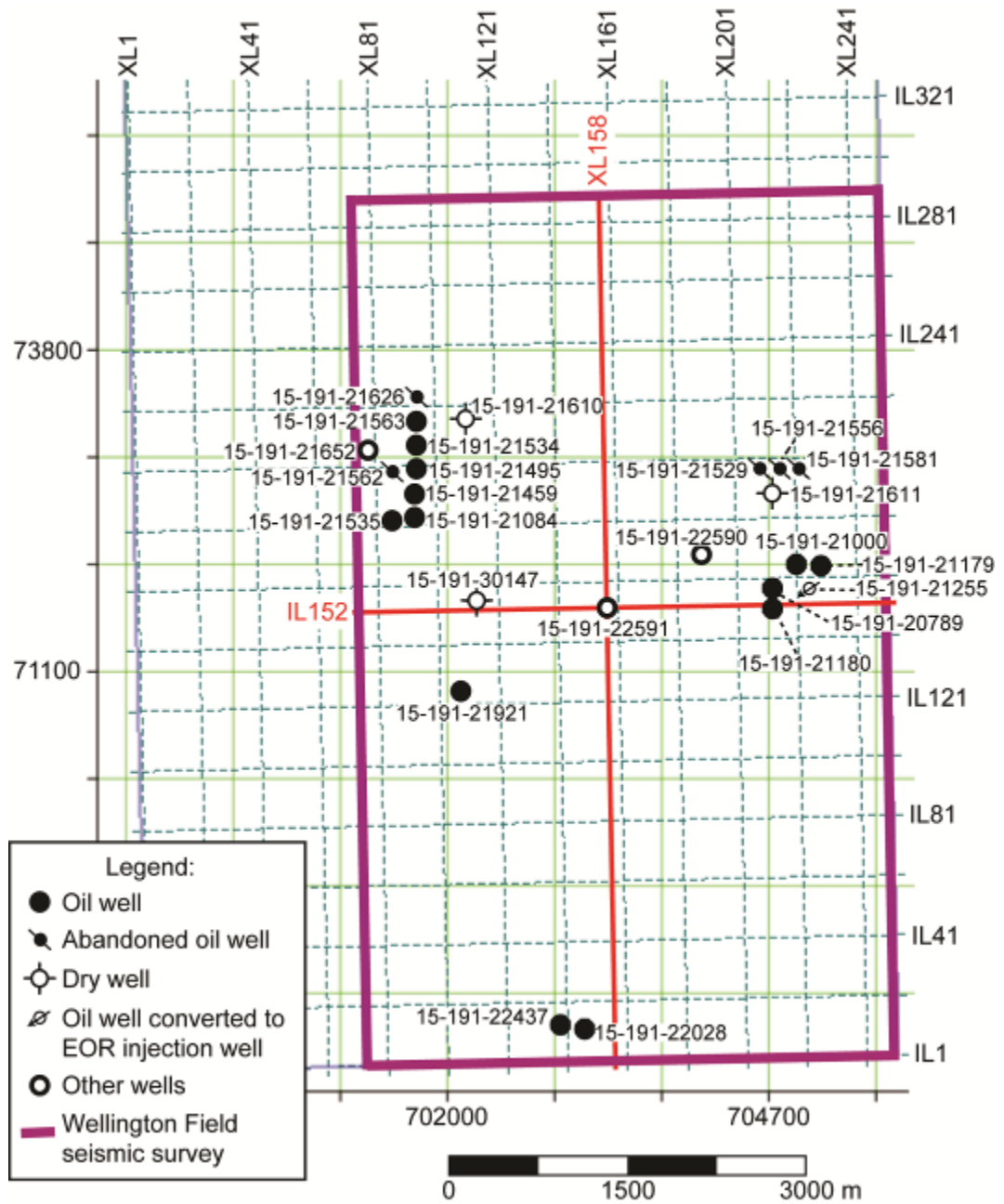
Figure 3.1. Basemap of the Wellington Field seismic survey used in this research with well locations. From Sirazhiev (2012).

18
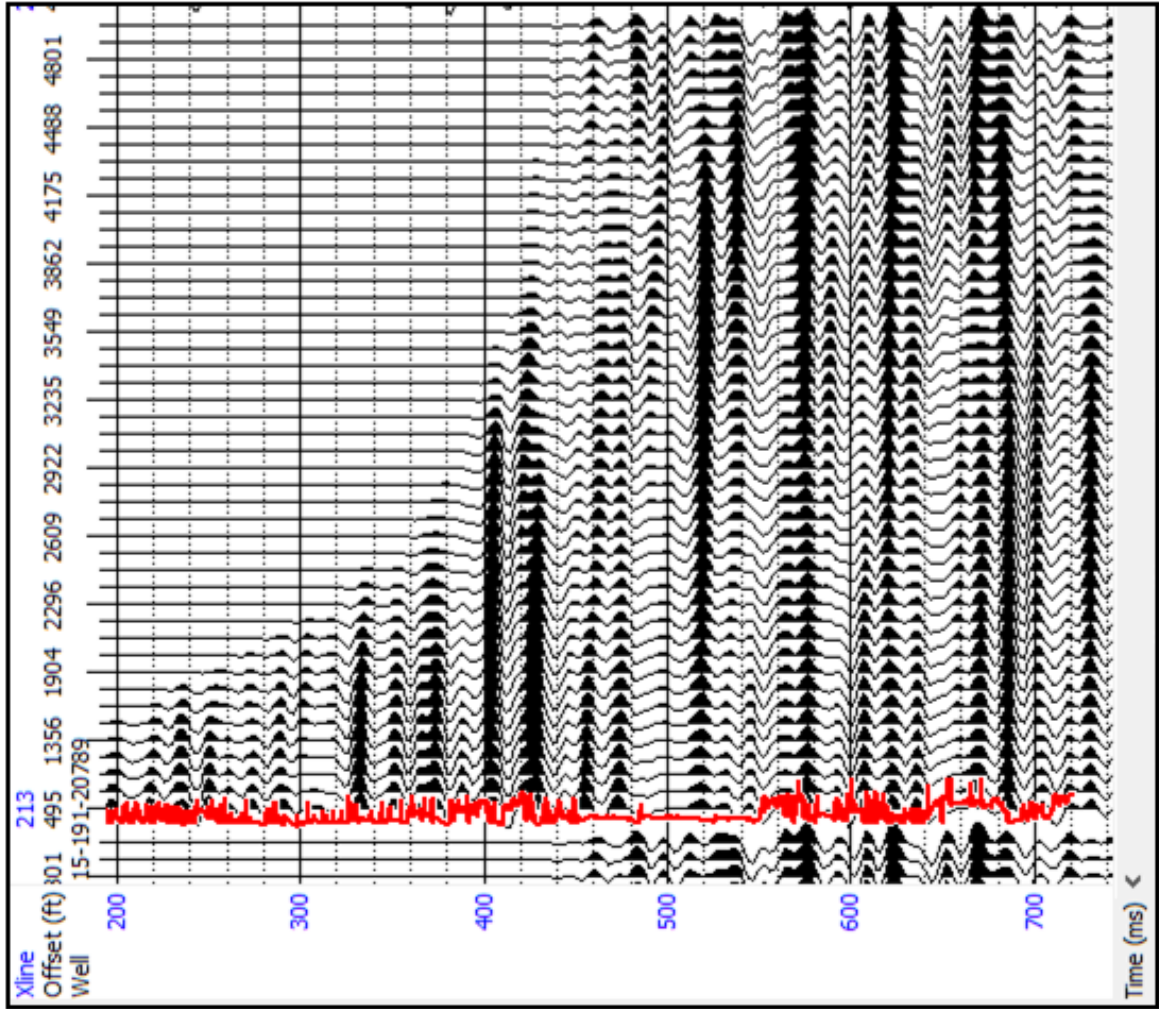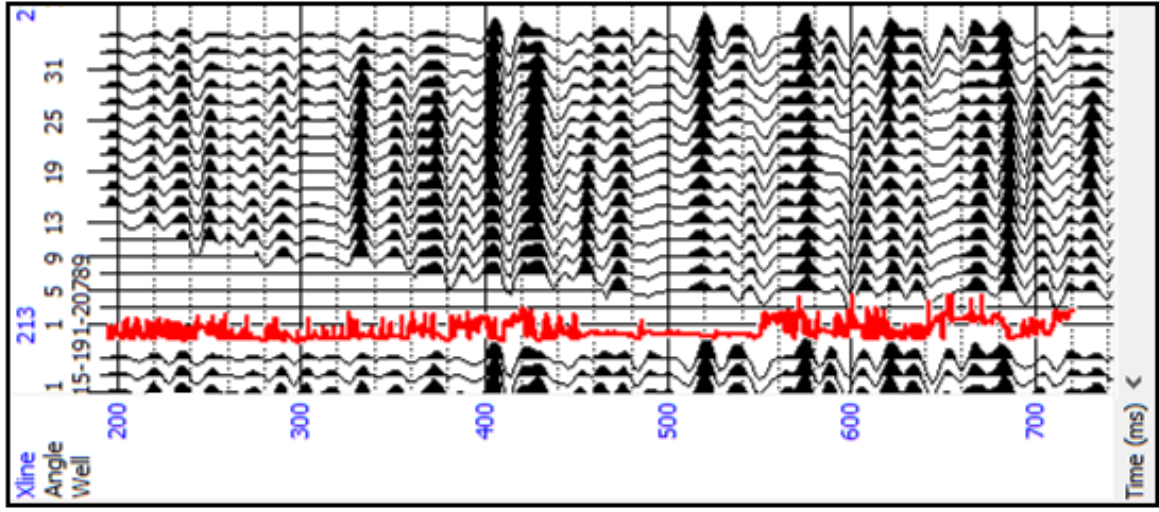
Figure 3.2. (a) Offset gather at well #15-191-20789. (b) Angle gather at well #15-191-20789.

3.2: Post-stack Seismic Interpretation

In addition to the pre-stack seismic gathers, post-stack time and depth-migrated versions of the same seismic data were used. The post-stack seismic data was used for interpreting time horizons that are needed for guiding the analysis of the AVO attributes; Intercept (A) and Gradient (B), and for building the initial models for the simultaneous AVO inversion of pre-stack data as described in sections 4.1 and 5.1. The depth converted seismic was used for structural interpretation because it corrects for seismic imaging distortion due to the lateral and vertical velocity variations.

Figure 3.3 shows the location of Wellington Field wells. The color coding shows the available well logs at each well. For interpreting the seismic horizons, the wells that have original sonic logs were tied to the seismic data. These wells are #15-121-22590, #15-121-22591, #15-121-20789 and #15-121-30147. These wells were tied to the pre-stack and post-stack seismic data to identify the corresponding time reflections of the different tops.

In Figure 3.3, the wells colored green and purple have formation porosity well logs which are needed for the multi-attribute linear regression analysis for porosity prediction as described later in section 6.1. These formation porosity logs need to be tied correctly to the seismic data for porosity prediction. Only wells #15-121-22590, #15-121-22591, #15-121-20789 have original P-wave sonic logs. The other wells have pseudo-sonic logs that were generated in the previous work on the Wellington Field done by Sirazhiev (2012) for establishing the time-depth relationship needed to tie the well logs to the seismic data. Eleven wells that have a good tie with seismic data were selected to be used in the multi-attribute linear regression analysis for porosity prediction. By using the original density logs, P-wave sonic logs and pseudo-sonic logs of these

wells, P-impedance logs were calculated for these eleven wells that will be used for evaluating

the simultaneous AVO inversion results later in section 5.2.

A statistical wavelet was extracted from the window between 300 and 800 ms of the

seismic data for two purposes (Figure 3.4). The first purpose is to tie the wells to the seismic data

by generating a synthetic seismogram. The second purpose is to measure the resolution limit of

the seismic data. The extracted wavelet shows a dominant frequency of 55 Hz and the average

velocity calculated within the Mississippian reservoir at well #15-121-22591 is about 4450 m/s.

From the wavelength equation ($\lambda = V_{average}/f$), the wavelength λ is 81 m. So, the seismic

resolution limit ($\lambda/4$) is about 20 m.

Figure 3.5 is a two-way time post-stack PSTM seismic cross section of Line A whose

location is shown on the Map in Figure 3.3. Most of the results will be demonstrated on Line A

because it is a representative line of the Wellington Field that extends in an east-west direction.

Also, Line A includes wells #15-121-22590 and #15-121-22591 that penetrated both the

Mississippian and the Arbuckle. As shown in Figure 3.5, six horizons were interpreted on the

post-stack seismic data. Five of these horizons are the tops of the Oread Limestone, the Kansas-

City Group, the Mississippian System, the Arbuckle Group and the basement. The additional

horizon (Horizon_1) was picked to illustrate the thinning of the Oread Limestone that is

overlapped by shale. Horizon_1 is the top of this shale (Figure 3.5). These thickness changes

cause time delay of the seismic reflections below the thicker part of the shale. The time delay

causes the time difference between the Mississippian top at well #15-121-22590 and the

Mississippian top at well #15-121-22591 (Figure 3.5).

At the location of well #15-121-22590, there is a double reflector at the top of the

Mississippian (Figure 3.5). The reason of this double reflector is the presence of a low

impedance layer overlying the Mississippian reservoir that is thick enough to be resolved and cause a localized double reflector. Figure 3.6 is an isochron map of the double reflector. The thicker layer above the Mississippian reservoir at well #15-121-22590 is attributed to a normal fault that is dipping to the SE (Figure 3.7). Figure 3.7 is a depth migrated seismic section of Inline #169 that shows the normal fault. Showing the fault on Inline #169, which extends E-W, is better than showing the fault on the Arbitrary Line A because Line A is oblique to the fault strike (Figure 3.6). Also, it is better to interpret the fault using the depth-migrated seismic data because the fault position is distorted by the time delay caused by the thinning of the Oread Limestone that was onlapped by a large section of shale (Figure 3.5). The normal fault created more accommodation space for thicker sediments to be deposited which caused the localized double reflector. The fault extends along the NW boundary of the localized double reflector between the two wells #15-121-22590 and #15-121-22591 (Figure 3.6). The same normal fault extends down to the basement cutting through the deeper Arbuckle Group as shown in Figure 3.8 which is a depth migrated seismic cross section along Line B that extends NW-SE perpendicular to the fault strike. The fault is interpreted to be of post-Mississippian early Pennsylvanian age because it cuts through the Mississippian and the underlying layers down to the basement, and there is a filled basin structure on the hanging wall above the Mississippian reservoir overlain by the flat layers that are not cut by the fault.
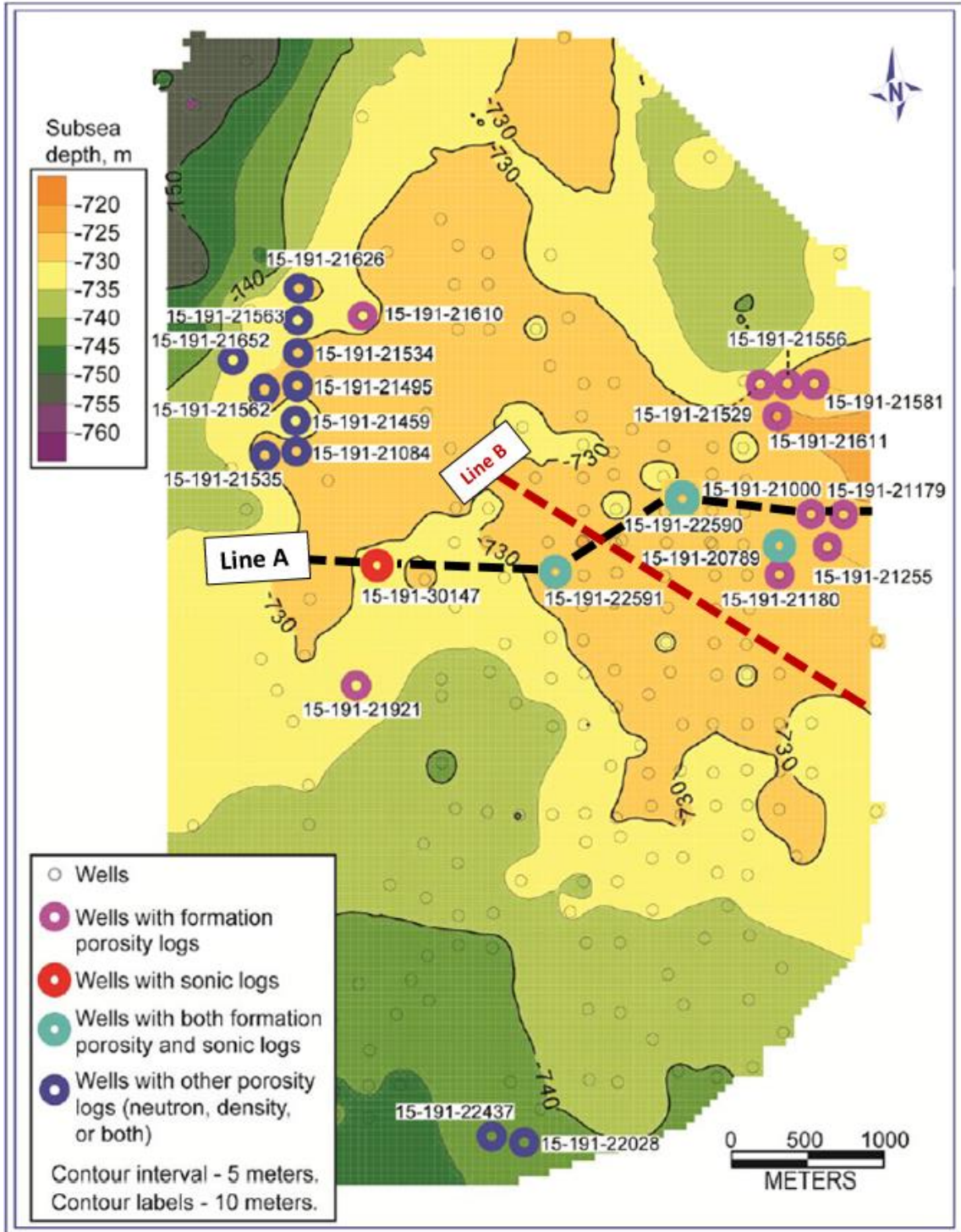
Figure 3.3. Mississippian depth map at the Wellington Field based on well data. Line A and Line B are locations of the cross sections on which seismic data, inversion results, and porosity prediction results are demonstrated. Modified from Sirazhiev (2012).
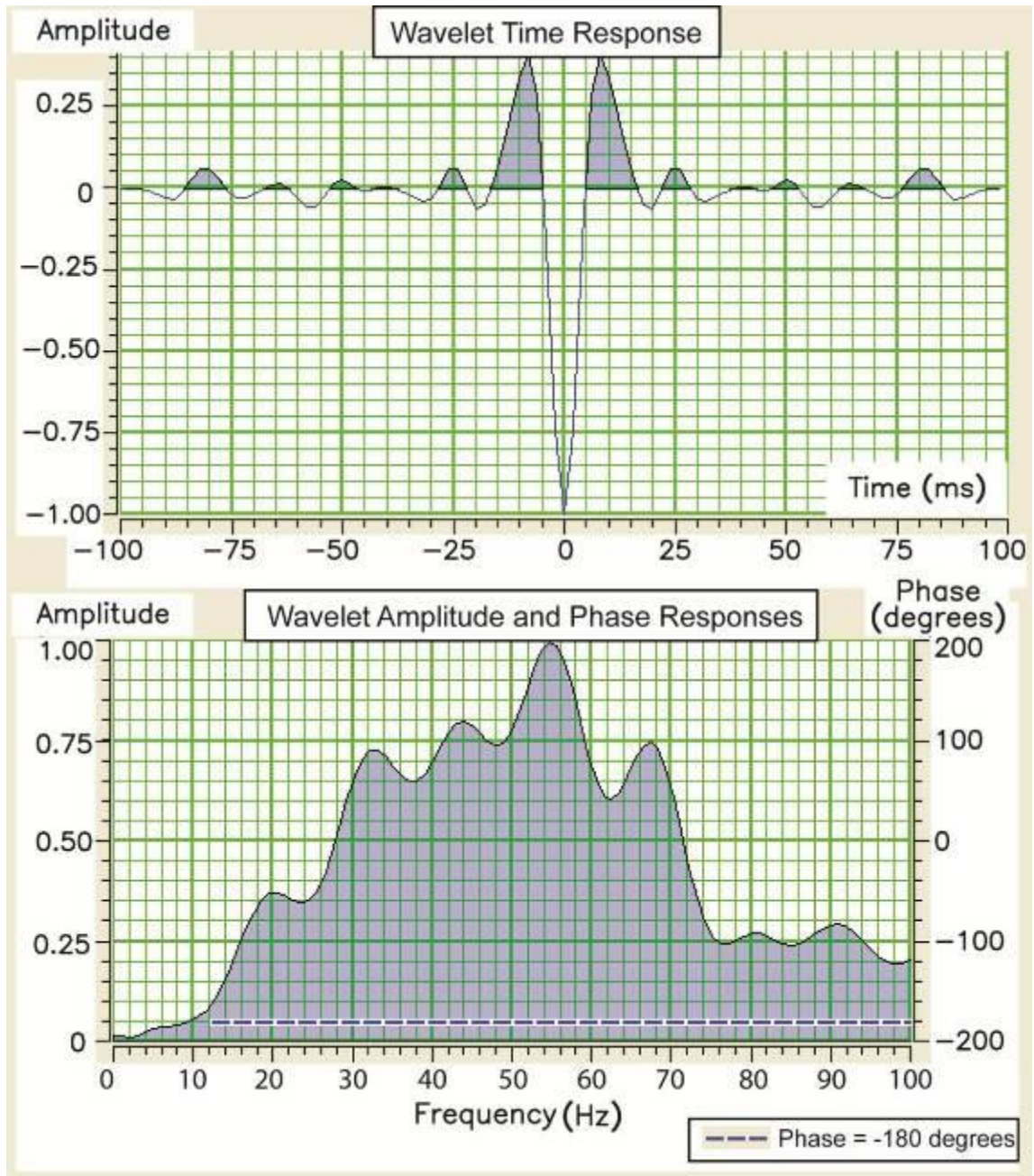
Figure 3.4. (Top) Null-phase statistical wavelet extracted from the seismic data in the time window 300-800 ms. (Bottom) Statistical wavelet amplitude and phase spectra. The wavelet has reverse polarity. From Sirazhiev (2012).
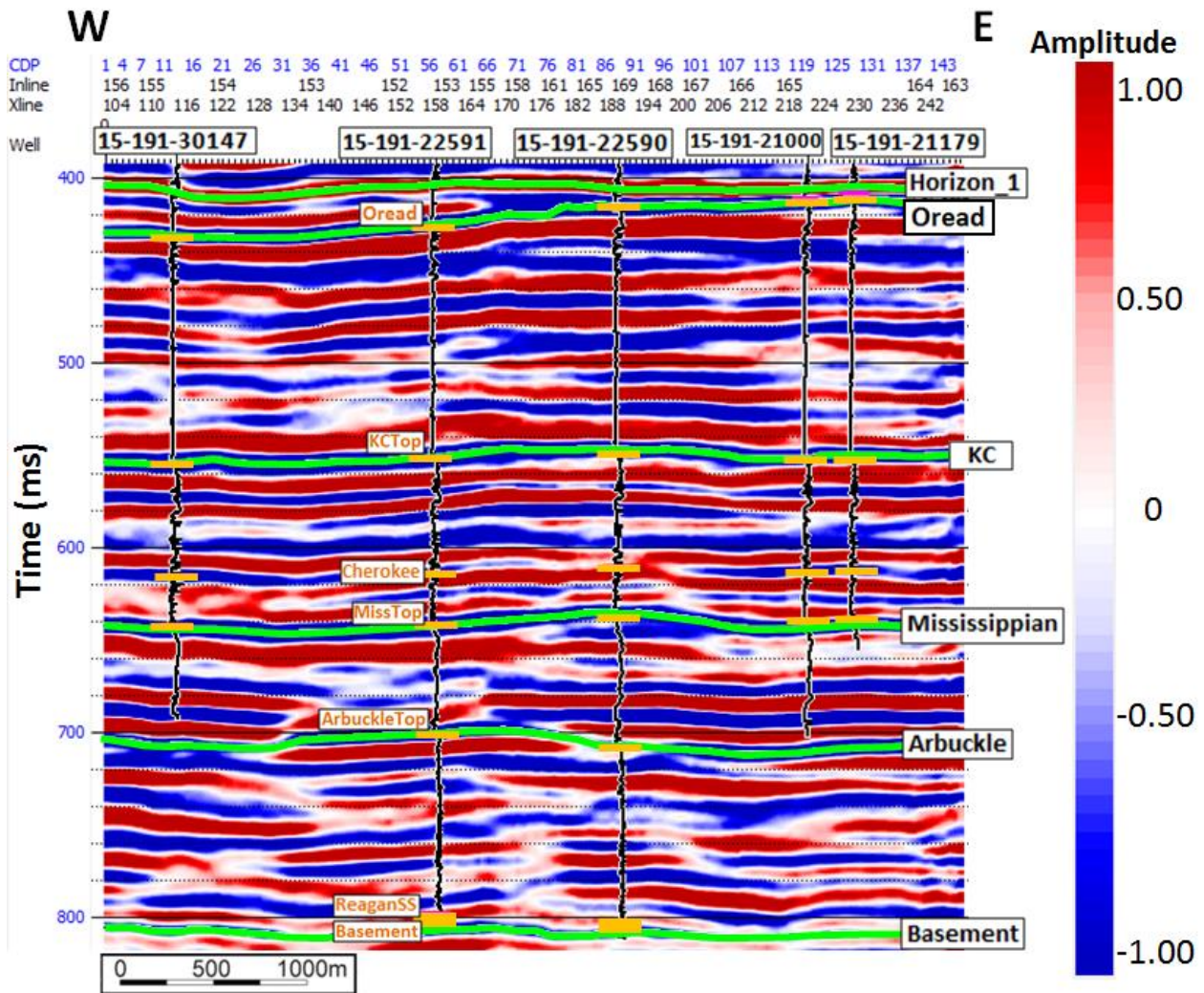
Figure 3.5. Time migrated seismic amplitude cross section. Cross section location is Line A shown in Figure 3.3.
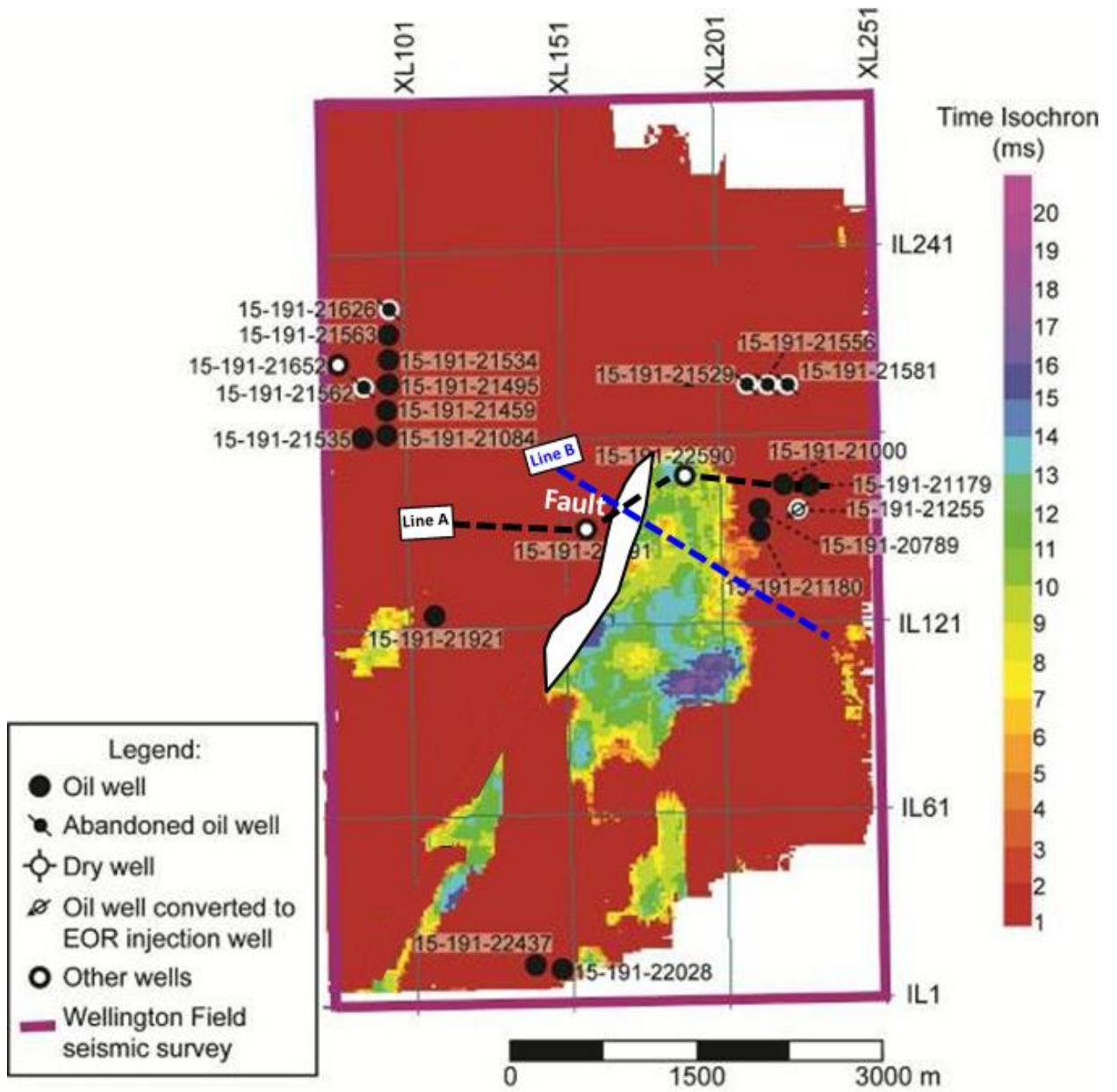
Figure 3.6. Double reflector isochron map bounded by post-Mississippian normal fault striking NE-SW and dipping SE. Modified from Sirazhiev (2012).
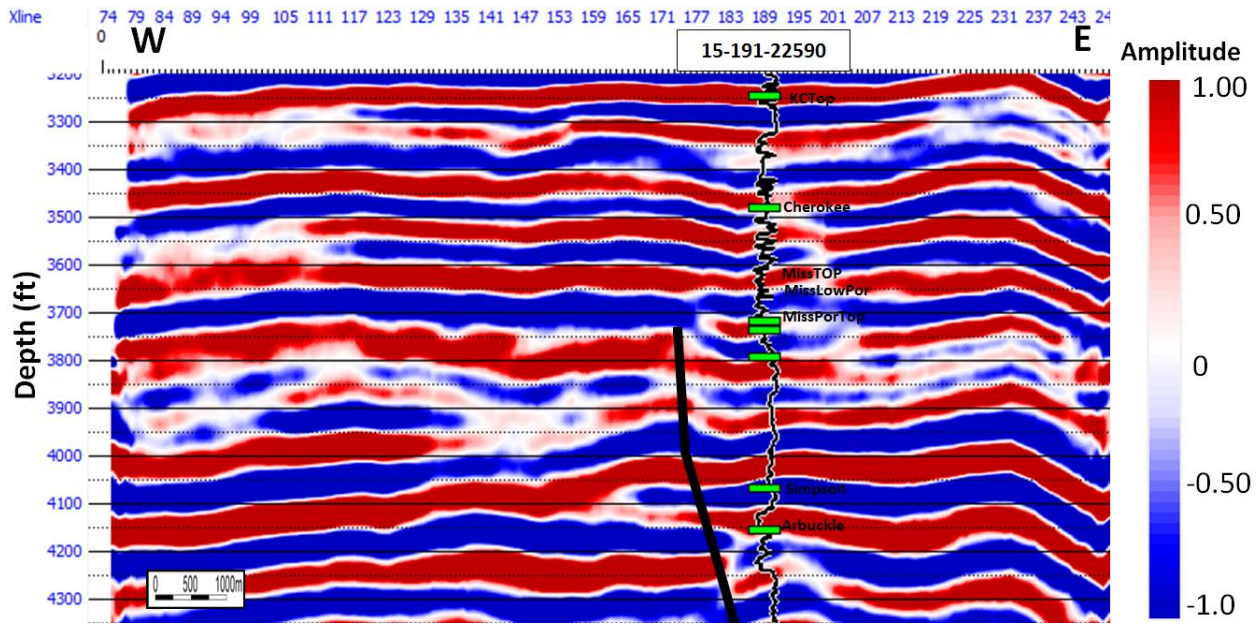
Figure 3.7. Depth migrated seismic section at inline #169 with post-Mississippian normal fault to the left of well #15-121-22590.
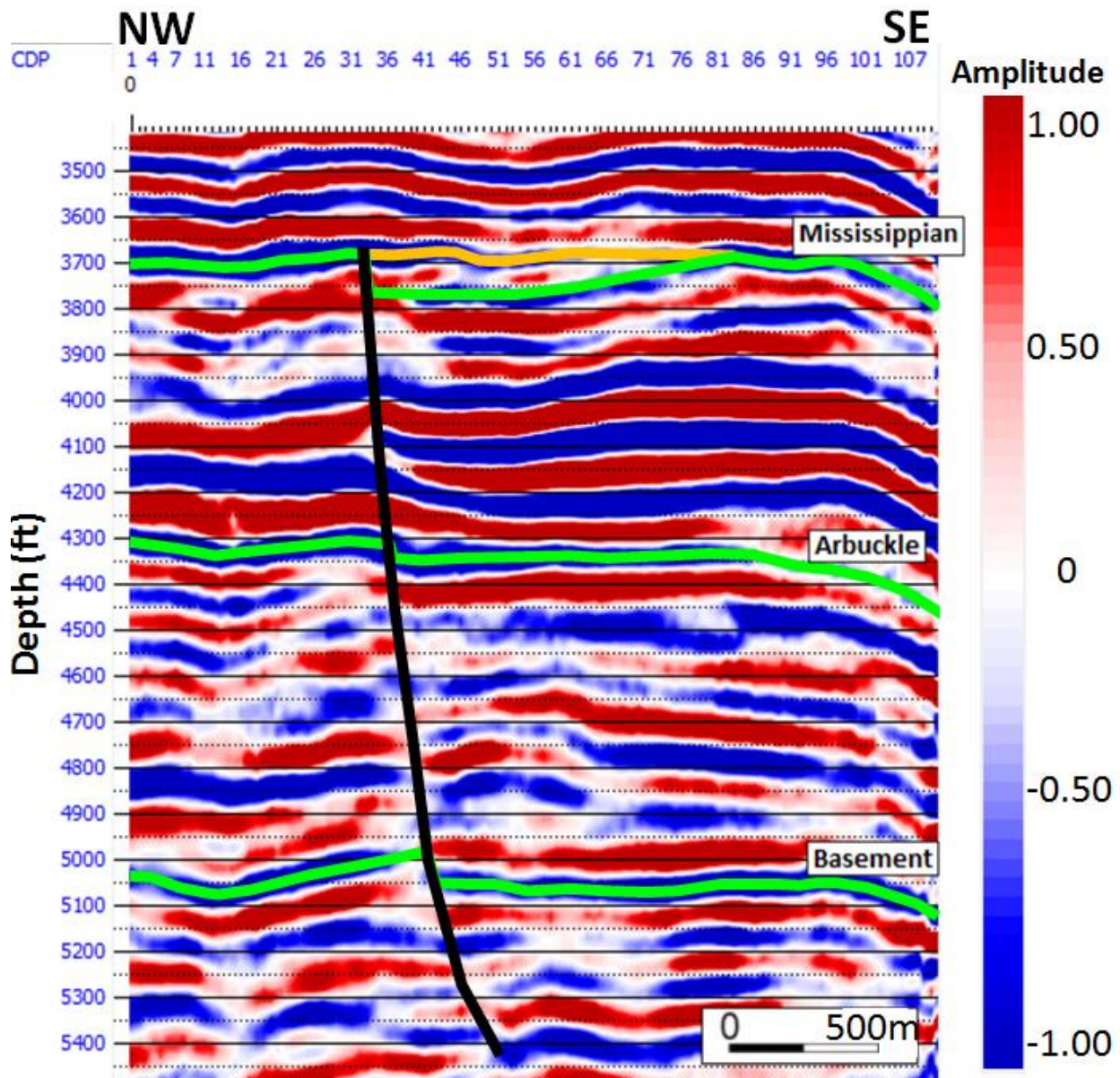
Figure 3.8. Depth migrated seismic section with post-Mississippian normal fault dipping to the SE. Cross section location is Line B shown in Figure 3.3.

CHAPTER 4: RESERVOIR AVO CLASSIFICATION

4.1: Mississippian Reservoir AVO Classification

The AVO attributes, intercept (A) and gradient (B), were analyzed at the Mississippian reservoir using the Hampson-Russell software. Figure 4.1 shows the angle gathers at the locations of wells #15-121-22591, #15-121-22590 and #15-121-20789. The Mississippian reservoir reflections picked at the three well locations are indicated by the red, the blue and the yellow lines, respectively. To the right of Figure 4.1 are the AVO crossplots of the reflection amplitudes with their trend lines. The trend lines show Class IV AVO response that is characterized by negative intercept (A) and positive gradient (B) (Figure 4.2; Avseth et al., 2005). The A-B crossplots of the Mississippian reservoir at 11 wells are plotted in the fourth quadrant in the typical location of Class IV AVO crossplots (Figures 4.2-4.3). Using the 3D volume of migrated seismic gathers, I created two AVO seismic attributes volumes for the whole Wellington Field area. These volumes are the Intercept (A) volume and the gradient (B) volume. Figure 4.4 is the intercept (A) cross section of Line A with P-wave sonic logs and green markers of the Mississippian reservoir posted at the well locations. The figure shows that the Mississippian reservoir at all of the well locations has negative intercept (A) values indicated by the negative blue event within the Mississippian reservoir. Figure 4.5 is the gradient (B) cross section of Line A. The figure shows that the Mississippian reservoir at the well locations has positive gradient (B) values indicated by the positive red event within the Mississippian reservoir. The intercept (A) and gradient (B) of Line A were crossplotted within a 60 ms window around the Mississippian horizon (Figure 4.6). Then, the plots falling within in the Class IV zone were highlighted by the red polygon (Figure 4.6). The seismic data on Line A corresponding to these Class IV points are shown in red on the seismic cross section in Figure 4.7. The crossplot

polygon highlighted the Class IV AVO zones between the markers of the top and base of the Mississippian reservoir at all of the well locations. All of the wells in Figure 4.7 have good porosity values within the Mississippian reservoir including well #15-121-30147 that has high calculated porosity of 24% at the top of the reservoir even though it was reported as a dry well possible due to poor localized porosity connectivity. This well was sidetracked later and produced oil from the Mississippian reservoir. The same observation holds for the two wells #15-121-21611 and #15-121-21610 that have porosity values of 25% and 20% respectively at the top of the Mississippian reservoir but the wells were reported as dry wells. Therefore, the Mississippian reservoir at these two wells showed a Class IV AVO response that was highlighted by the crossplotting technique.

The A-B crossplotting technique at the Mississippian reservoir consistently identifies a Class IV AVO response that highlights reservoirs with good porosity, even those that are not necessarily productive due to potentially localized porosity connectivity.
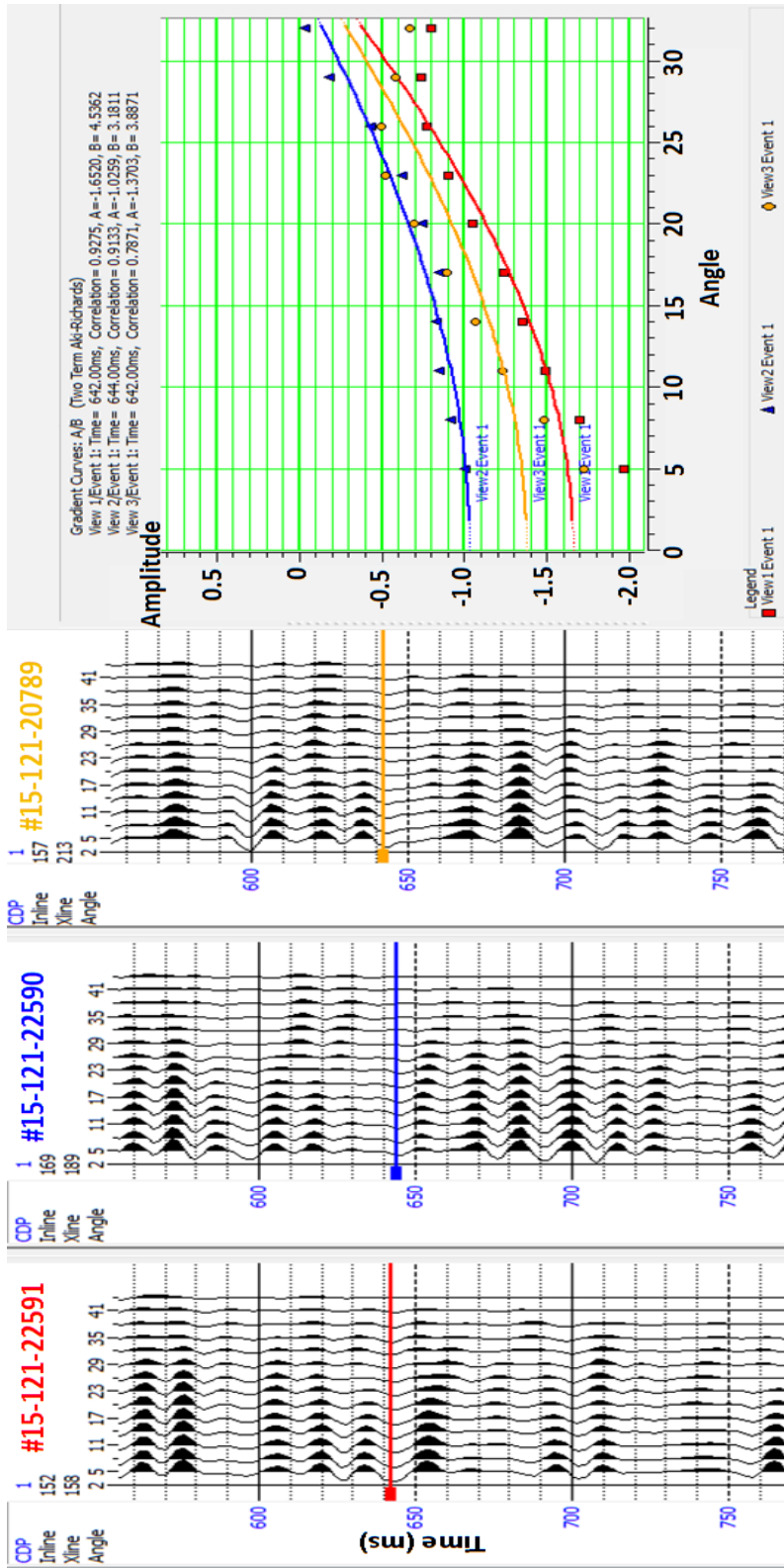
Figure 4.1. (Left) Seismic angle gathers at wells #15-121-22591, #15-121-22590 and #15-121-20789 with picked Mississippian reservoir events. (Right) AVO crossplots of the picked seismic traces with their trend lines that show Class IV AVO response.
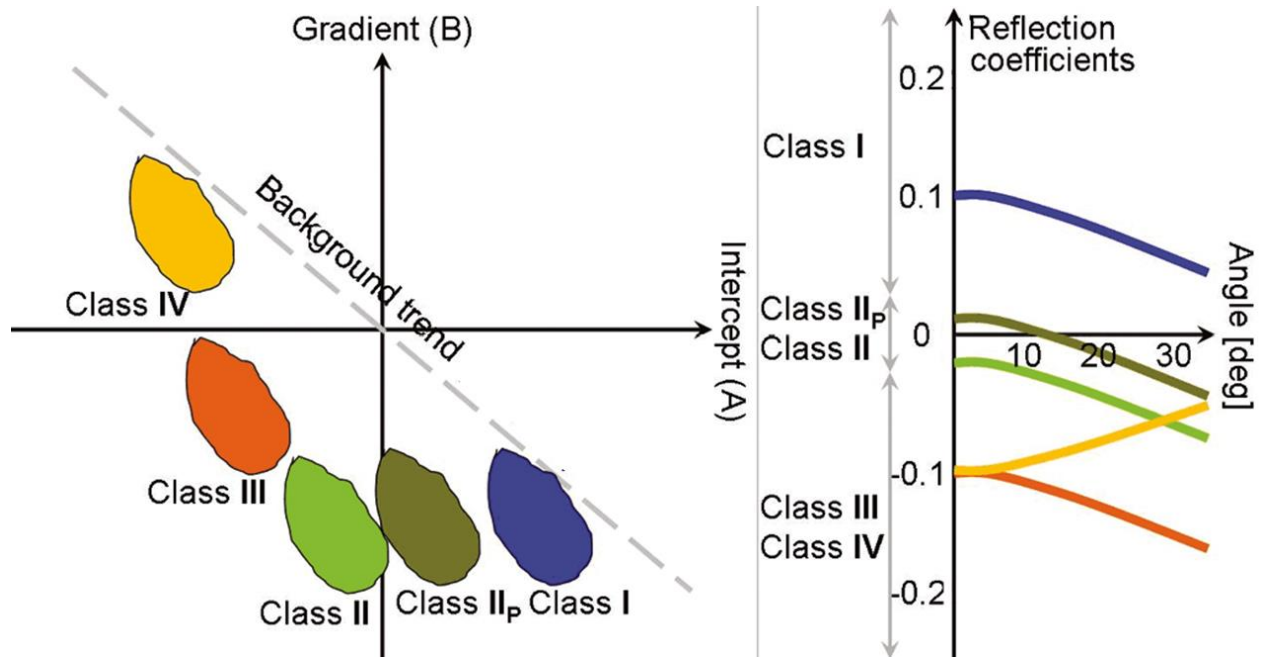
Figure 4.2. AVO classes. Modified from Avseth et al., (2005).
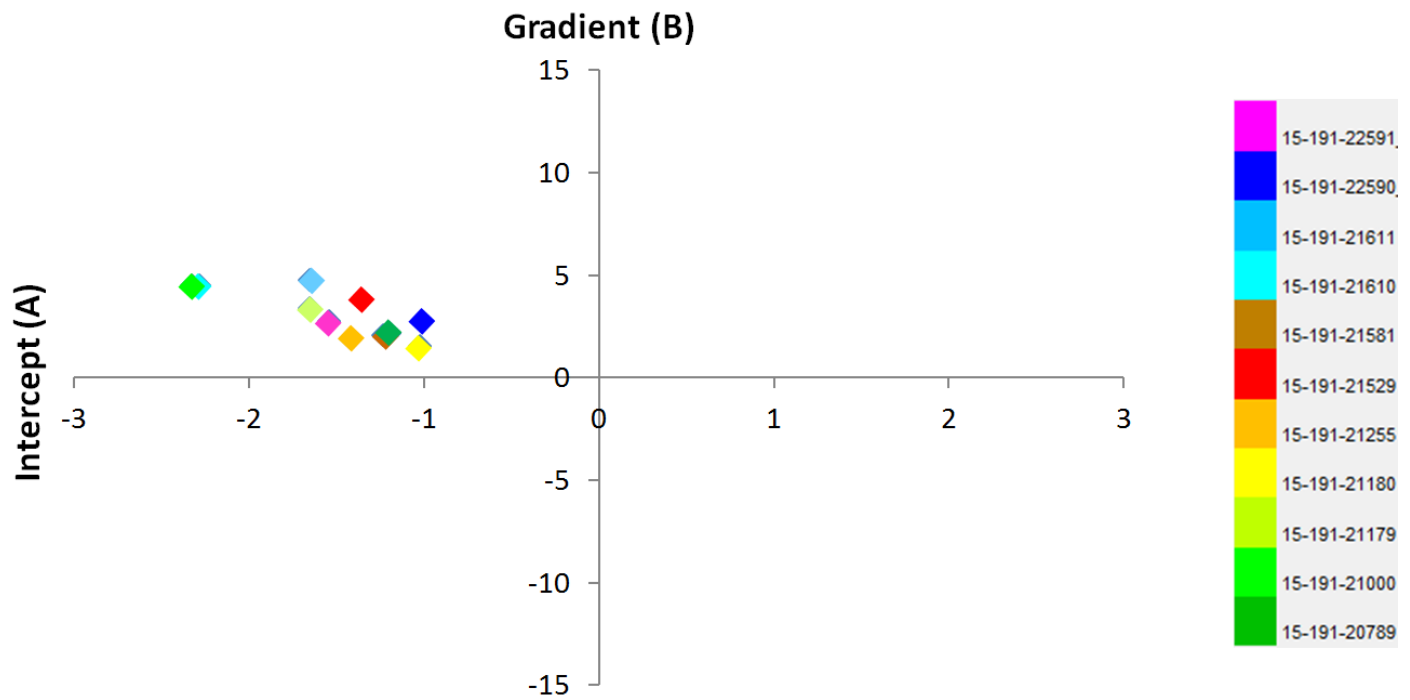
Figure 4.3. Mississippian chert reservoir A-B crossplots at 11 wells are plotted in the fourth quadrant in the typical location of Class IV AVO crossplots.
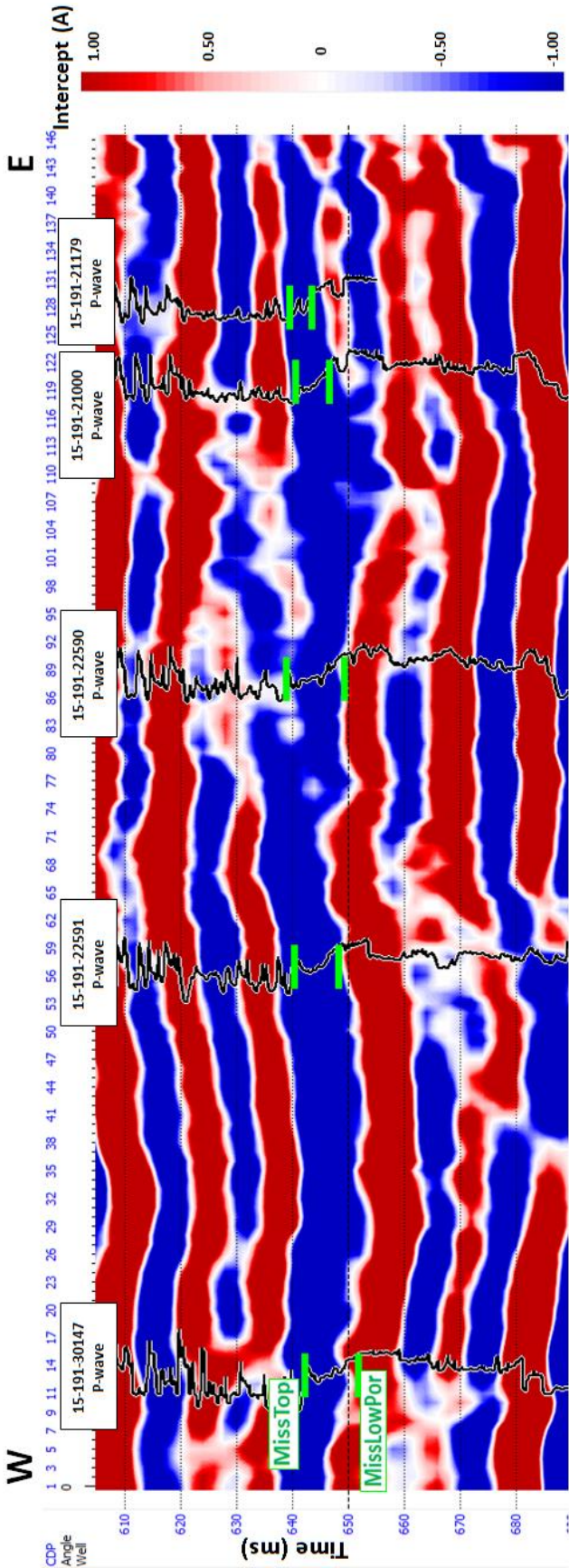
Figure 4.4. Intercept (A) cross section with P-wave sonic logs posted at the well locations. The Mississippian reservoir at all of the well locations has negative intercept (A) values indicated by the negative blue event within the Mississippian reservoir. The cross section color scale is limited manually between -1 and +1 to emphasize the sign of the Intercept (A) values. The range of the Intercept (A) values extends beyond the color scale range of this cross section. Cross section location is Line A shown in Figure 3.3.

33
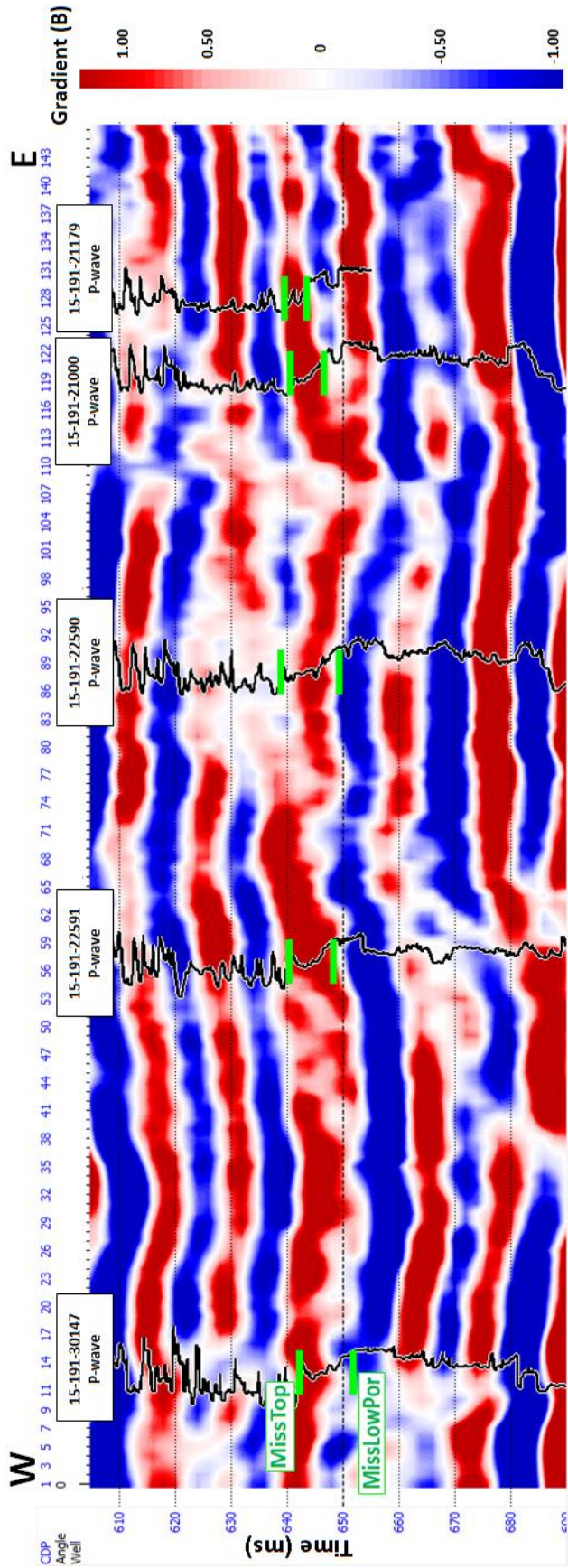
Figure 4.5. Gradient (B) cross section with P-wave sonic logs posted at the well locations. The Mississippian reservoir at all of the well locations has positive intercept (B) values indicated by the positive red event within the Mississippian reservoir. The cross section color scale is limited manually between -1 and +1 to emphasize the sign of the Gradient (B) values. The range of the Gradient (B) values extends beyond the color scale range of this cross section. Cross section location is Line A shown in Figure 3.3.

34
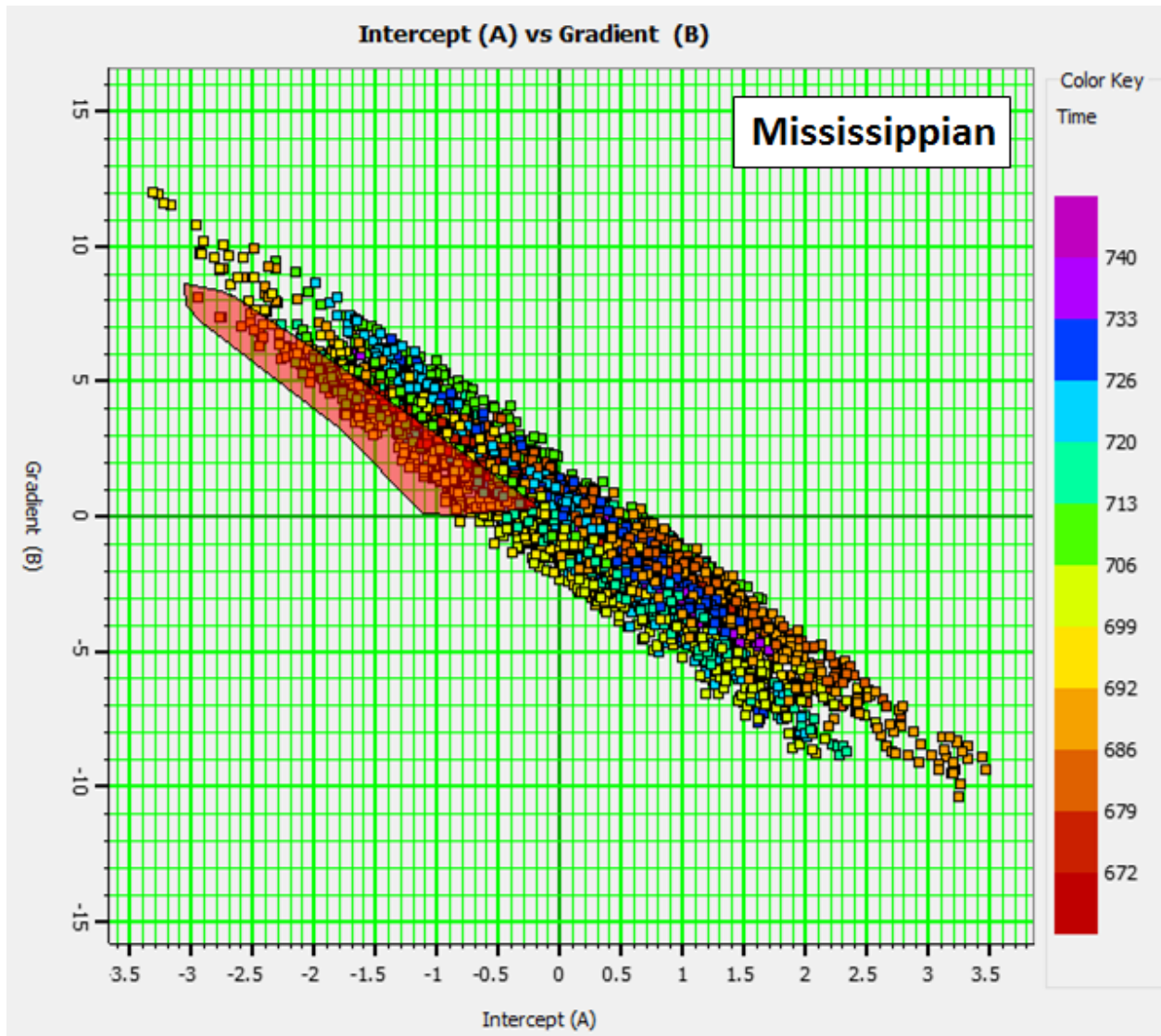
Figure 4.6. A-B crossplots within a 60 ms window around the Mississippian horizon. The red polygon highlights Class IV AVO crossplots.
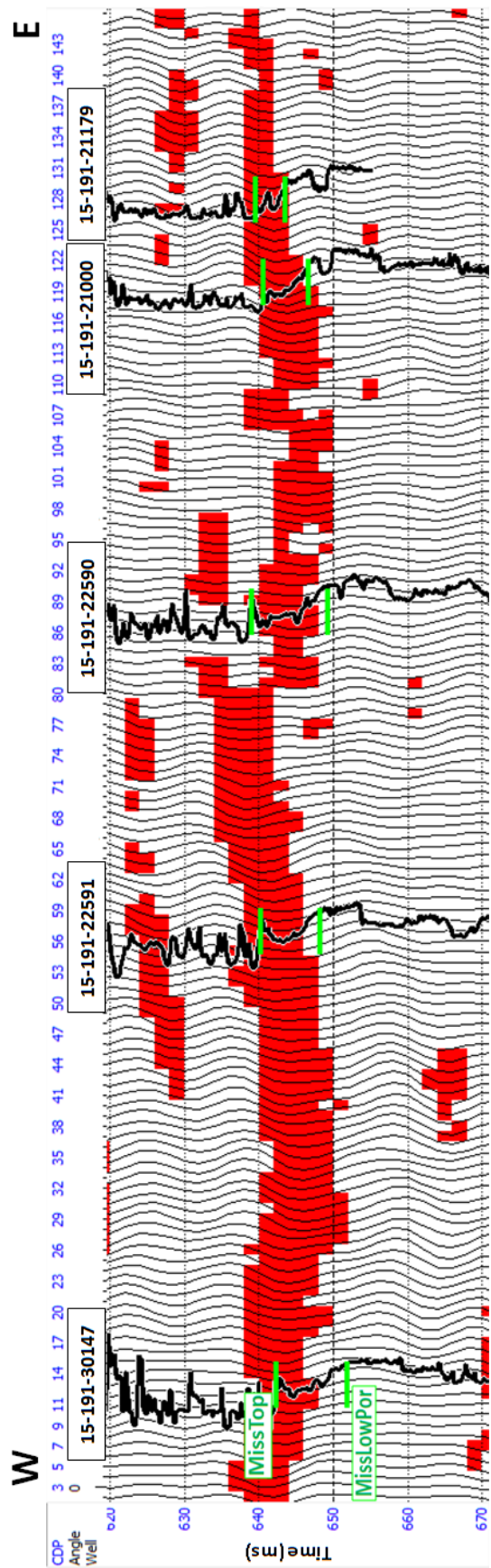
Figure 4.7. Class IV AVO highlighted zones on the seismic section that correspond to the A-B crossplots highlighted by the red polygon in Figure 4.6. Cross section location is Line A shown in Figure 3.3.

36

4.2: Arbuckle Porous Zones AVO Classification

The A-B crossplotting technique was used for identifying the AVO class of the porous zones in the Arbuckle. The porous zones in the Arbuckle show Class IV AVO response as well. The AVO class was determined by A-B crossplotting for the time window between the Arbuckle horizon and the Basement horizon (Figure 4.8). When the Class IV crossplots were highlighted, the porous zones were highlighted at the locations of wells #15-121-22591 and #15-121-22590. Figure 4.9a and Figure 4.10a show the corresponding highlighted zones of the crossplots in the red polygon in Figure 4.8 along seismic Inline #152 and Inline #169 with porosity logs posted at the well locations #15-121-22591 and #15-121-22590. The arrows point at the high porosity zones that were highlighted by the red polygon of Figure 4.8 where the porosity logs show high porosity values. The same highlighted zones show low impedance values in the P-impedance and S-impedance volumes that were created by the simultaneous AVO inversion of pre-stack data as described in section 5.1 (Figure 4.9b,c) and (Figure 4.10b,c).
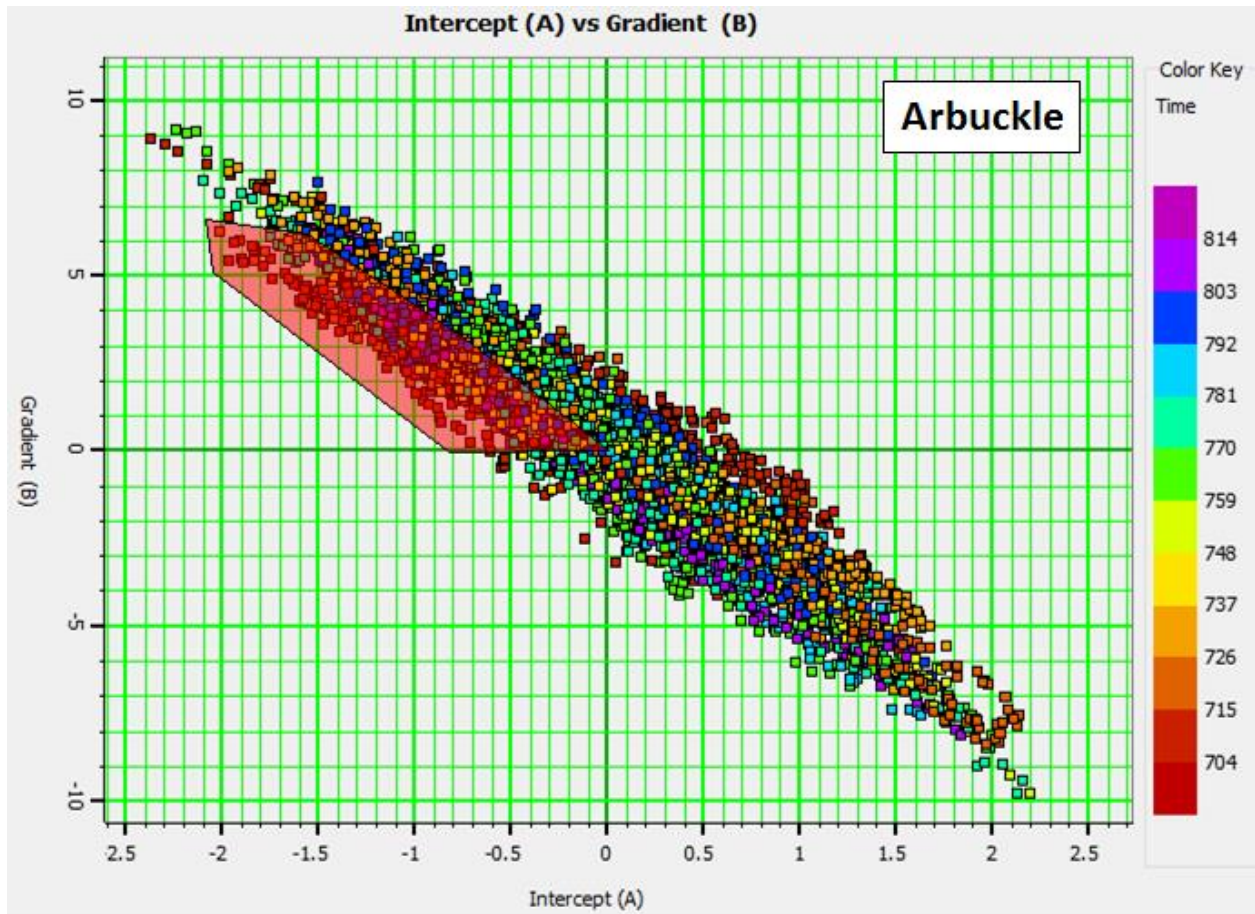
Figure 4.8. A-B crossplots of the time window between the Arbuckle top horizon and basement horizon. The red polygon highlights Class IV AVO crossplots.
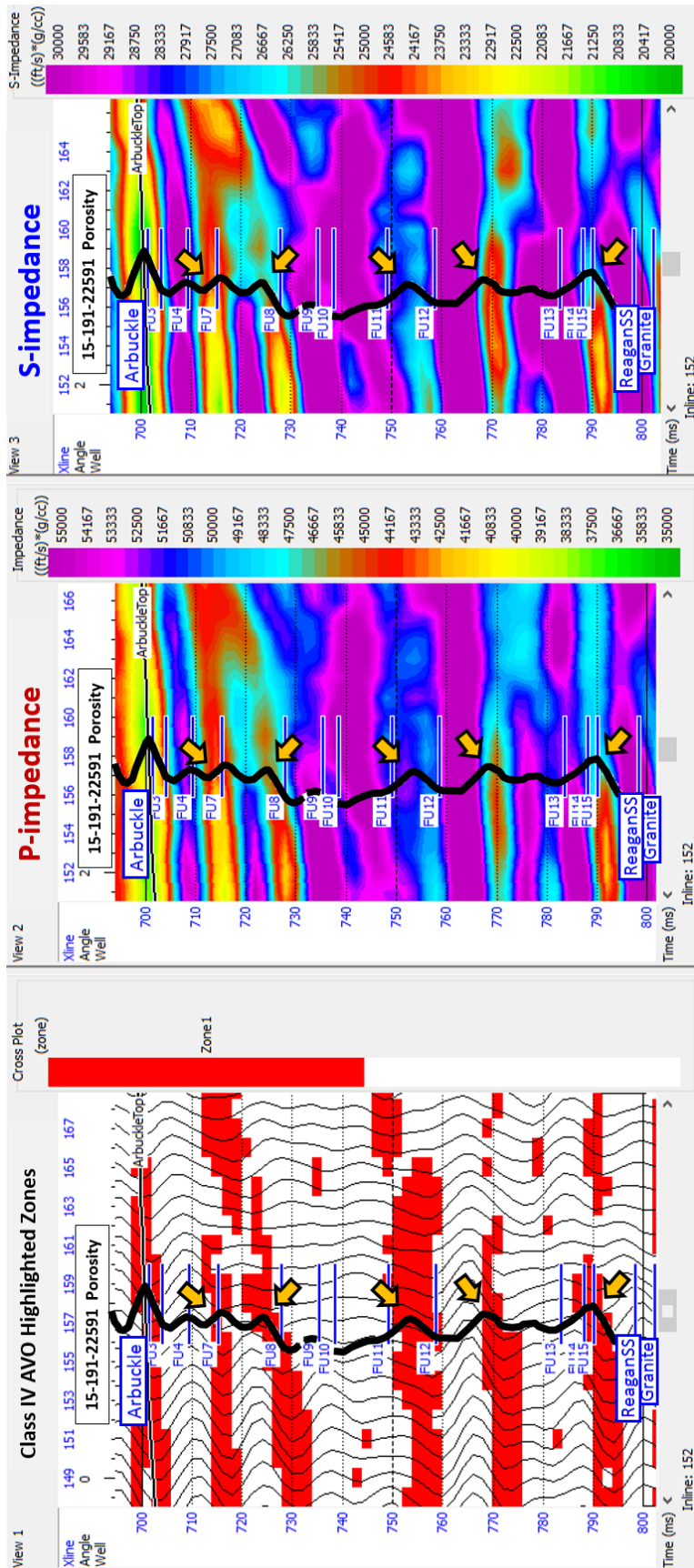
Figure 4.9. a) Class IV AVO highlighted zones on Inline #152 that correspond to the A-B crossplots highlighted by the red polygon in Figure 4.8. b) P-impedance (Z_P) inverted by simultaneous AVO inversion at Inline #152. c) S-impedance (Z_S) inverted by simultaneous AVO inversion at Inline #152. Black curves are formation porosity logs of well #15-121-22591. The arrows point at the high porosity zones on the porosity logs that were highlighted by the red polygon on the seismic sections. The same highlighted zones show low P-impedance and S-impedance.
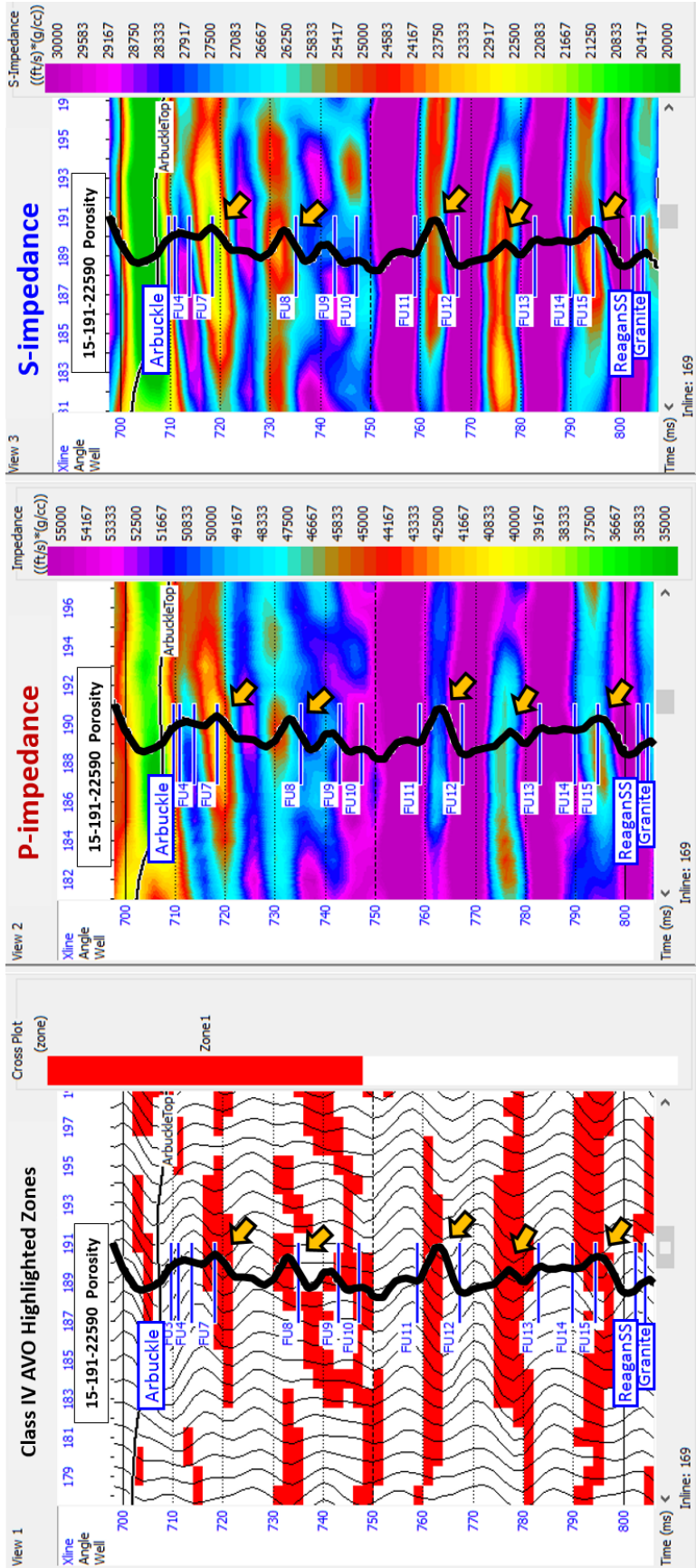
Figure 4.10. a) Class IV AVO highlighted zones on Inline #169 that correspond to the A-B crossplots highlighted by the red polygon in Figure 4.8. b) P-impedance (Z_P) inverted by simultaneous AVO inversion at Inline #169. c) S-impedance (Z_S) inverted by simultaneous AVO inversion at Inline #169. Black curves are formation porosity logs of well #15-121-22590. The arrows point at the high porosity zones on the porosity logs that were highlighted by the red polygon on the seismic sections. The same highlighted zones show low P-impedance and S-impedance.

CHAPTER 5: SIMULTANEOUS AVO INVERSION

5.1: Wellington Field Simultaneous AVO Inversion of Pre-stack Migrated Seismic Gathers

In a previous work on the Wellington Field by Sirazhiev (2012), model-based inversion was applied using the 3D post-stack seismic data to invert for P-impedance volume that was incorporated in the multi-attribute linear regression analysis for porosity prediction. In the present study the pre-stack migrated seismic gathers were used to apply the simultaneous AVO inversion method developed by Hampson et al. (2005). Simultaneous AVO inversion was applied to the pre-stack angle gathers after they were processed and converted from offset gathers to angle gathers as described in section 3.1 and appendices A, B and C. It is called simultaneous AVO inversion because it inverts for P-impedance (Z_P), S-impedance (Z_S) and density (ρ) at the same time, unlike the post-stack model-based inversion that inverts for P-impedance only.

Simultaneous AVO inversion in principle solves the equation written by Fatti et al. (1994) which describes the reflection amplitude change with angle θ in the pre-stack migrated seismic gathers in terms of P-wave reflectivity (R_P), S-wave reflectivity (R_S) and density reflectivity (R_D)

$$R_{PP}(\theta) = c_1 R_P + c_2 R_S + c_3 R_D \qquad (1)$$

Where

$$c_1 = 1 + tan^2\theta \qquad\qquad R_P = \frac{1}{2}\left[\frac{\Delta V_P}{V_P} + \frac{\Delta\rho}{\rho}\right]$$

$$c_2 = -8\gamma^2 sin^2\theta \qquad\qquad R_S = \frac{1}{2}\left[\frac{\Delta V_S}{V_S} + \frac{\Delta\rho}{\rho}\right]$$

$$c_3 = -\frac{1}{2}tan^2\theta + 2\gamma^2 sin^2\theta \qquad R_D = \frac{\Delta\rho}{\rho}$$

$$\gamma = \frac{V_S}{V_P}$$

This form of Fatti equation solves best for Z_P, but it does not solve as well for Z_S because the c_2 factor that defines the S-wave is smaller than the c_1 factor. Also, this form does not solve very well for density because the c_3 factor is very small (Simmons et al., 1996). To lower the effect of this problem, the Fatti equation is rewritten in a form that has independent variables to make the system more stable.

For obtaining the independent variables, we need first to define linear relationships between Z_P, Z_S and density using the well logs of wells #15-121-22591 and well #15-121-22590 (Hampson et al., 2005). The linear relationships were defined by the fit line of the crossplots of $\ln(Z_P)$ vs $\ln(\rho)$, and the fit line of the crossplots of $\ln(Z_S)$ vs $\ln(Z_P)$ (Figure 5.1). The relationships are described by the following two equations written by Hampson et al. (2005):

$$\ln(Z_S) = k * \ln(Z_P) - k_c + \Delta L_S \qquad (2)$$

Where, $k = 1.073$
$k_c = 1.36$
$\Delta L_S = $ the deviation away from the stright line

$$\ln(\rho) = m * \ln(Z_P) - m_c + \Delta L_D \qquad (3)$$

where, m $= 0.303$
$m_c = 2.29$
$\Delta L_D = $ the deviation away from the straight line

The deviations away from the straight lines, shown as ΔL_S and ΔL_D in figure 5.1, are the desired fluid anomalies. ΔL_S and ΔL_D are independent variables of $\ln(Z_P)$, unlike $\ln(Z_S)$ and $\ln(\rho)$. Using these independent variables, it was shown by Hampson et al., (2005) that the Fatti equation can be written alternatively in a way that describes the seismic traces at each angle in the angle gathers

$$s_\theta = \hat{c}_1 W_\theta D L_P + \hat{c}_2 W_\theta D \Delta L_S + W_\theta c_3 D \Delta L_D \qquad (4)$$

Where,

$\hat{c}_1 = (1/2)c_1 + (1/2)kc_2 + mc_3$

$\hat{c}_2 = (1/2)c_2$

$W(\theta) = $ wavelet at angle θ

$D = $ Derivative operator

$L_P = \ln(Z_P)$

The simultaneous AVO inversion started with low frequency initial Z_P, Z_S and density model volumes that were created using the P-impedance and S-impedance and density logs of wells #15-121-22591 and #15-121-22590. The well logs were low-pass filtered with a high cut of 15 Hz. Then, the low pass filtered well log curves were interpolated around the seismic survey area using the horizons, which were interpreted on the post-stack seismic data, to create a low frequency initial trace at each CDP in the survey area.

Using equation (4), synthetic seismic gathers were created at each CDP by convolving the reflectivity of the initial Z_P, Z_S and density models with angle-dependent wavelets that were extracted from the real seismic gathers. The initial models values were changed simultaneously and iteratively until the synthetic gathers matched the real gathers with the smallest least-squared error (Hampson et al., 2005).

Before applying the inversion to the entire seismic volume, simultaneous AVO inversion was evaluated at wells #15-121-22591 and #15-121-22590 by comparing the inverted Z_P, Z_S and density with the original well logs (Figures 5.2-5.3). The red curves are the inverted logs, the blue curves are the real well logs, and the black smooth curves are the initial low-frequency models from which simultaneous AVO inversion starts. There is generally a good agreement between the real and inverted logs. The correlation between the red synthetic seismic gather of the red inverted logs with the black real seismic gather is 0.93 at well #15-121-22590 and 0.91 at well #15-121-22591 (Figures 5.2-5.3). Based on this good agreement, the simultaneous AVO

inversion was applied to the gathers of the 3D seismic data set to create Z_P, Z_S, and density

volumes. The inversion results were evaluated within the Mississippian chert reservoir and the

Arbuckle Group.
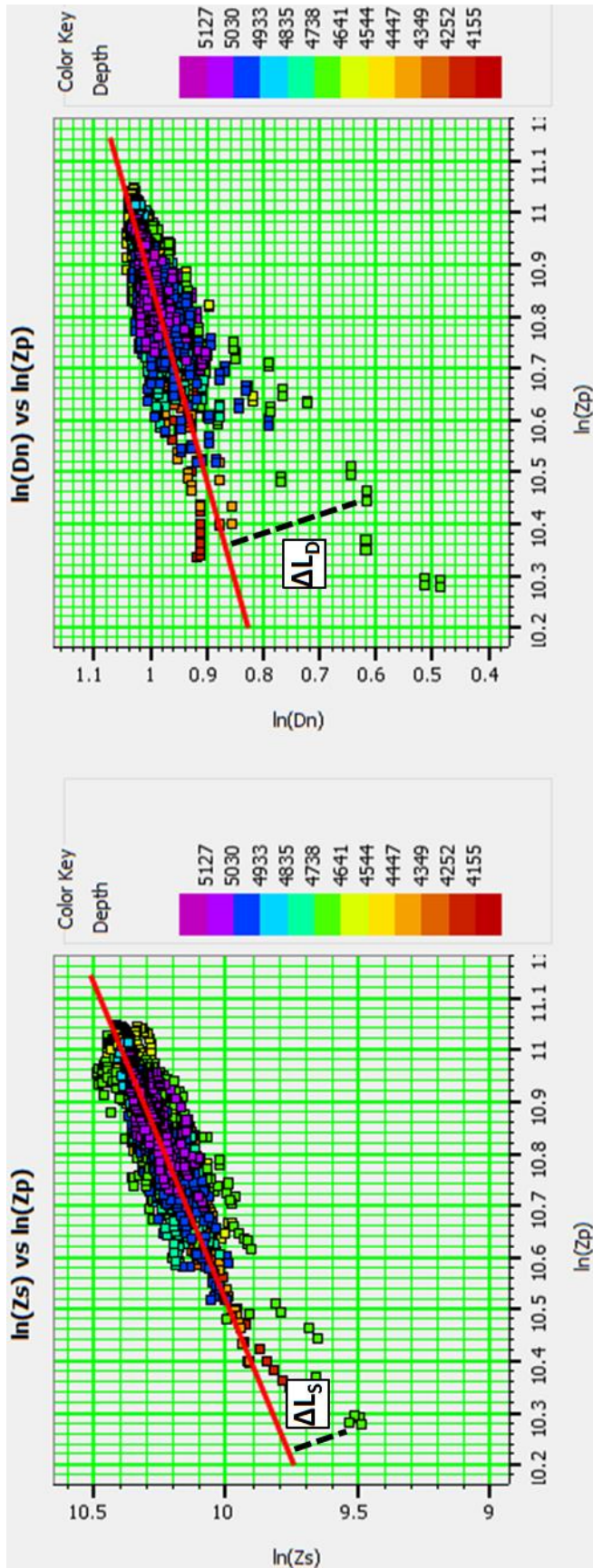
Figure 5.1: Cross plots of $\ln(\rho)$ vs. $\ln(Z_P)$ and $\ln(Z_S)$ vs. $\ln(Z_P)$ calculated from the logs of wells #15-121-22591 and #15-121-22590. The deviations away from the best fit lines, ΔLD and ΔLS, are the desired fluid anomalies which are independent of $\ln(Z_P)$.
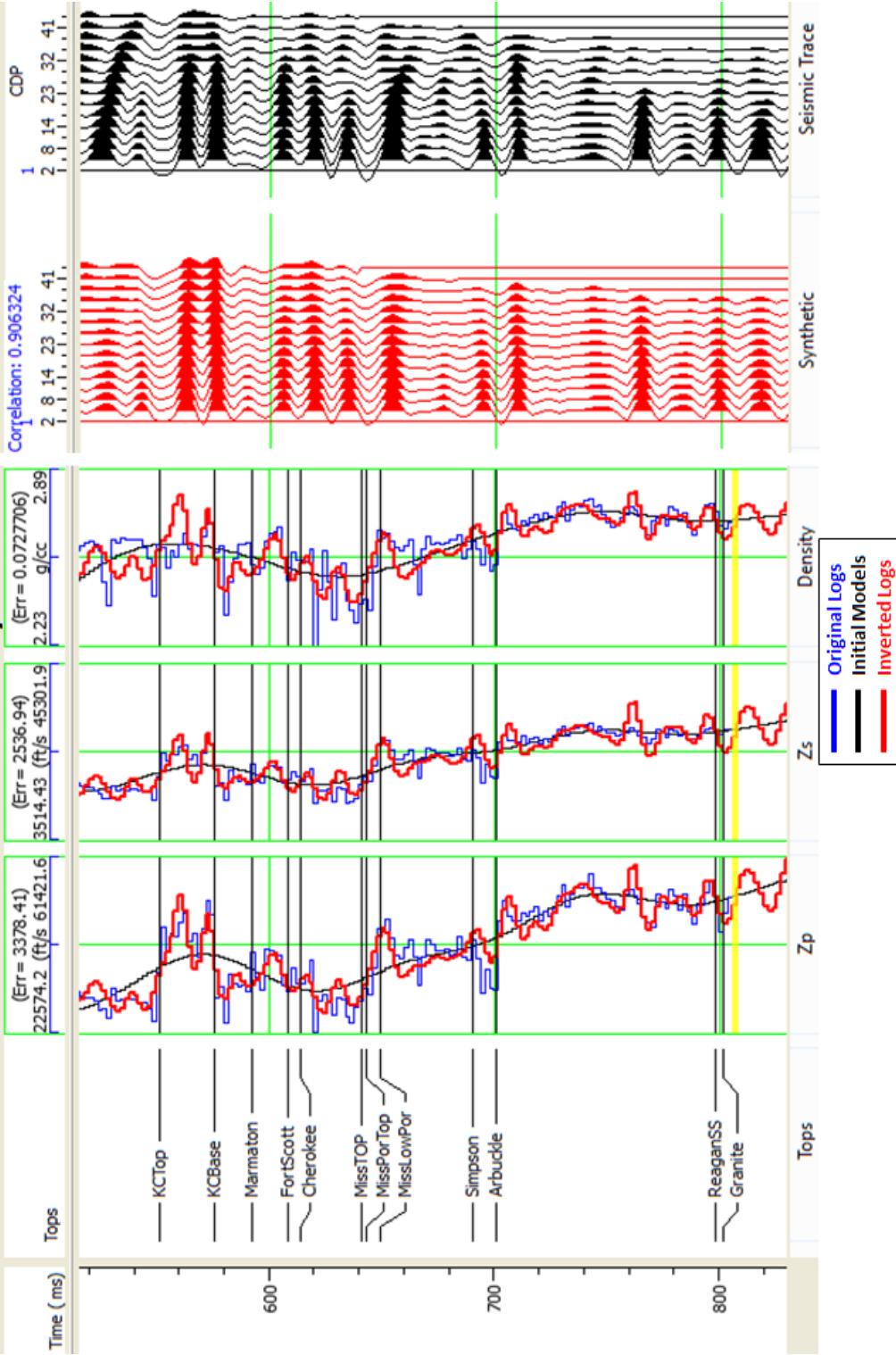
Figure 5.2. Analysis of simultaneous AVO inversion at well location #15-191-22591. From left to right: 1) Well tops. 2) Inverted traces (red), original well logs (blue) and initial models (black) of Z_P, Z_S and density. 3) Synthetic seismic gather (red) 4) Real seismic gather (black). The inverted traces (red) show a good match with the original logs (blue). The synthetic seismic gather shows a high correlation of 0.91 with the real seismic gather (black) at the well location. Synthetic and seismic traces are displayed in SEG reversed polarity.
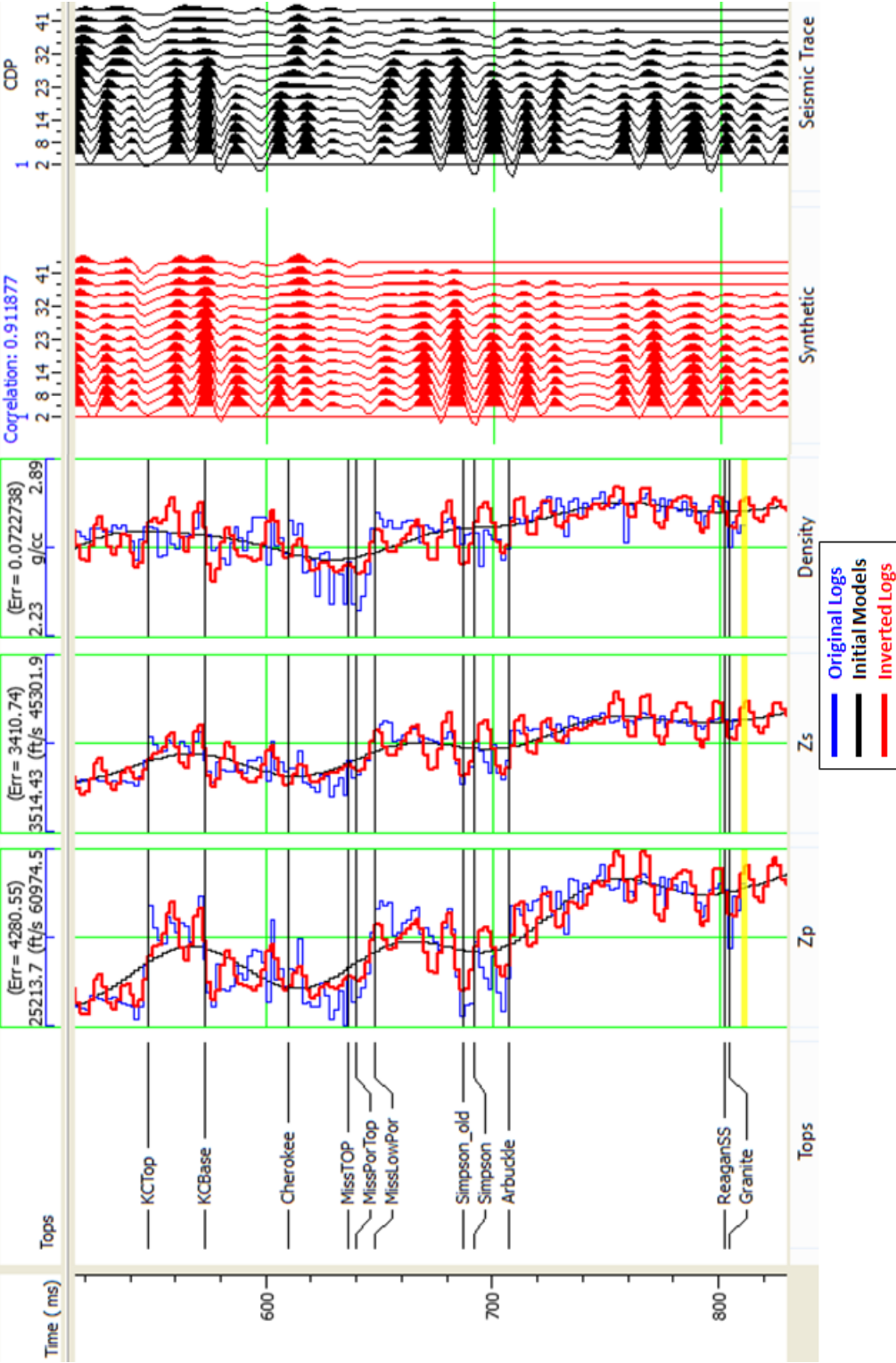
Figure 5.3. Analysis of simultaneous AVO inversion at well location #15-191-22590. From left to right: 1) Well tops. 2) Inverted traces (red), original well logs (blue) and initial models (black) of Z_P, Z_S and density. 3) Synthetic seismic gather (red) and initial models (black) of Z_P, Z_S and density. 3) Synthetic seismic gather (red) 4) Real seismic gather (black). The inverted traces (red) show a good match with the original logs (blue). The synthetic seismic gather shows a high correlation of 0.93 with the real seismic gather (black) at the well location. Synthetic and seismic traces are displayed in SEG reversed polarity.

5.2: Simultaneous AVO Inversion Evaluation within the Mississippian Reservoir

The simultaneous AVO inversion for Z_P and density was evaluated within the Mississippian reservoir at the eleven wells that have a good tie to the seismic data and have P-impedance and density logs. The evaluation was done by comparing inverted seismic traces at these well locations with the original well logs. Inverted Z_S, however, was evaluated within the Mississippian reservoir at wells #15-191-22591 and #15-191-22590 because they are the only wells that have original S-impedance logs.

Figure 5.4 shows inverted Z_P traces (red) and original P-impedance logs (black) at the eleven well locations. As mentioned earlier, the gradational downward porosity decrease within the Mississippian reservoir results in a corresponding increase in acoustic impedance. Therefore, the Mississippian reservoir corresponds to the transitional impedance boundary marked by the blue lines in figure 5.4. The inverted Z_P traces and the original P-impedance logs show generally good agreement within the Mississippian reservoir with an overall 0.85 correlation coefficient and RMS inversion error of 953 (m/s)*(g/cc). Figure 5.5 is a crossplot of the inverted Z_P traces against the original P-impedance logs within the Mississippian reservoir at the eleven well locations showing a best fit line that has a slope of 0.91. The linear relationship between the inverted and the original P-impedances supports the good agreement between them. A few outliers shifted away from the best fit line due to the high impedance parts at the reservoir base that were underestimated by inversion as visually evident for wells #15-121-21581, #15-121-20789 and #15-121-21255 (Figure 5.4). For a quick comparison between the simultaneous AVO inversion and post-stack model-based inversion results, the post-stack model-based inverted P-impedance traces were crossplotted against the original P-impedance well logs for the same group of wells (Figure 5.6). The crossplot shows a lower overall correlation of 0.77 with higher

RMS inversion error of 1080 (m/s)*(g/cc), and a best fit line that has a lower slope of 0.76 indicating less agreement between the post-stack model-based inversion traces and the original logs.

Figure 5.7 is a cross section at Line A of inverted Z_P by simultaneous AVO inversion. The posted P-impedance well logs show the ramp-transition within the Mississippian reservoir from the overlying low impedance rocks to the underlying high impedance rocks. The inverted Z_P cross section shows the expected impedance variation around and within the Mississippian reservoir (Figure 5.7). By referring to the impedance color scale in Figure 5.7, the cross section shows that impedance changes from green to yellow at the top of the Mississippian reservoir. Then, impedance changes gradually downward from yellow to red within the Mississippian until it becomes blue at the base of the reservoir. So, inverted Z_P provides good contrast at the top and the bottom of the Mississippian reservoir that helps in picking the top and the base of the Mississippian reservoir. However, it becomes challenging to determine the top of the Mississippian reservoir on the inverted Z_P data at some places where the overlying layer has impedance values that are equal to the impedance values at the top of the Mississippian reservoir such as the location of well #15-121-22590.

In Figure 5.8a the inverted Z_S traces (red) show a good match with the well S-impedance logs (black) within the Mississippian reservoir at wells #15-191-22591 and #15-191-22590. The inverted Z_S and original S-impedance logs have an overall correlation of 0.93 for both wells. Because inverted Z_S was only analyzed at wells #15-191-22591 and #15-191-22590, another evaluation was done for inverted Z_P within the Mississippian reservoir at only these two wells to compare it with inverted Z_S (Figure 5.8b). Inverted Z_P shows a correlation of 0.94 for both wells indicating that inverted Z_S and inverted Z_P results are similar in quality. The inverted Z_S cross

section of Line A in Figure 5.9 shows the same details depicted in the Z_P impedance cross section of Line A (Figure 5.7).

The inverted density traces at the Mississippian reservoir show generally that they have the same trends with the densities measured by the original well logs, however the results were not as good as those observed fro the Z_P and Z_S impedance inversions (Figure 5.10). The inverted and real densities at the Mississippian reservoir show an overall correlation of 0.65. Therefore, the inverted and the real density crossplots are more scattered as shown in Figure 5.11. The reduced quality of density estimation by inversion might be due to the fact that density recovery mainly depends on the far offsets amplitudes that are usually affected by noise and wave attenuation (Chopra et al., 2010). The inverted density cross section of Line A in Figure 5.12 shows gradation within the Mississippian that is consistent with ramp-transition of density as shown on the overlain density logs. However, the density cross section is not expected to show density values that are close to the real density values as illustrated by the crossplot in figure 5.11. Also, the density cross section shows weaker contrast at the top of the Mississippian reservoir. Therefore, inverted density would not be efficient for picking the top of the Mississippian reservoir.
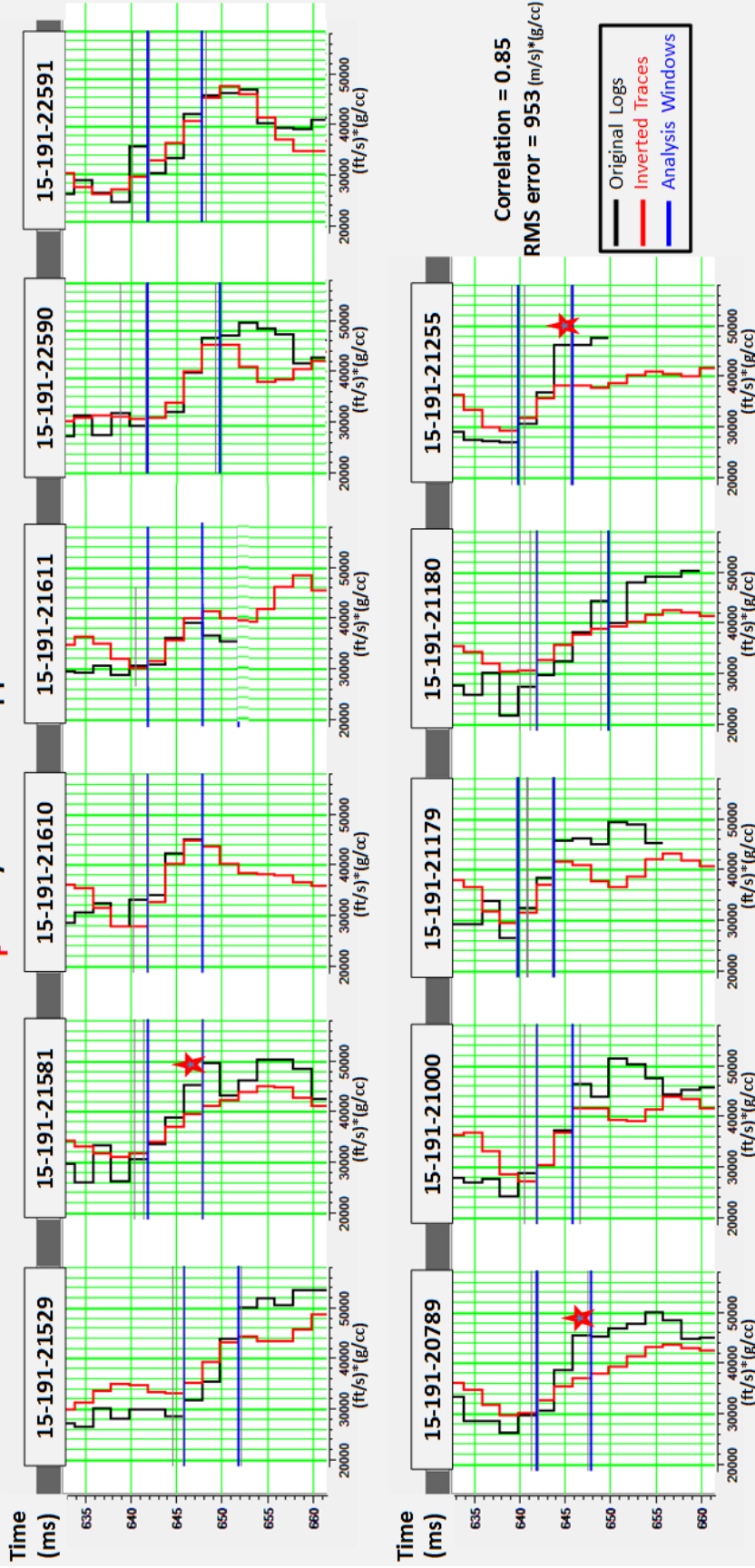
Figure 5.4. Analysis of inverted Z_P by simultaneous AVO inversion within the Mississippian chert reservoir (shown by the blue horizontal lines of the analysis window) at 11 well locations. The inverted Z_P traces (red) show a good agreement with the original P-impedance logs (black) with an overall correlation of 0.85 for all wells. The total RMS error for all wells is 953 $(m/s)*(g/cc)$. Red stars mark the underestimated high impedance parts near the reservoir base as discussed in section 5.2.

51
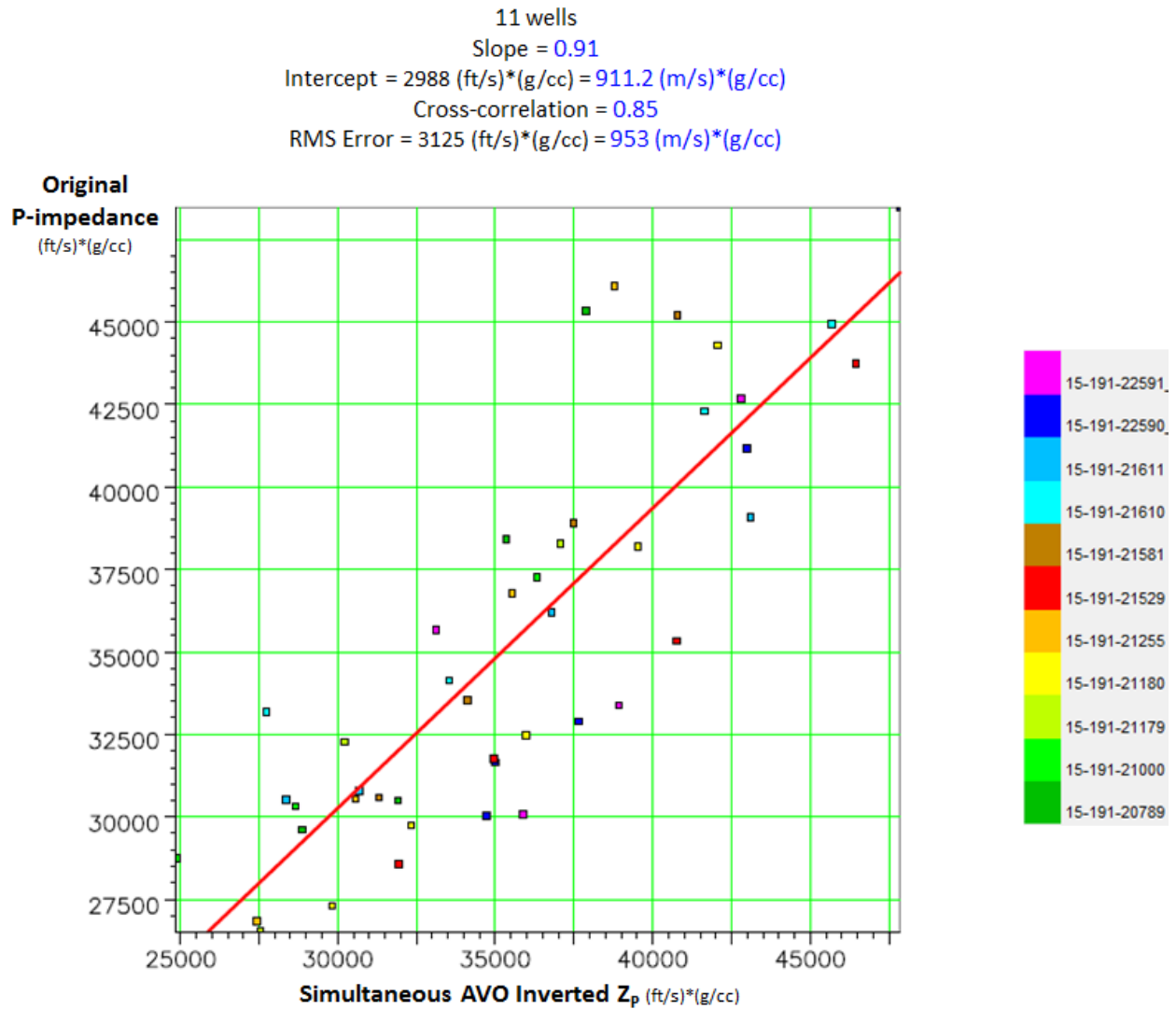
Figure 5.5. Crossplot of the inverted Z_P by simultaneous AVO inversion versus the original P-impedance logs within the Mississippian chert reservoir (the analysis window shown with blue horizontal lines in Figure 5.4) at 11 well locations. The red line shows the line of perfect correlation between inverted and original P-impedance values. The total RMS error for the 11 wells is 953 (m/s)*(g/cc).
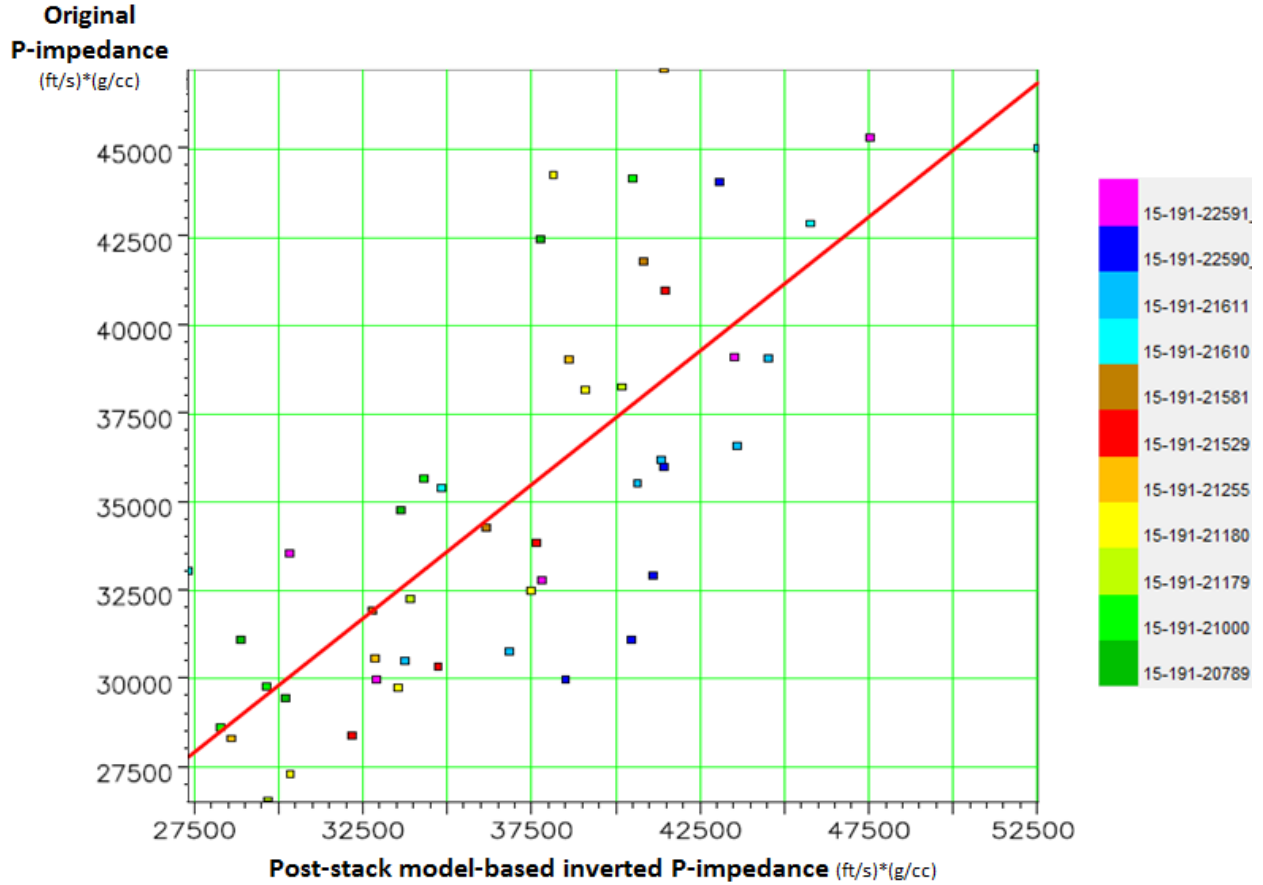
Figure 5.6. Crossplot of the inverted P-impedance by post-stack model-based inversion versus the original P-impedance logs within the Mississippian chert reservoir at 11 well locations. The red line shows the line of perfect correlation between inverted and original P-impedance values. The total RMS error for the 11 wells is 1080 (m/s)*(g/cc).
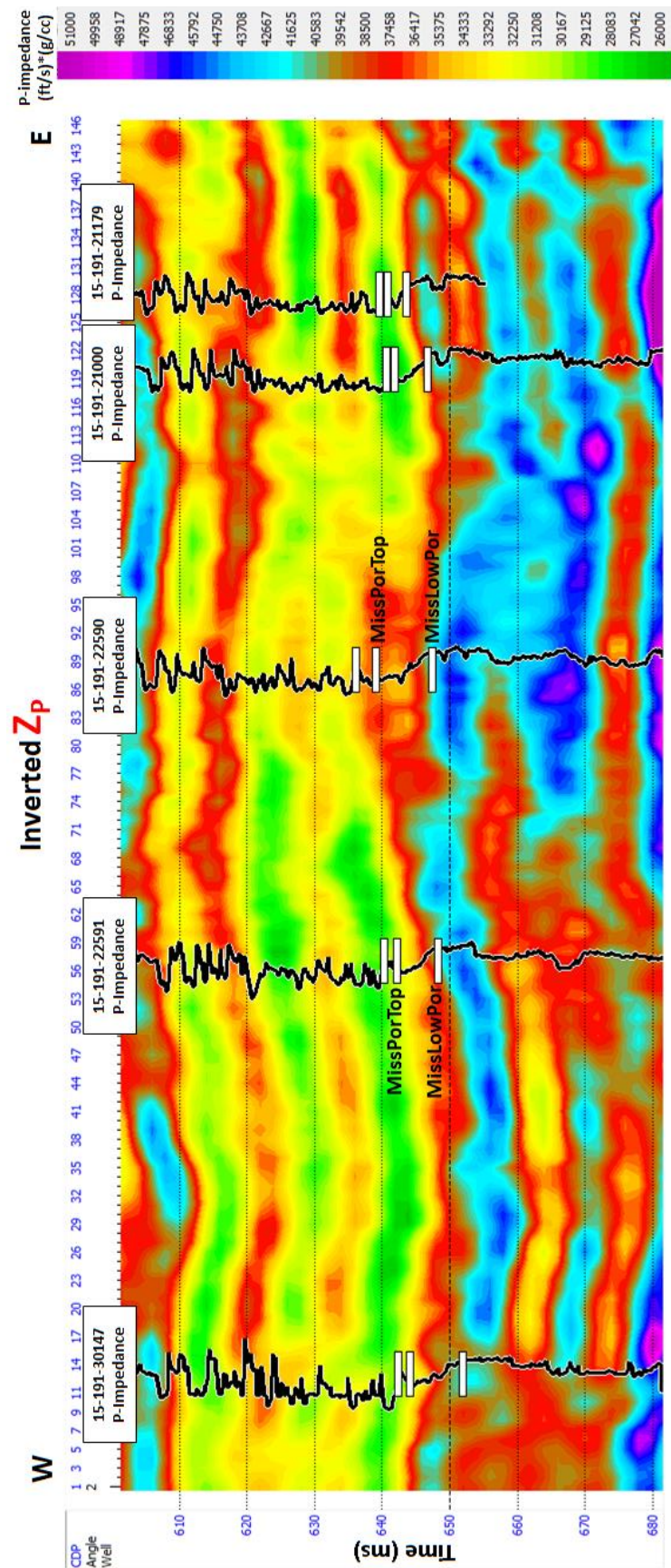
Figure 5.7. Simultaneous AVO inverted Z_P cross section with P-impedance well logs posted at well locations. Cross section location is Line A shown in Figure 3.3.
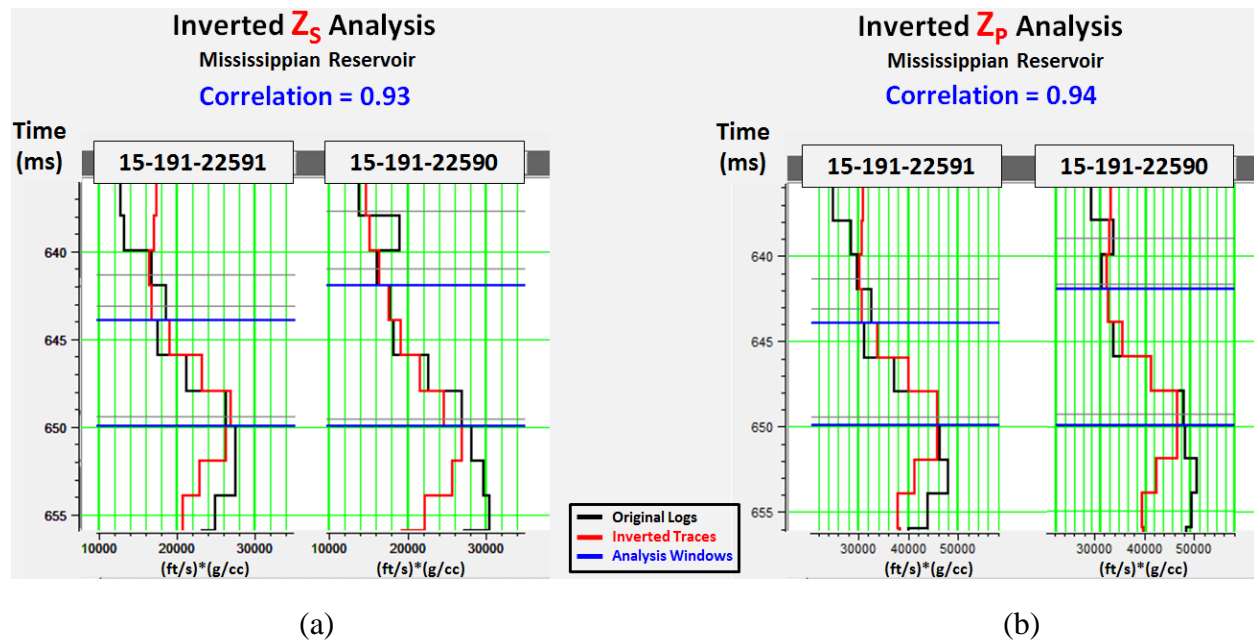
Figure 5.8. a) Analysis of inverted Z_S by simultaneous AVO inversion within the Mississippian chert reservoir at wells #15-191-22591 and #15-191-22590. b) Analysis of inverted Z_P by simultaneous AVO inversion within the Mississippian chert reservoir at wells #15-191-22591 and #15-191-22590.
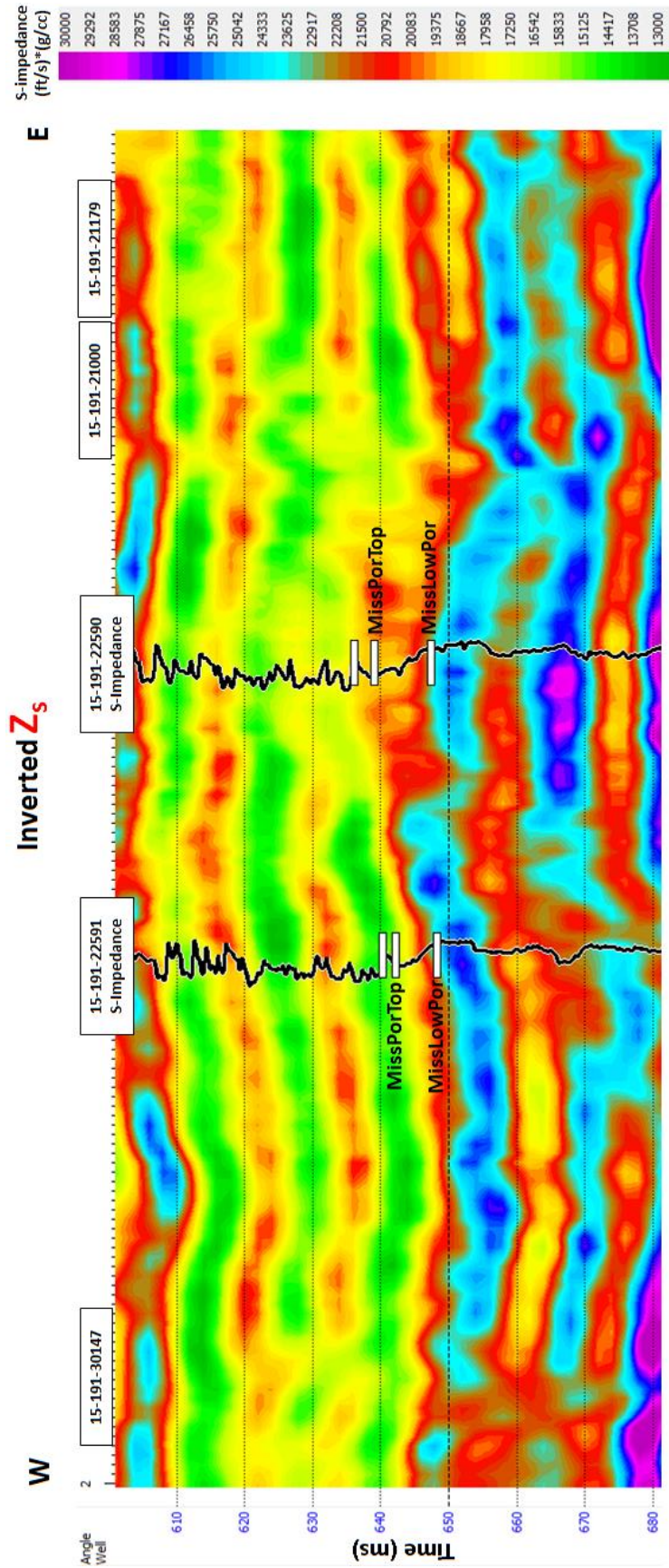
Figure 5.9. Simultaneous AVO inverted Z_S cross section with S-impedance well logs posted at well locations. Cross section location is Line A shown in Figure 3.3.
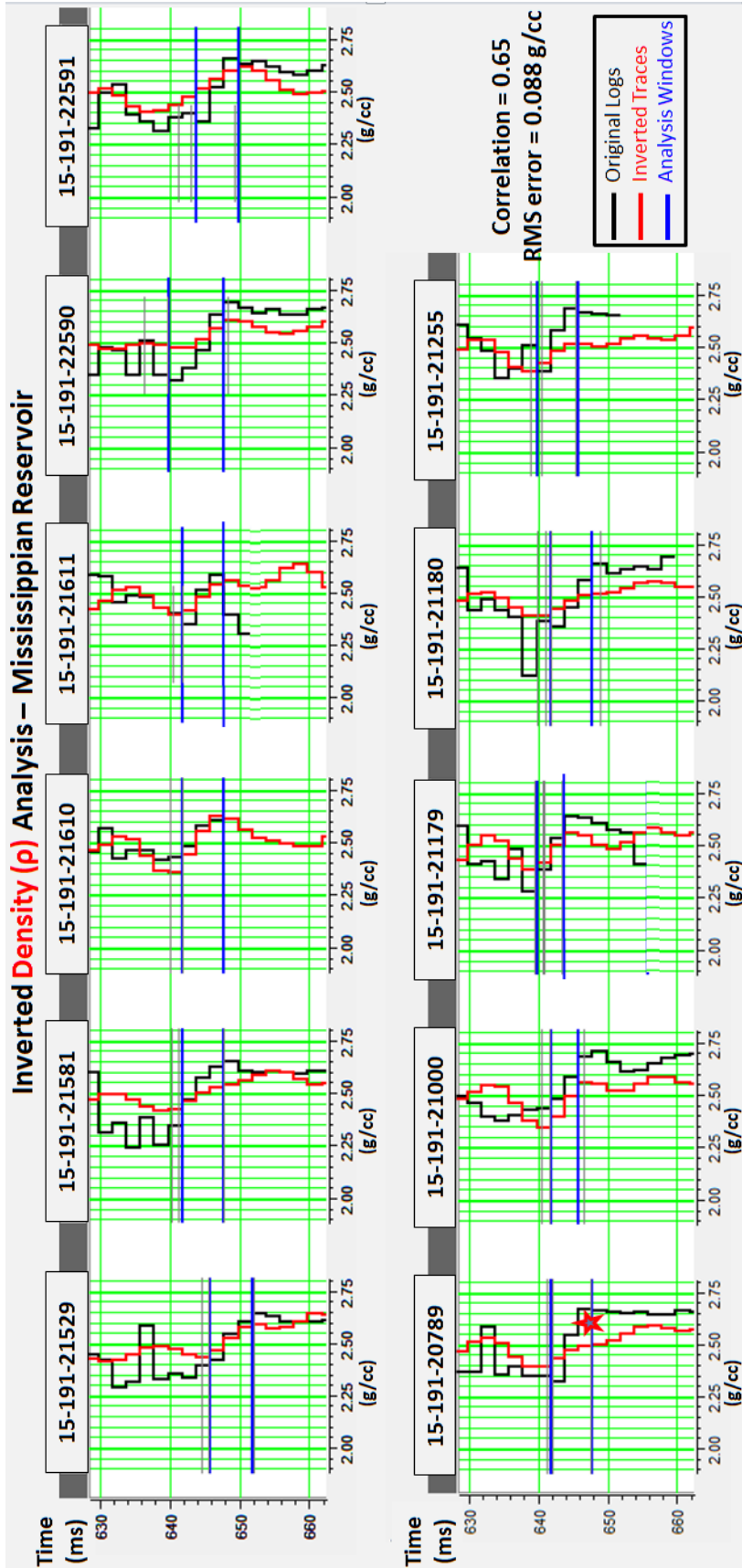
Figure 5.10. Analysis of the inverted density by simultaneous AVO inversion within the Mississippian chert reservoir (shown by the blue horizontal lines of the analysis window) at 11 well locations. Inverted densities have the same trends of the original densities with less agreement than that of inverted Z_P and Z_S impedances with original wells logs (Figure 5.4) and (Figure 5.8). The inverted and original densities at the Mississippian show an overall correlation of 0.65.
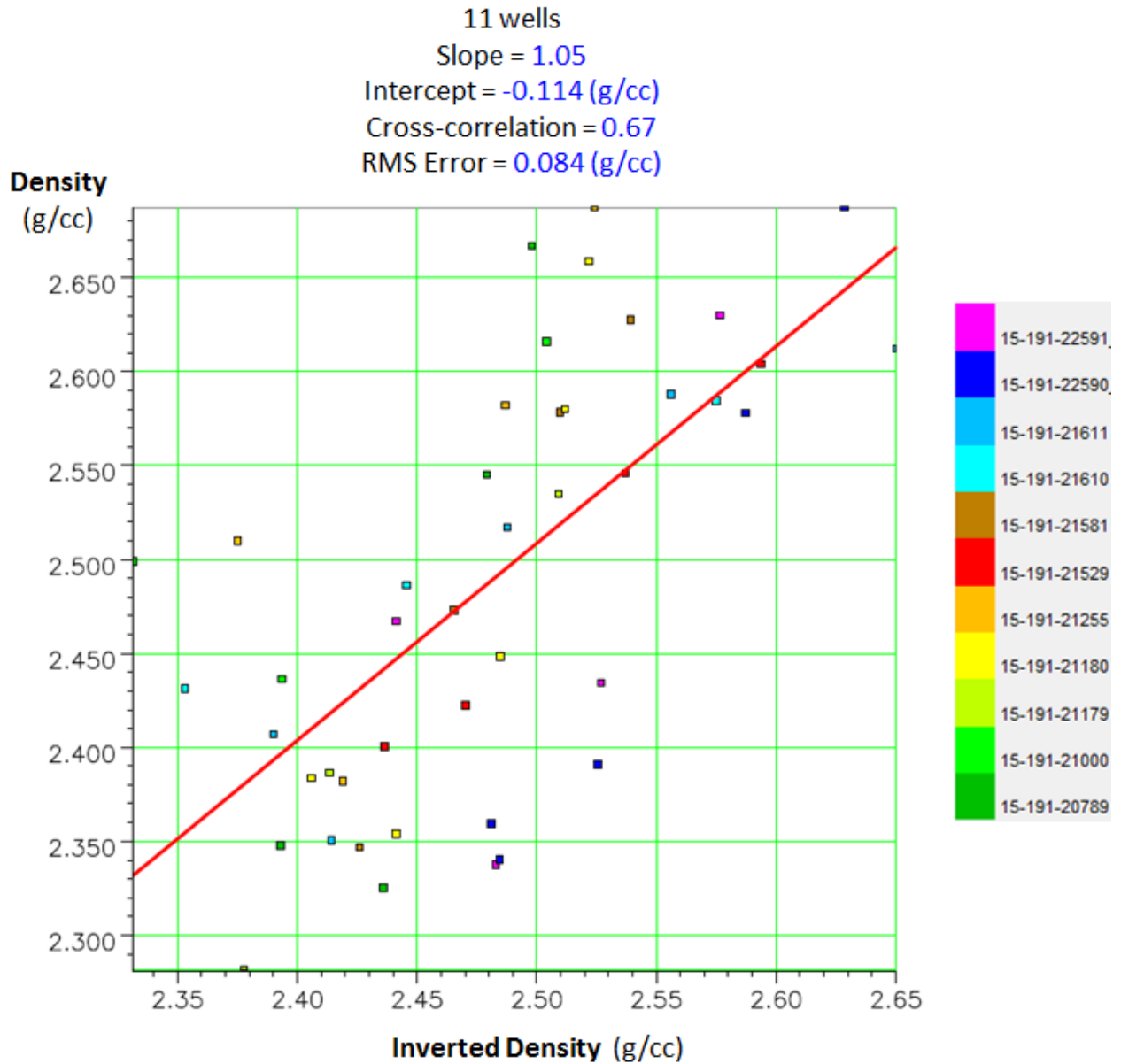
Figure 5.11. Crossplot of the inverted density by simultaneous AVO inversion versus the original density logs within the Mississippian chert reservoir at 11 well locations. The inverted and original densities crossplots are more scattered than the crossplots of inverted and original impedances indicating less quality of density recovery by inversion.
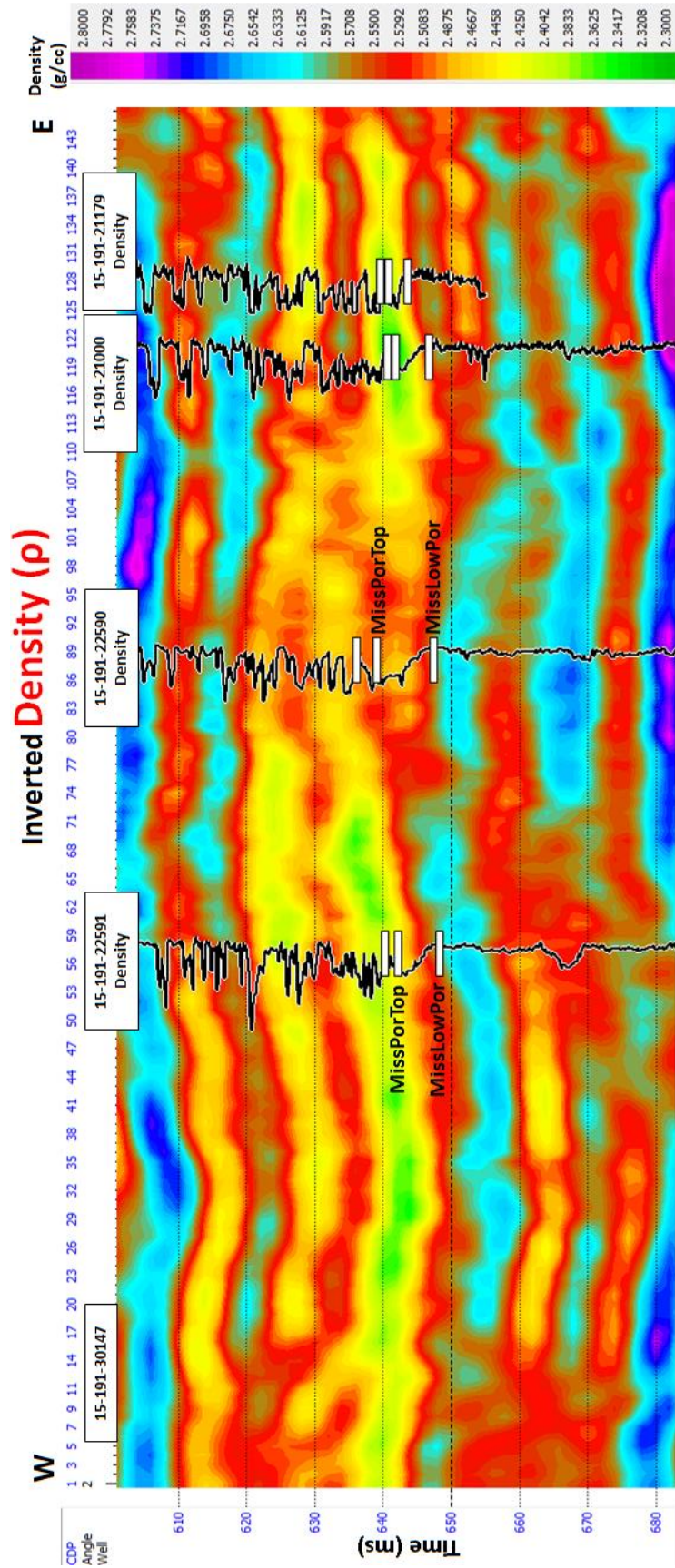
Figure 5.12. Simultaneous AVO inverted density cross section with density well logs posted at well locations. Cross section location is Line A shown in Figure 3.3.

5.3: Simultaneous AVO inversion of Synthetic Wedge Model of the Mississippian Reservoir

A wedge model was created using the P-wave, S-wave and density logs of well #15-121-22590 to test the power of recovering impedance values using simultaneous AVO inversion within a reservoir characterized by downward gradational porosity decrease and downward velocity increase such as the Mississippian reservoir in the Wellington Field. The original thickness of the Mississippian reservoir at well #15-121-22590 is about 15 m. In the wedge model, the Mississippian reservoir was stretched and squeezed so that the Mississippian reservoir has an increasing thickness from 0 to 60 m. The wedge model was made by creating 61 P-wave, S-wave and density logs from well #15-121-22590 with modified thicknesses of the Mississippian reservoir starting from a thickness of 0 m up to 60 m with 1 m thickness increment from one well to the other. Then, these logs were used to make depth-velocity models with 1 m separation between each model on a single line. The depth-velocity models were convolved with the statistical wavelet extracted earlier from the Wellington seismic data to create synthetic pre-stack seismic angle gathers (0 to 45 degrees) at the locations of the depth-velocity models (Figure 5.13).

For applying the simultaneous AVO inversion to the synthetic wedge mode gathers, initial Z_P, Z_S and density models were built using only the low-pass filtered original logs of well #15-121-22590 that were interpolated by three horizons interpreted on post-stack seismic section of the wedge model. Simultaneous AVO inversion was applied to the wedge model as explained earlier in Section 5.1 to invert for Z_P, Z_S and density wedge models.

Since inverted Z_P provided the best results as demonstrated in section 5.2, it was sufficient to evaluate the inversion applied using inverted Z_P only (Figure 5.14). The inverted Z_P was evaluated at each trace location of the wedge model because the P-impedance well logs were

available at all of the trace locations. Figure 5.15 is a crossplot of the RMS inversion error calculated within the Mississippian reservoir versus the wedge thickness.

Figure 5.16 shows inverted Z_P traces and P-impedance well logs for the wedge thickness range 0-8 m. At 0 m reservoir thickness, the inverted Z_P trace shows a step velocity function that represents a sharp impedance boundary. Starting from 1 m thickness, inverted Z_P shows a transitional impedance boundary that has a constant time thickness for reservoir thicknesses between 1-4 m as shown between the blue markers in Figure 5.16. In the transitional zone between the blue markers for reservoir thicknesses 1-4 m, there is a noticeable separation between the real and inverted values which resulted in the high RMS error for thicknesses between 1-4 m as shown in Figure 5.15. So, a transitional layer can exist for reservoir thicknesses 1-4 m in the inverted impedance cross section indicating the presence of the reservoir, but it does not provide reliable thickness or reliable impedance values within this thickness range. As thickness increases, the agreement between inverted and real impedances improves, and the inversion RMS error decreases (Figures 5.15 – 5.17). The inversion RMS error decreases dramatically at the reservoir thickness of 5 m, and the RMS error keeps decreasing as thickness increases until the error starts having steady RMS error with slight variations from the reservoir thickness of 10 m Figure 5.15. The inverted and real impedances have almost similar values for reservoir thicknesses that are greater than or equal to 10 m, which correspond to thicknesses that are greater than or equal to $1/8\lambda$ in terms of wavelength (Figure 5.15 – 5.17).
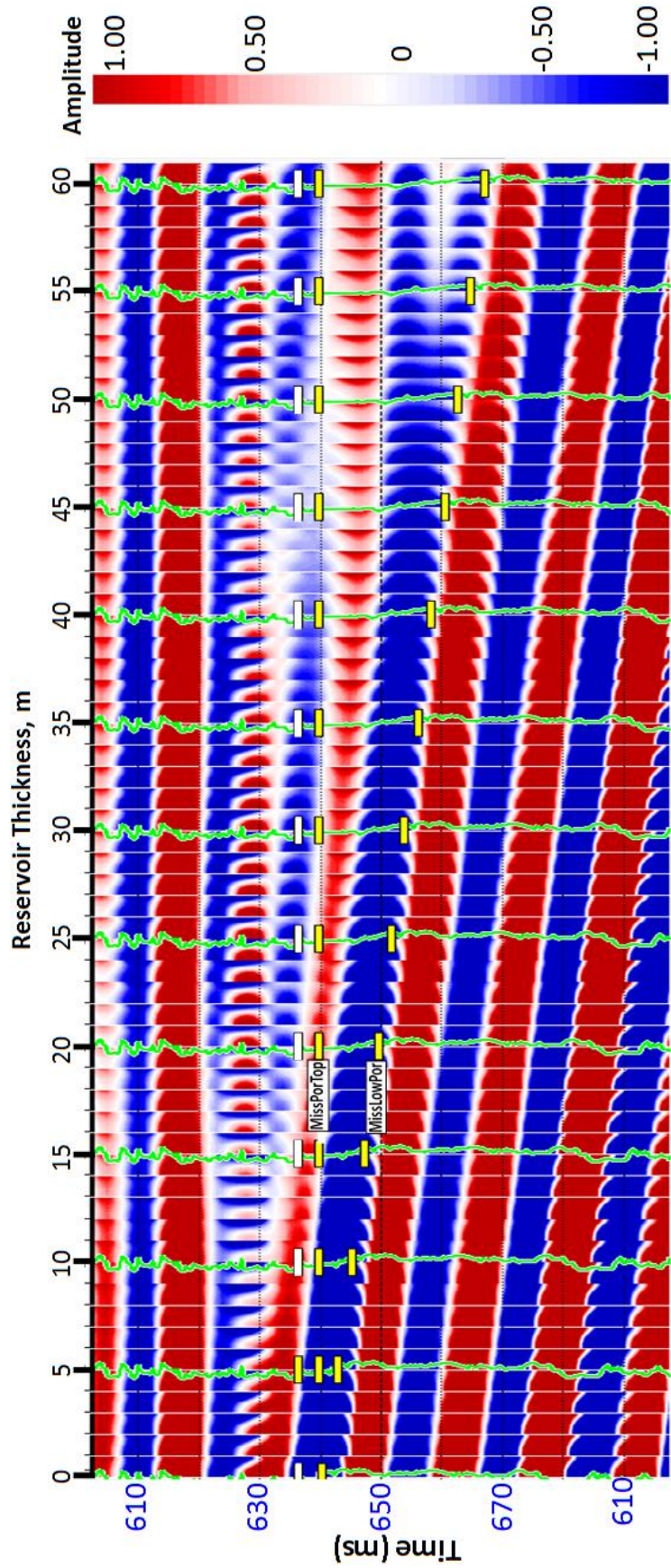
Figure 5.13. Synthetic seismic gathers section of the Mississippian reservoir wedge model constructed at well #15-191-22590. Synthetic P-wave sonic logs calculated by stretching and squeezing the original log within the Mississippian reservoir are shown in light green for every 5th trace (original reservoir thickness is 15 m). Well top shown in white – MissTop, the top of the reworked Mississippian chert; well tops shown in yellow – MissPorTop and MissLowPor, the top and the base of the chert reservoir.

62
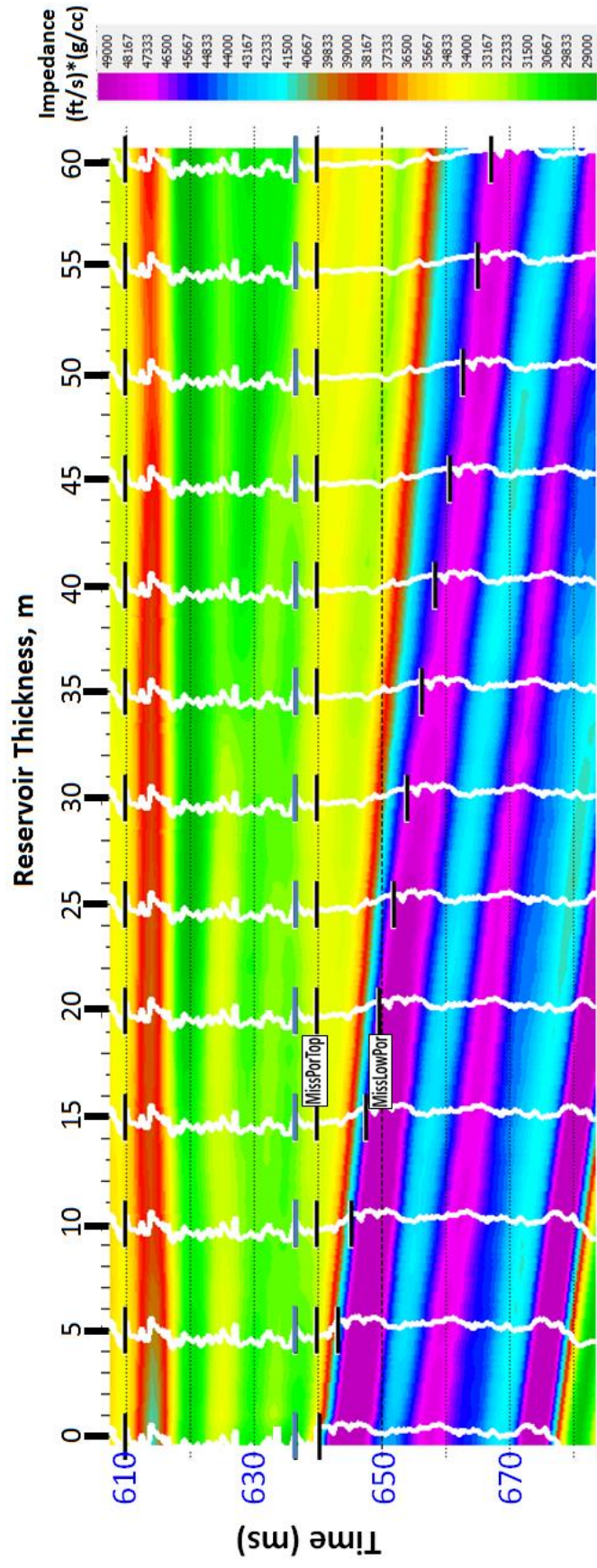
Figure 5.14. Wedge model inverted Z_P by simultaneous AVO inversion of the synthetic gathers in Figure 5.13. P-impedance logs are shown for every 5th trace.
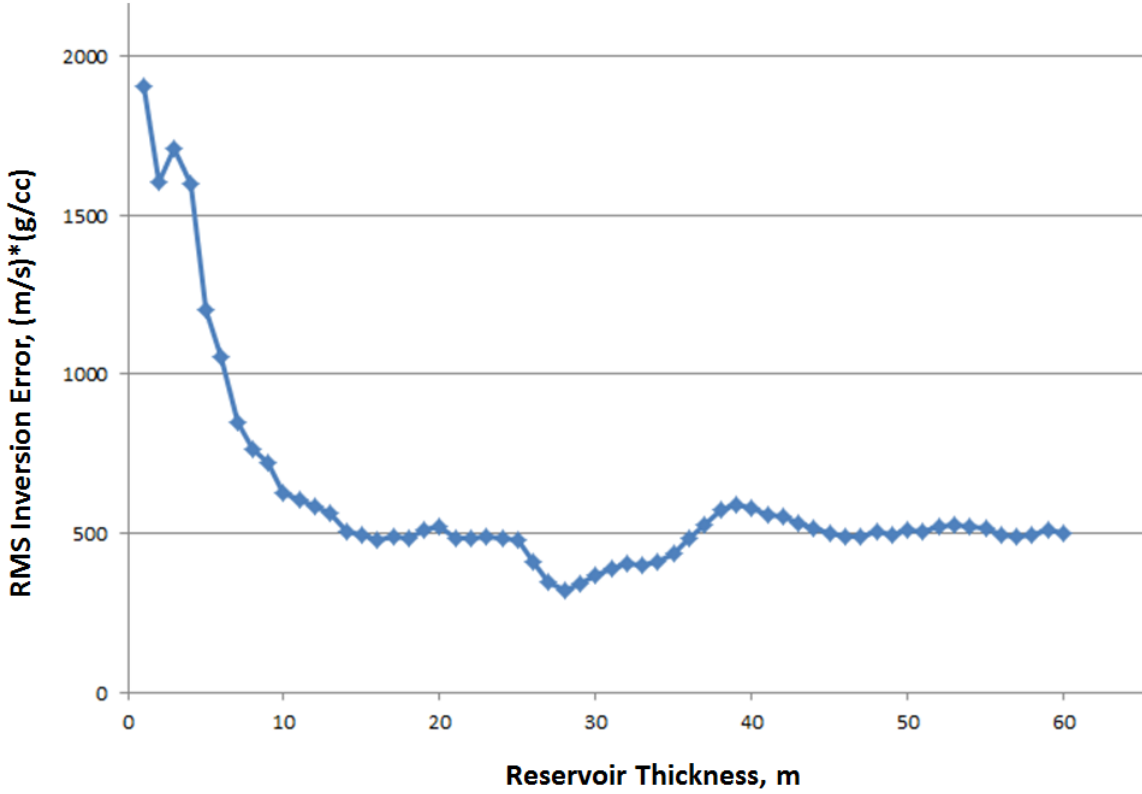
Figure 5.15. Crossplot of the RMS error of the simultaneous AVO inversion of the synthetic wedge model (shown in Figure 5.14) versus the wedge thickness. The RMS prediction errors were calculated within the Mississippian chert reservoir at each trace.
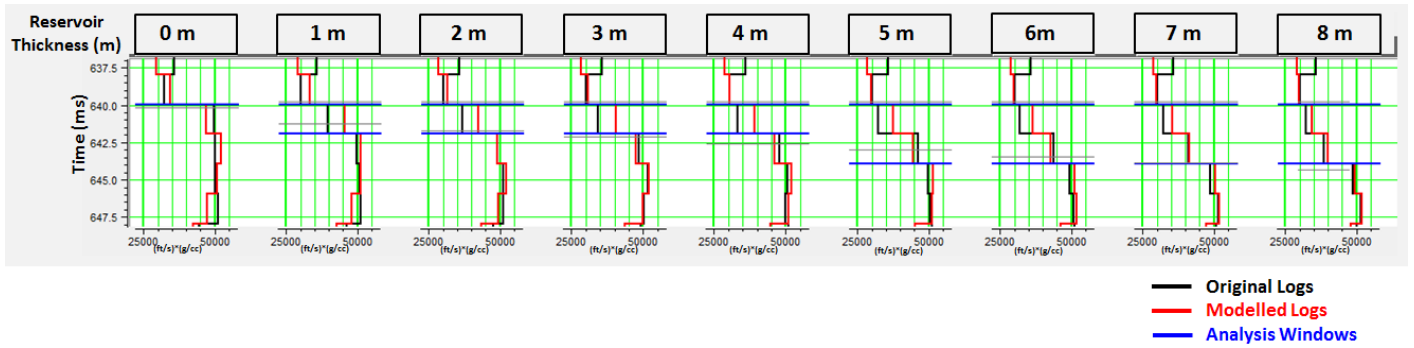
Figure 5.16. Analysis of inverted Z_P by simultaneous AVO inversion of the synthetic wedge model (shown in Figure 5.14) within the reservoir interval for the wedge thickness range 0-8 m. Red curves are inverted Z_P traces, and black curves are original P-impedance logs.
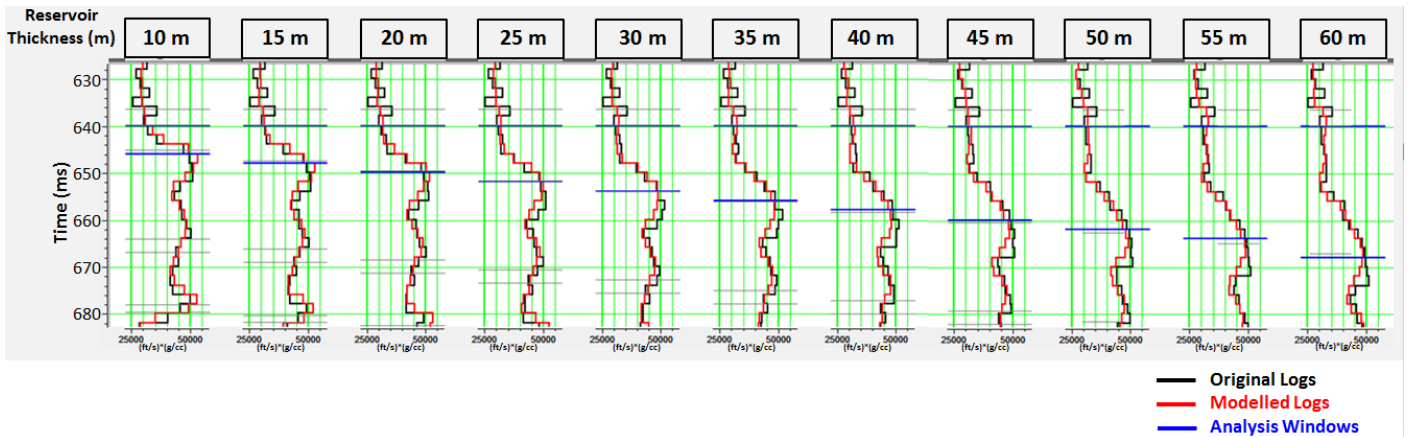
Figure 5.17. Analysis of inverted Z_P by simultaneous AVO inversion of the synthetic wedge model (shown in Figure 5.14) within the reservoir interval for the wedge thickness range 10-60 m with 5 m step. Red curves are inverted Z_P traces, and black curves are original P-impedance logs.

5.4: Simultaneous AVO Inversion Evaluation within the Arbuckle

The inverted Z_P, Z_S and density evaluation within the Arbuckle was done at wells #15-121-22590 and #15-121-22591 because the Arbuckle was penetrated by these two wells. Figure 5.18 shows the inverted Z_P traces (red) and the original P-impedance well logs (black) at wells #15-121-22590 and #15-121-22591. Generally, the inverted Z_P traces have the same trend of the original P-impedance logs. They have an acceptable overall correlation of 0.72 with the original P-impedance wells logs, and RMS inversion error of 813 (m/s)*(g/cc). However, there are some features that appear on the well logs that were not resolved by the inversion resulting in mismatches between inverted and original well logs especially at well #15-121-22590. This inversion resolution limit is due to the difference in frequency content between seismic data and well logs. Well logs usually have higher frequency bandwidth than seismic data. The Wellington Field seismic data has maximum useable frequency between 100 Hz and 128 Hz as shown in the amplitude spectrum of the seismic data in Figure 5.19. Therefore, the original well logs were low-pass filtered with a maximum frequency of 100 Hz and a maximum high cut of 128 Hz for inversion evaluation and porosity prediction evaluation within the Arbuckle in this research because seismic traces will never have better resolution than the filtered original well logs.

The inverted Z_P traces in Figure 5.20 show better agreement with the filtered P-impedance logs at both wells with higher overall correlation of 0.83 and lower RMS error of 568 (m/s)*(g/cc) (Figure 5.20). For comparing the simultaneous AVO inversion results with the post-stack model-based inversion results, the inverted P-impedance by model-based inversion of post-stack seismic data was evaluated within the Arbuckle at wells #15-121-22590 and #15-121-22591 (Figure 5.21). Visually, the post-stack model-based inverted P-impedance traces have the same trend of the original P-impedance logs. However, the post-stack model-based inverted

66

impedance traces showed a lower overall correlation of 0.66 with the original logs and a higher RMS inversion error of 820 (m/s)*(g/cc).

The simultaneous AVO inverted Z_S traces show a good agreement with the original S-impedance logs at both wells. The inverted Z_S traces have an overall correlation of 0.74 with the original S-impedance logs (Figure 5.22). A great advantage of the simultaneous AVO inversion for Z_P and Zs within the Arbuckle is that there is a good correlation between the inverted impedance traces at the different well locations, which makes it easy to match the corresponding tops of Arbuckle flow units between the different well locations on the inverted data. Figure 5.23 shows the inverted Z_P traces at well #15-121-22590 and well #15-121-22591. Both traces show the same trend that made it easy to relate the corresponding tops of the flow units at the two well locations. This advantage has shown an effect when interpreting the impedance volumes. For example, there is a low impedance zone between the tops of flow units FU11 and FU12 at both wells (Figure 5.23). The simultaneous AVO inverted Z_P cross section of Line A in Figure 5.24a shows, in the white box between the wells, that this low impedance zone is continuous between the two wells. However, the same low impedance zone in the post-stack model-based inversion in Figure 5.24b does not seem continuous between the two wells. Actually, the low impedance zone between the tops of flow units FU11 and FU12 at well #15-121-22591 to the left might be mistaken for being related to the shallower low impedance zone between the tops of flow units FU8 and FU10 at well #15-121-22590 to the right (Figure 5.24b).

By looking at the two P-impedance cross sections in Figures 5.24a, b, the low impedance zones are better defined in the simultaneous AVO inverted Z_P cross section compared to the post-stack model-based inversion cross section. The low impedance zones in the simultaneous AVO inverted impedance cross section show better contrast with the surrounding higher

impedance zones, which makes it easy to identify and follow the low impedance zones around the field. The low impedance zones were picked by the dashed lines on the simultaneous AVO inverted Z_P cross section in Figure 5.24a because it has better depiction of the subsurface features, and the same dashed lines are overlain on the post-stack model-based inverted impedance cross section in Figure 5.24b. The injection zone chosen for the CO_2 sequestration is the bottom picked low impedance zone near the top of flow unit FU15 (Figure 5.24a). The inverted Z_S cross section of Line A in Figure 5.25 exhibits the same impedance trends shown by the Z_P cross section.

Finally, inverted and original densities show a good visual agreement between their trends in the Arbuckle at wells #15-121-22590 and #15-121-22591 with an overall correlation of 0.64 that is acceptable, but lower than the correlation of inverted Z_P and inverted Z_S with the original logs (Figure 5.26). An inverted density cross section along Line A is shown in Figure 5.27. Inverted density trends are in overall agreement with inverted Z_P and inverted Z_S shown in Figure 5.24a and Figure 5.25.

Figure 5.18. Analysis of inverted Z_P by simultaneous AVO inversion within the Arbuckle Group at wells #15-121-22590 and #15-121-22591. Red curves are inverted Z_P traces and black curves original P-impedance logs. Overall correlation between inverted and original logs is 0.72 for all wells. The total RMS error for all wells is 813 (m/s)*(g/cc).
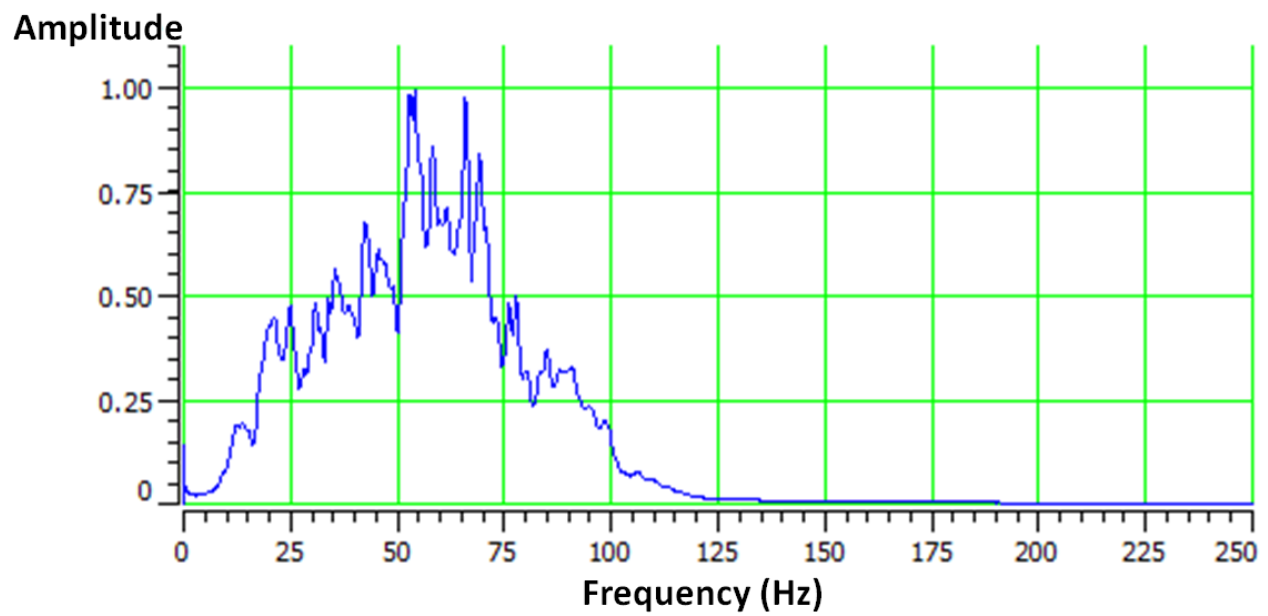
Figure 5.19. Amplitude spectrum of the Wellington Field seismic gathers. The data has frequency content ranging between 10 Hz and 128 Hz.
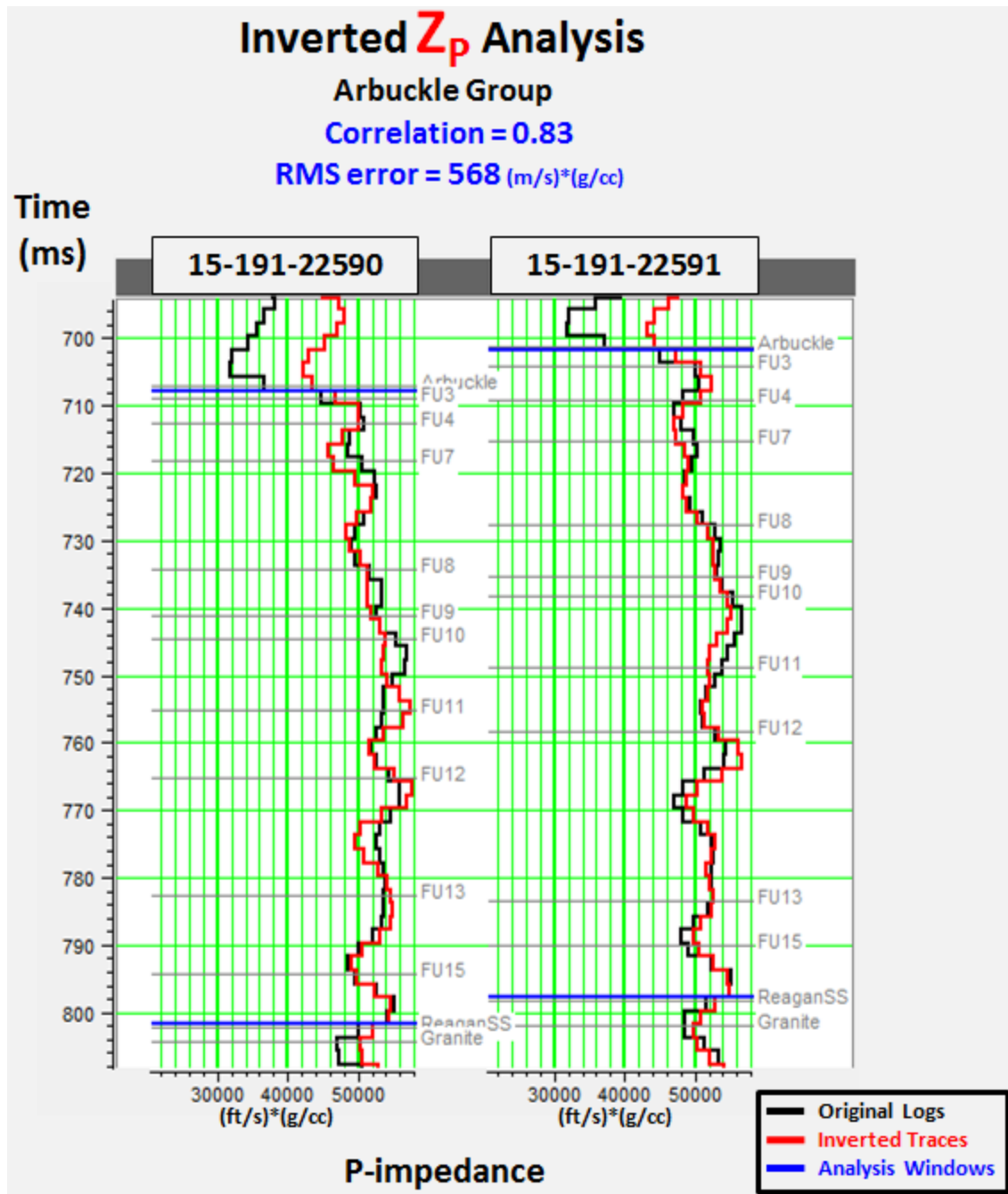
Figure 5.20. Analysis of inverted Z_P by simultaneous AVO inversion within the Arbuckle Group at wells #15-121-22590 and #15-121-22591. Red curves are inverted Z_P traces, and black curves are filtered original P-impedance logs. Overall correlation between inverted and original logs is 0.83 for all wells. The total RMS error for all wells is 568 (m/s)*(g/cc).

Figure 5.21. Analysis of inverted P-impedance by post-stack model-based inversion within the Arbuckle Group at wells #15-121-22590 and #15-121-22591. Red curves are inverted P-impedance traces, and black curves are filtered original P-impedance logs. Overall correlation between inverted and original logs is 0.66 for all wells. The total RMS error for all wells is 820 (m/s)*(g/cc).
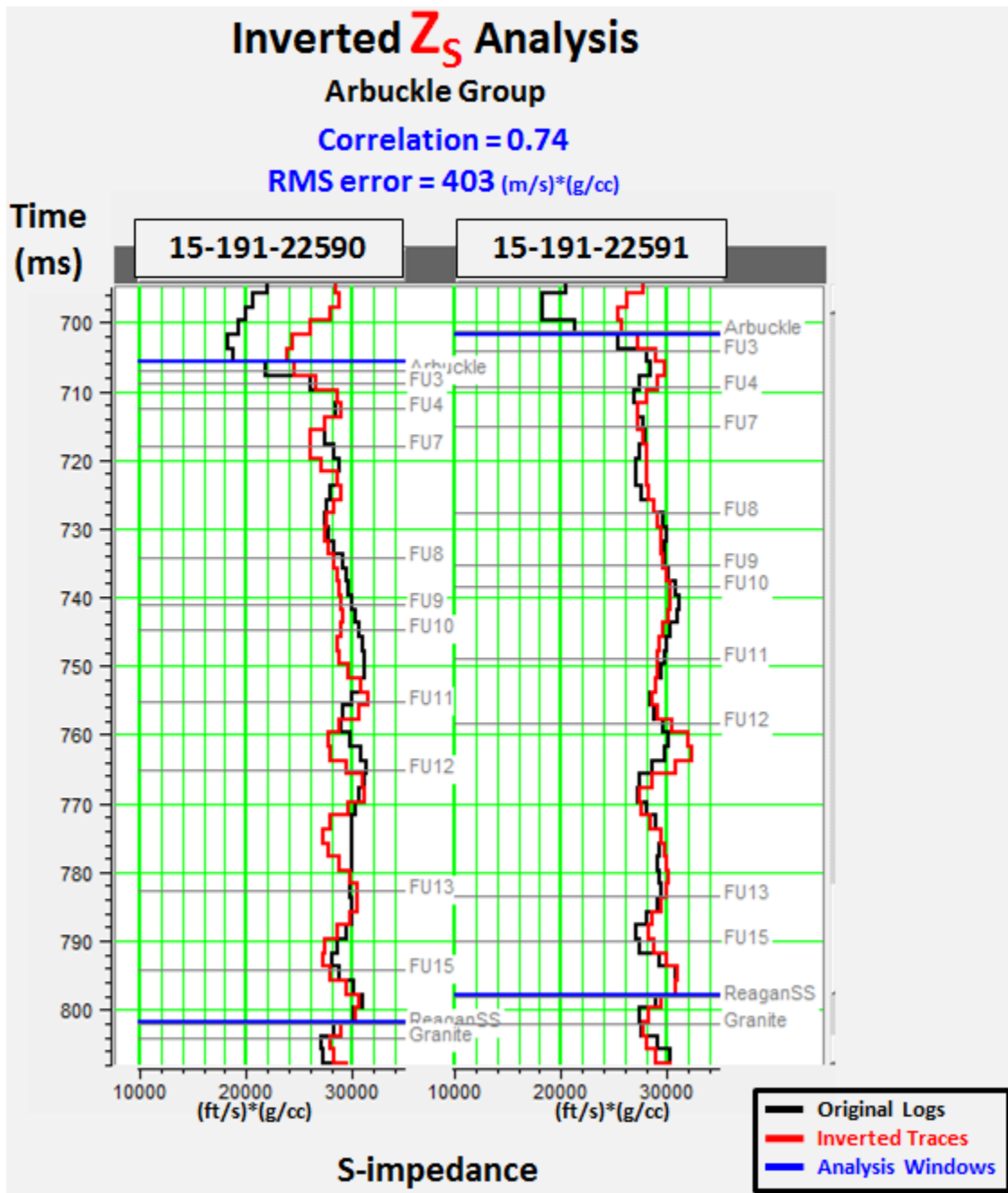
Figure 5.22. Analysis of inverted Z_S by simultaneous AVO inversion within the Arbuckle Group at wells #15-121-22590 and #15-121-22591. Red curves are inverted Z_S traces, and black curves are filtered original S-impedance logs. Overall correlation between inverted and original logs is 0.74 for all wells. The total RMS error for all wells is 403 (m/s)*(g/cc).
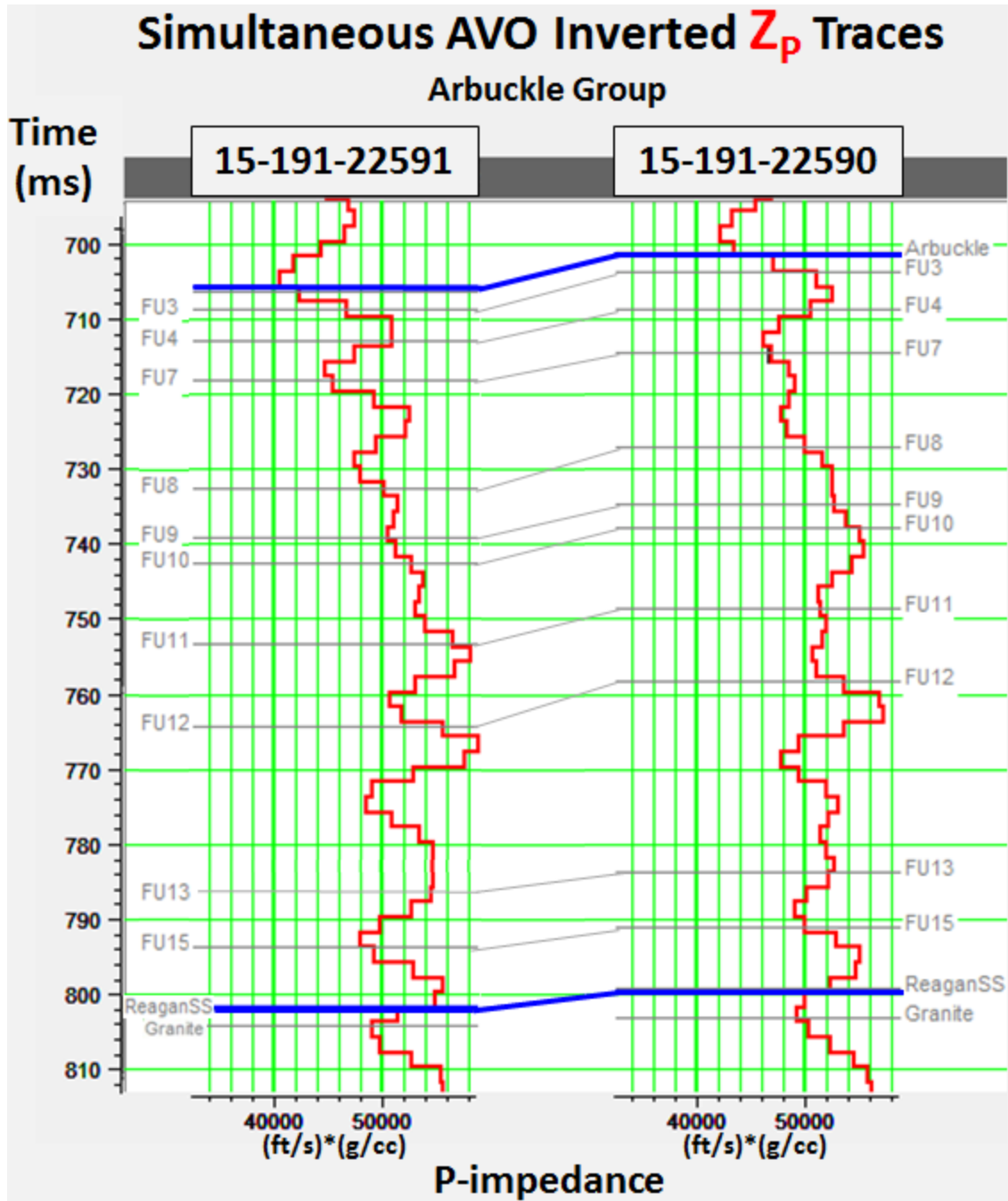
Figure 5.23. Simultaneous AVO inverted Z_P traces at well #15-121-22590 and well #15-121-22591. Both traces show the same trend that made it easy to relate the corresponding tops of the flow units at the two well locations.
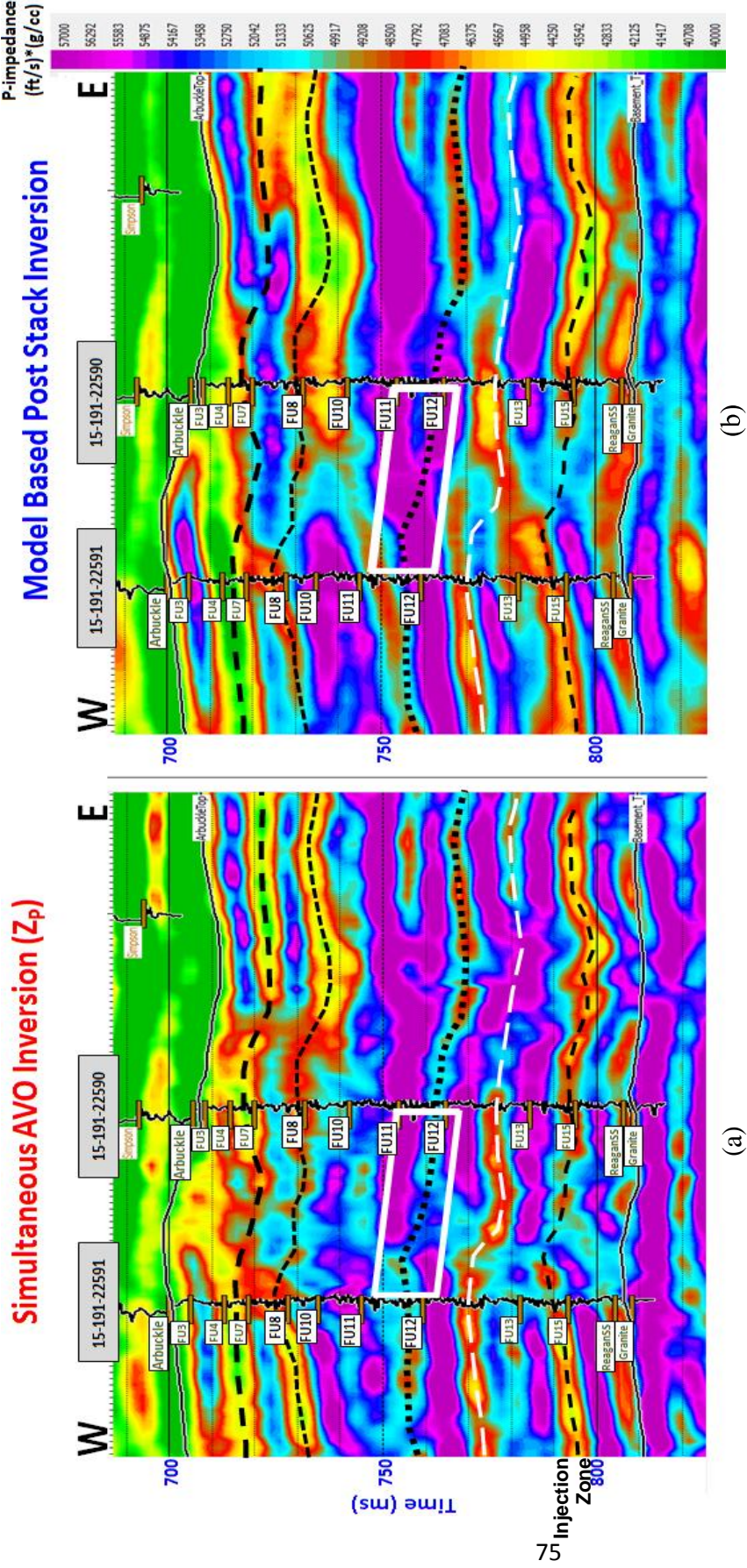
Figure 5.24. a) Simultaneous AVO inverted Z_P cross section. b) Post-stack model-based inverted P-impedance cross section. Cross sections location is Line A shown in Figure 3.3. The low impedance zones are picked by the dashed lines on the simultaneous AVO inverted Z_P cross section because it has better depiction of the subsurface features, and the same dashed lines are overlain on the post-stack model-based inverted P-impedance cross section.
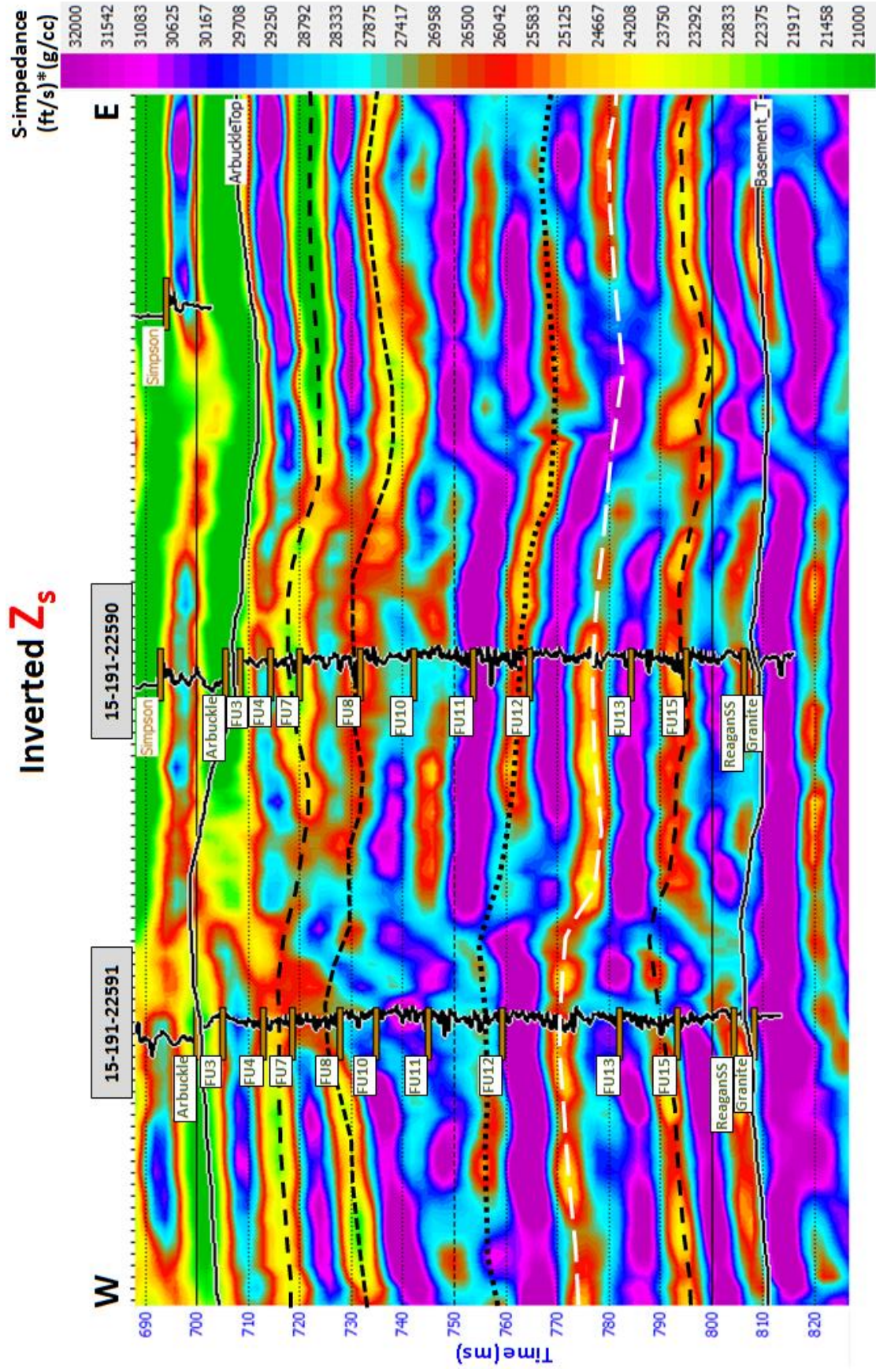
Figure 5.25: Simultaneous AVO inverted Z_S cross section with S-impedance well logs posted at well locations. Cross section location is Line A shown in Figure 3.3.
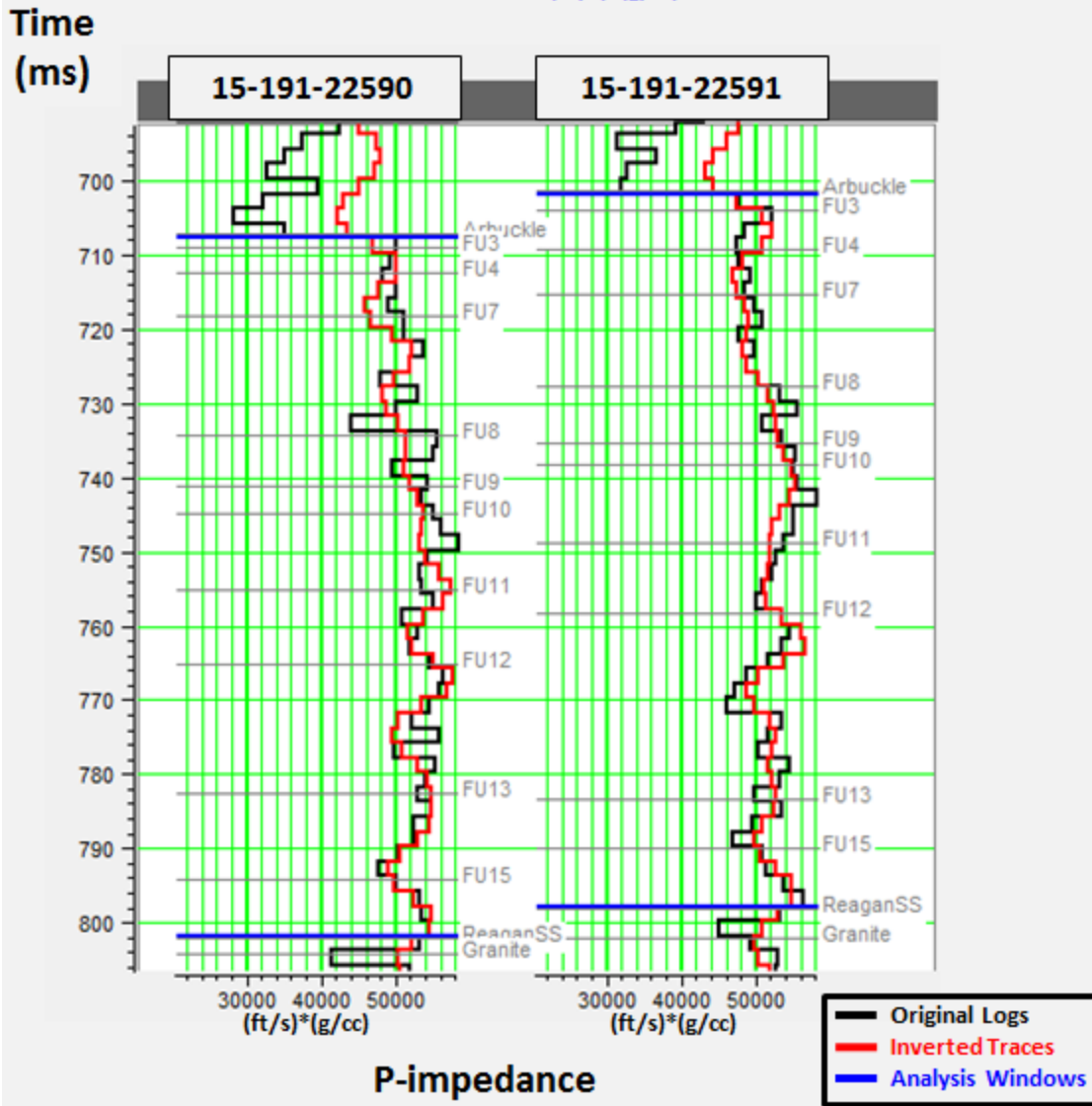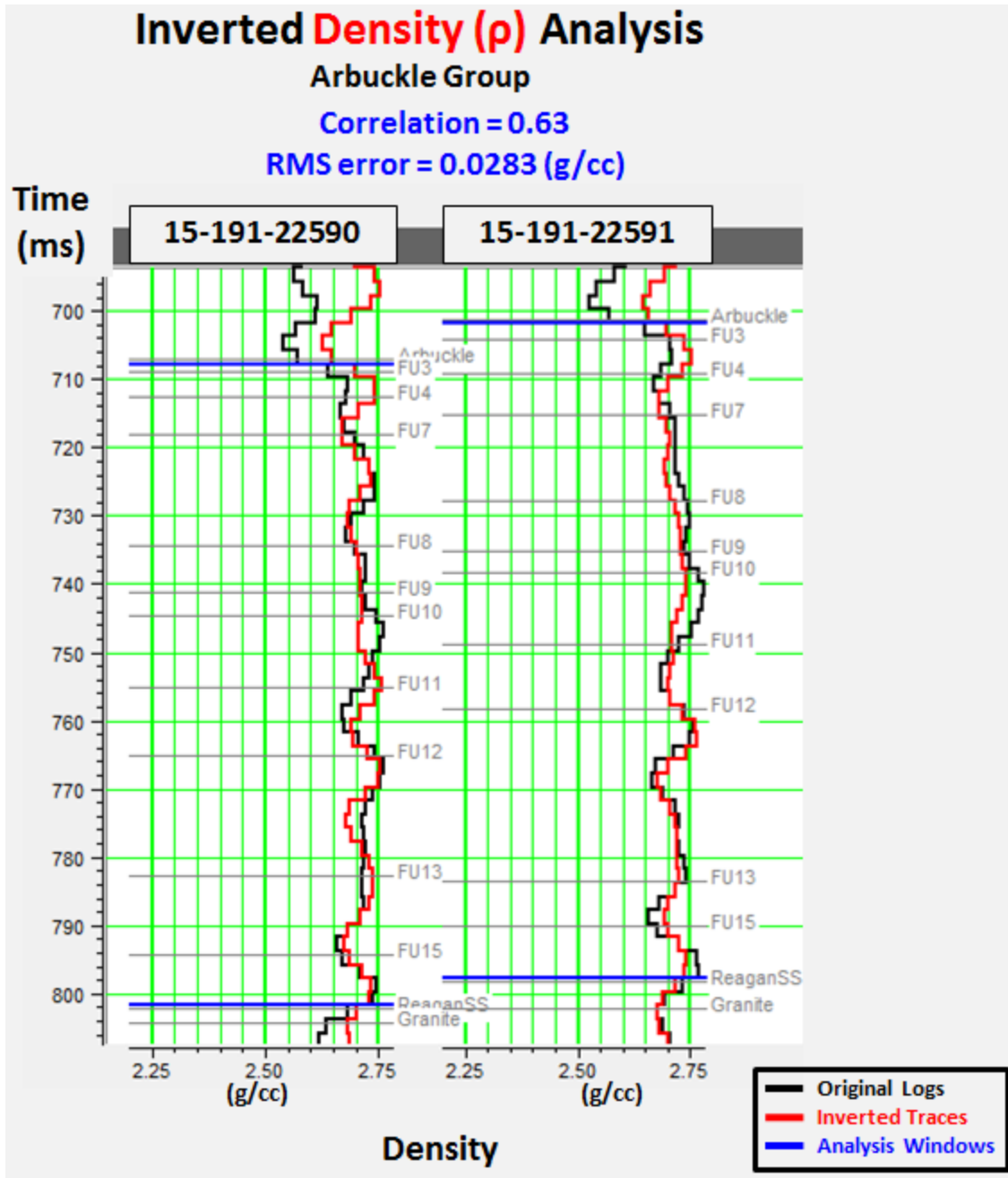
Figure 5.26. Analysis of inverted density by simultaneous AVO inversion within the Arbuckle Group at wells #15-121-22590 and #15-121-22591. Red curves are inverted density traces, and black curves are filtered original density logs. Overall correlation between inverted and original logs is 0.63 for all wells. The total RMS error for all wells is 0.0283 (g/cc).
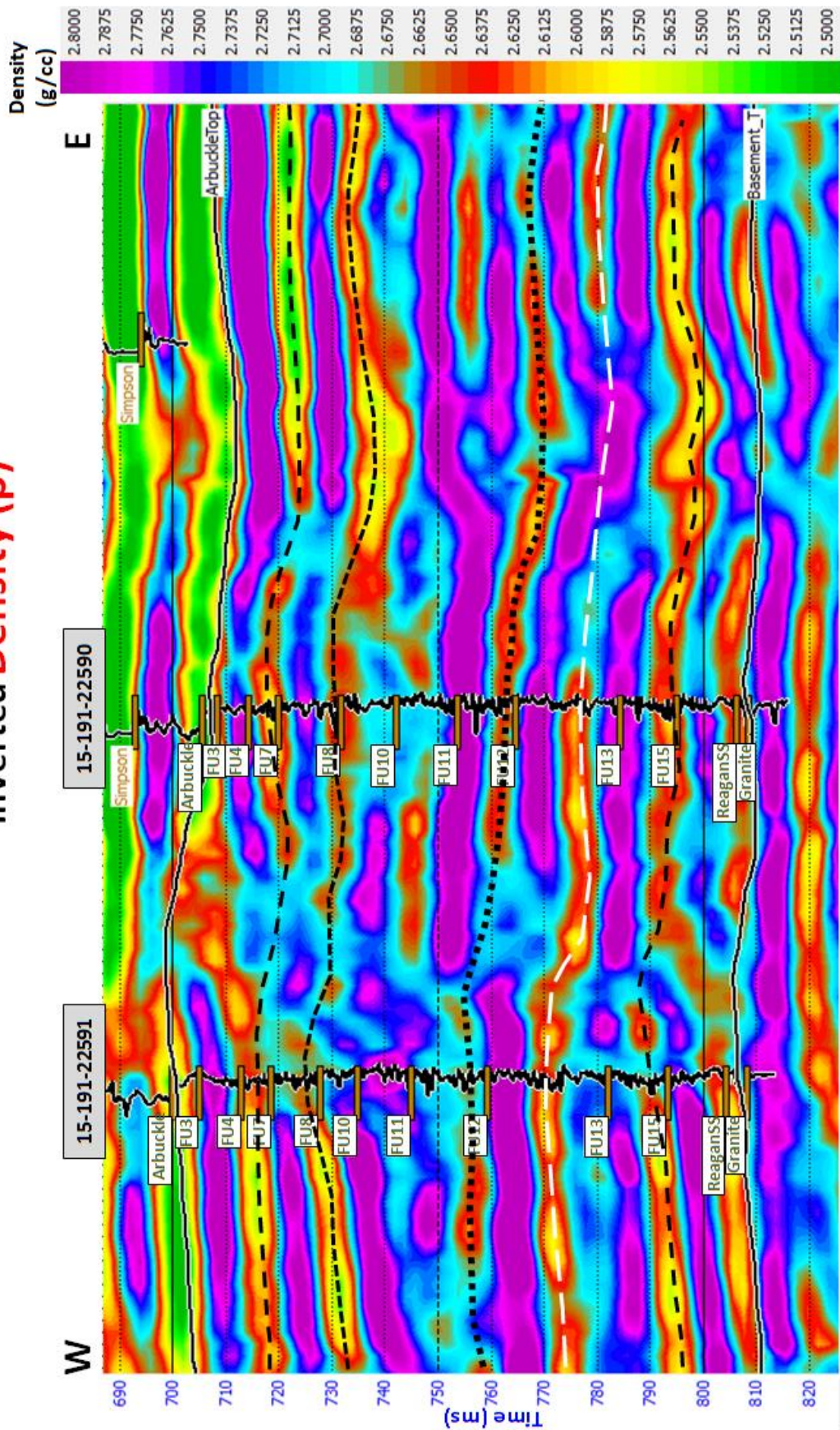
Figure 5.27. Simultaneous AVO inverted density cross section. Cross section location is Line A shown in Figure 3.3.

CHAPTER 6: POROSITY PREDICTION

Three sets of data were used for porosity prediction. The data used were the simultaneous AVO inverted Z_P and Z_S volumes, the post-stack seismic data and formation porosity logs of the eleven wells that are tied to the seismic data. The software used for porosity prediction was the Hampson-Russell EMERGE software that finds the relationship between the formation porosity logs and the seismic attributes at the well locations by multi-attribute linear regression analysis described by Hampson et al. (2001). The software uses this relationship to estimate the porosity at all locations of the seismic volume.

6.1: Multi-attribute Linear Regression Analysis

For porosity prediction, EMERGE software applies multilinear regression analysis to find a relationship between the formation porosity logs and a combination of attributes. EMERGE differentiates between two types of attributes. The internal attributes listed in Table 6.1 are the group of attributes calculated automatically by EMERGE from the post-stack seismic data. The external attributes are the attributes determined by the user which, for this study, were the inverted Z_P and Z_S by simultaneous AVO inversion. The best combination of attributes for porosity prediction is determined by the step-wise regression method which identifies these attributes in steps by trial and error. In the first step, the linear relationship between the formation porosity logs and each attribute is defined by solving the equation for a **single-attribute transform**:

$$\phi(t) = w_0 + w_1 . A_1(t) \qquad (5)$$

where $\phi(t)$ – formation porosity values known from well logs,

$A_1(t)$ – a seismic attribute value,

w_0 and w_1 – unknown weights.

Instantaneous attributes:	Amplitude envelope
	Amplitude weighted cosine phase
	Amplitude weighted frequency
	Amplitude weighted phase
	Apparent polarity
	Cosine instantaneous phase
	Instantaneous frequency
	Instantaneous phase
Windowed frequency attributes	Average frequency
	Dominant frequency
Filter slice attributes	Filter 5/10 – 15/20 Hz
	Filter 15/20 – 25/30 Hz
	Filter 25/30 – 35/40 Hz
	Filter 35/40 – 45/50 Hz
	Filter 45/50 – 55/60 Hz
	Filter 55/60 – 65/70 Hz
Derivative attributes	Derivative
	Derivative instantaneous amplitude
	Second derivative
	Second derivative instantaneous amplitude
Integrate attributes	Integrate
	Integrate absolute amplitude

Table 6.1. Internal seismic attributes used in the multi-attribute linear regression analysis.

The weights w_0 and w_1 are calculated by the least-squares minimization approach for each attribute (Hampson et al., 2001). Then, the best attribute that results in the lowest RMS error is chosen to be $A^1_1(t)$. In the second step, another attribute is determined by solving the equation for

two-attribute transform in which the known first best attribute $A^1_1(t)$ is paired with another attribute:

$$\phi(t)=w_0+w_1.A^1_1(t)+w_2.A_2(t) \qquad (6)$$

where $\phi(t)$ – formation porosity values known from well logs,

$A^1_1(t)$ – the best single attribute,

$A_2(t)$ – seismic attribute value,

w_0, w_1 and w_2 – unknown weights.

The attribute that results in the lowest RMS values is chosen to be the second attribute $A^2_2(t)$. This process can go on as long as desired to find N seismic attributes to derive a **multi-attribute transform**:

$$\phi(t)=w_0+w_1{\cdot}A^1_1(t) +...+ w_N{\cdot}A^N_N(t) \qquad (7)$$

The higher the number of attributes in the multi-attribute transform the lower the prediction error. However, using a large number of attributes in the transform could result in overfitting the data at the well locations, but the porosity prediction interpolation between the wells would be erroneous (Kalkomey, 1997). Therefore, the validation error is calculated by leaving out wells. When a multi-attribute transform is derived, its validity for porosity prediction is tested by solving for the regression coefficients using porosities from all wells except one well, which is called the blind well. Then, by using the derived coefficients, the prediction error is calculated at the location of the blind well. This process is repeated for all wells to calculate an average validation error (Hampson et al., 2001).

So far, the method is limited because it only correlates each target sample with the corresponding samples on the seismic attribute ignoring the big difference in the frequency content between the well logs and seismic data. Therefore, the crossplot regression was extended

to include neighboring samples by convolutional operators that allow predicting each target sample by a weighted average of samples on each attribute. The number of averaged samples on each attribute is the length of the convolutional operator. The weights on the individual samples are determined by the shape of the convolutional operator (Hampson et al., 2001). Therefore, when using convolutional operators, the multi-attribute transform in equation (7) is replaced by:

$$\phi(t)=w_0+w_1*A^1_1(t) +...+ w_N *A^N_N(t) \qquad (8)$$

(*) Represents convolution by an operator

6.2: Mississippian Reservoir Porosity Prediction

Two multi-attribute transforms were derived in this study. The first multi-attribute transform was derived within the Mississippian reservoir only. Therefore, the porosity prediction volume will not be valid outside the Mississippian reservoir using this transform. A group of attributes and different convolutional operator lengths was tested for optimum porosity prediction. During the process of deriving the transform by step-wise regression, the validation error is measured every time an additional attribute is added to the transform in order to make a cross-validation curve that shows the maximum number of attributes with the lowest validation error. Also, using convolutional operators means adding more attributes that decrease the prediction error but not necessarily the validation error. Therefore, cross-validation is applied for convolutional operators as well (Hampson et al., 2001). Figure 6.1 shows the porosity prediction validation error curves created by crossplotting the number of attributes in the transform against the validation error. Each curve represents a different convolutional operator length. According to the validation error plot in Figure 6.1, the light blue curve shows that the lowest validation error is achieved when the five attributes listed in Table 6.2 are used with 5-point-convolutional operator for porosity prediction within the Mississippian reservoir.

82

The resulting porosity prediction was evaluated within the Mississippian reservoir. Figure 6.2 shows porosity prediction traces (red) and original porosity logs (black) at well locations. The Mississippian reservoir is marked by the blue markers at the different wells. Figure 6.2 shows good agreement between predicted and original porosity logs within the Mississippian reservoir with an overall cross correlation of 0.90. The crossplotting of predicted and original porosity logs shows a linear relationship that supports the good agreement (Figure 6.3). Figure 6.4 is a cross section of the predicted porosity of Line A with well porosity logs overlain on the section. The derived transform was the best transform for quantitative porosity values prediction within the Mississippian reservoir, but it does not provide meaningful results outside the Mississippian reservoir.

However, the second multi-attribute transform, which was derived within a larger window that includes the surrounding background formations resulted in an acceptable valid porosity prediction within the Mississippian reservoir and around it. The second multi-attribute transform was derived between the Cherokee Group top above the Mississippian and the Reagan Sandstone top at the base of the Arbuckle. Therefore, the resulting porosity prediction volume by the second transform helps identify porosity differences between the Mississippian reservoir and the surrounding formations, and it helps determine the top and the base of the Mississippian reservoir that can be easily delineated across the Wellington field (Figure 6.5). The derivation of the second multi-attribute transform will be discussed in more details in section 6.3. The porosity prediction results were compared with the results of the A-B crossplotting technique described in section 4.1 (Figure 6.6). The same Class IV AVO highlighted zone shows higher porosity values in the porosity prediction cross section as shown in Figure 6.6.

Number of attributes	Seismic Attribute	Prediction Error porosity fraction	Validation error porosity fraction
1	Instantaneous Phase	0.039852	0.045785
2	1/(Z_S)	0.031128	0.044479
3	Apparent Polarity (Z_P)	0.025288	0.040763
4	Amplitude Weighted Frequency (Z_P)	0.021179	0.034428
5	Second Derivative	0.018626	0.032762

Table 6.2: Attributes of the first multi-attribute transform derived within the Mississippian chert reservoir for porosity prediction. Note that the prediction error decreases with increasing number of attributes. Validation error was used to determine the optimum number of seismic attributes.
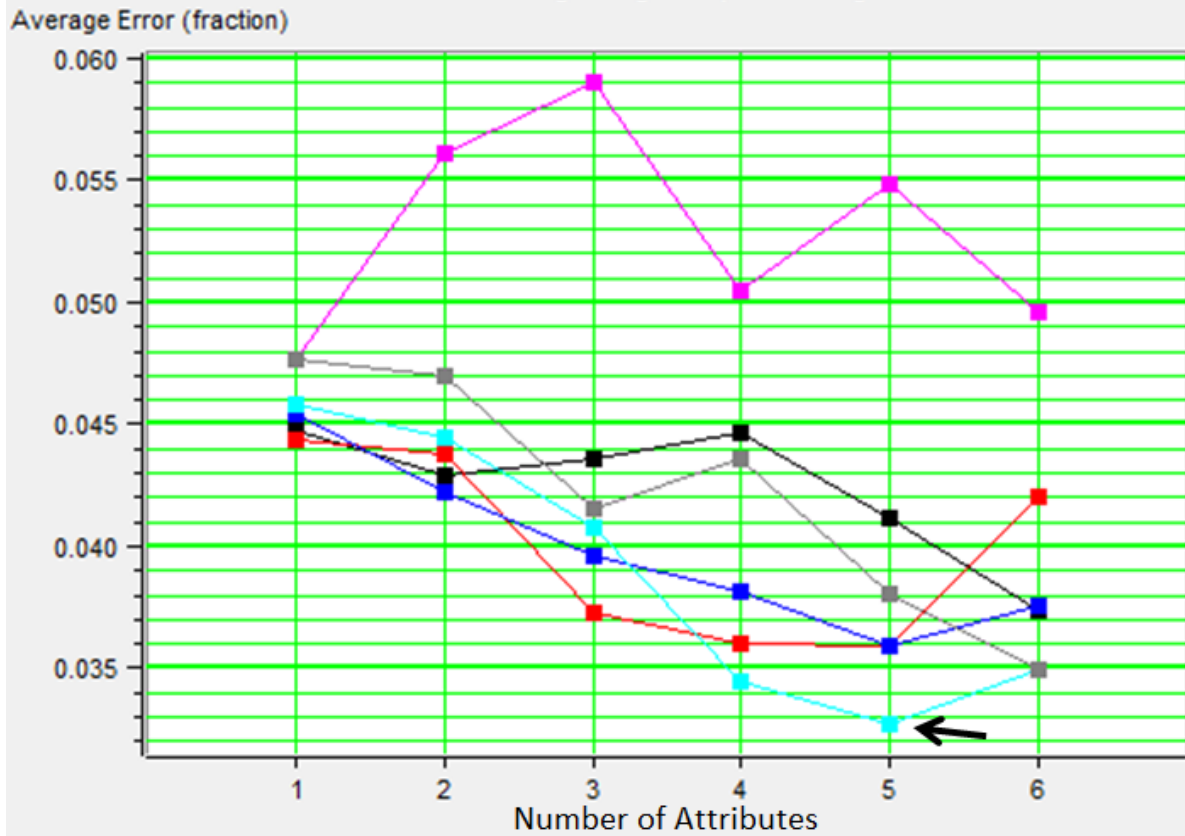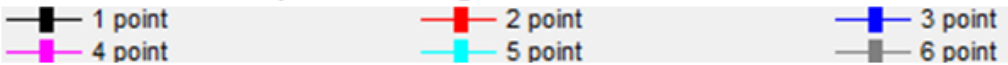
Figure 6.1. Average RMS validation error versus the number of seismic attributes used for deriving multi-attribute transforms within the Mississippian chert reservoir only. Each curve represents the convolutional operator length. The lowest RMS validation error is achieved when the five attributes listed in Table 6.2 are used with 5-point-convolutional operator.
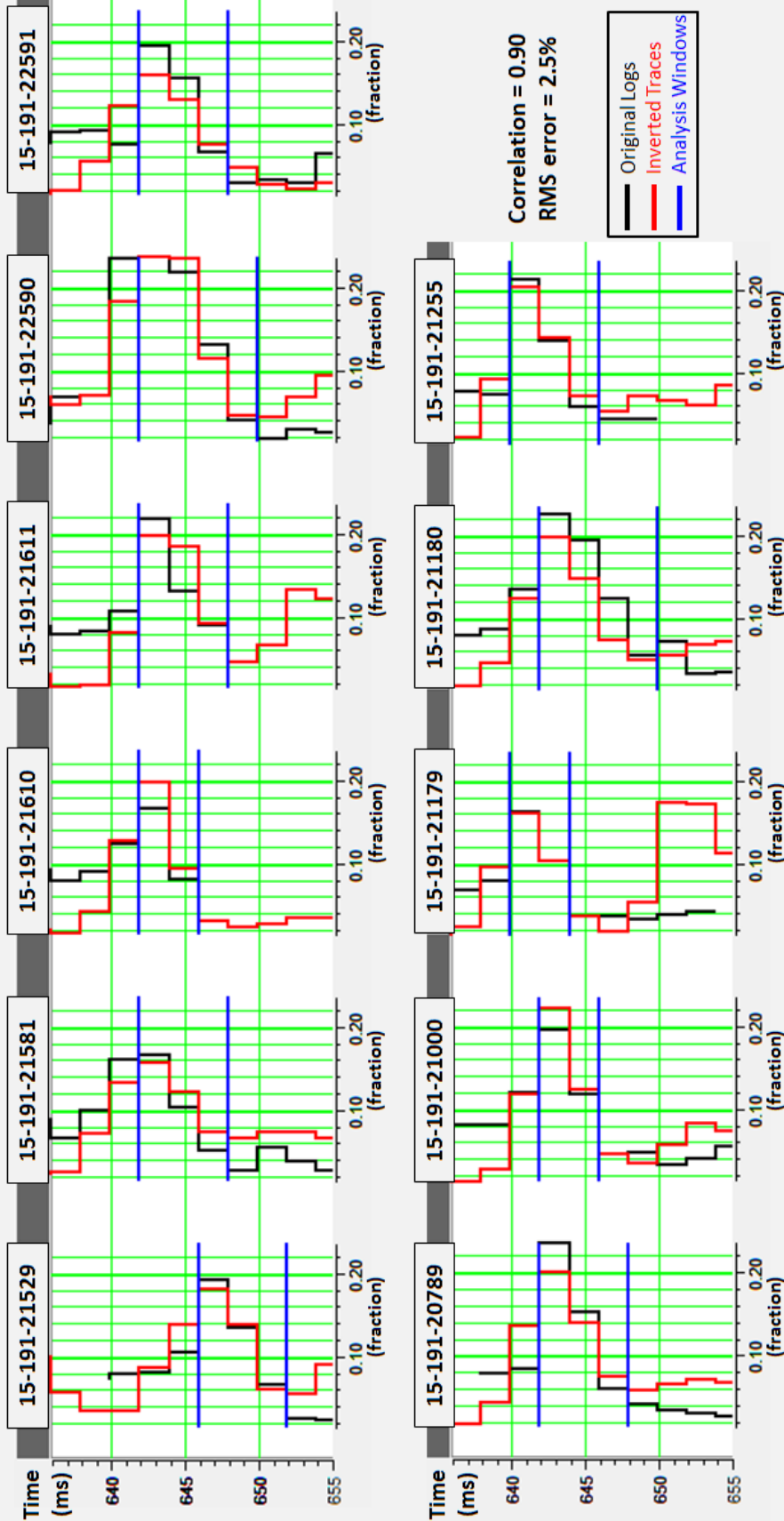
Figure 6.2. Analysis of the predicted porosity by the first multi-attribute transform within the Mississippian reservoir (shown by the blue horizontal lines of the analysis window) at 11 well locations. The predicted porosity traces (red) show a good agreement with the original formation porosity logs (black) with an overall correlation of 0.90 for all wells. The total RMS error for all wells is 2.5%.
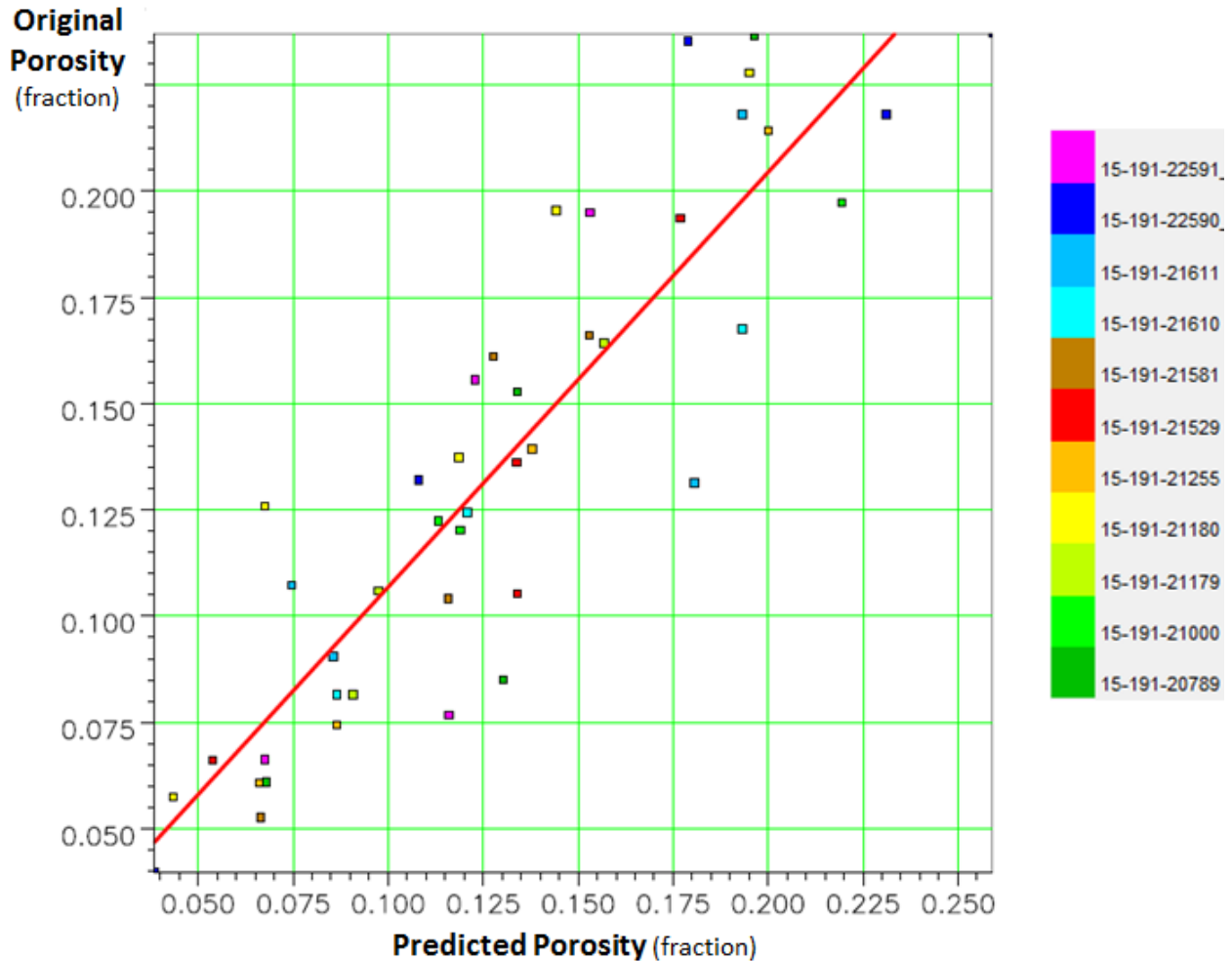
Figure 6.3. Crossplot of the predicted porosity by the first multi-attribute transform versus the original formation porosity logs within the Mississippian chert reservoir (the analysis window shown with blue horizontal lines in Figure 6.2) at 11 well locations. The red line shows the line of perfect correlation between predicted and original porosity values. The total RMS error for the 11 wells is 2.5%.
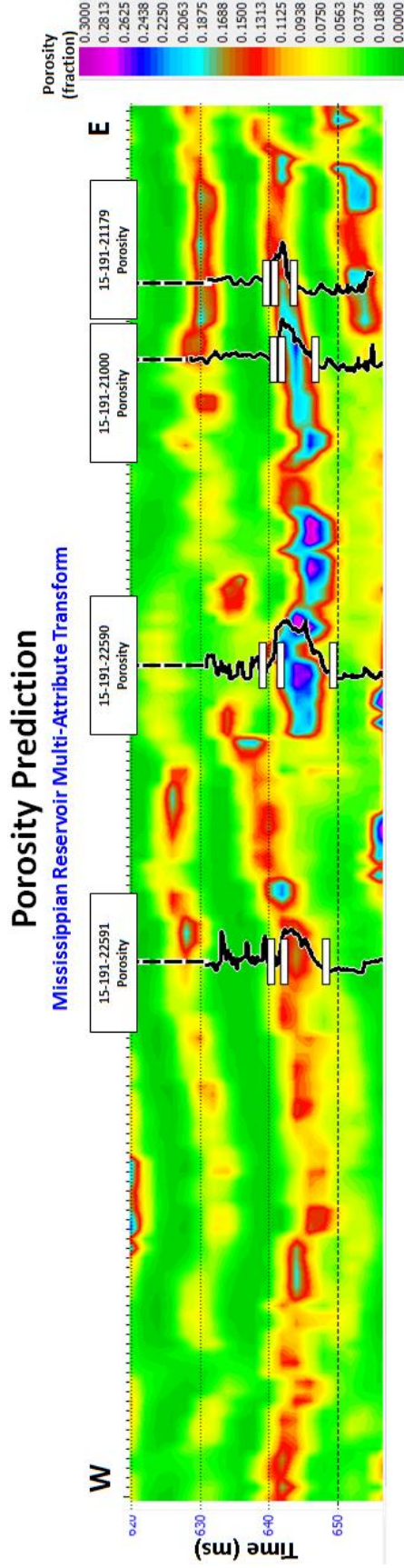
Figure 6.4. Cross section of predicted porosity by the first multi-attribute transform with formation porosity logs posted at well locations. The first multi-attribute transform derived with the Mississippian chert reservoir is the best transform for quantitative porosity values prediction within the Mississippian reservoir, but it does not provide meaningful results outside the Mississippian chert reservoir. Cross section location is Line A shown in Figure 3.3.
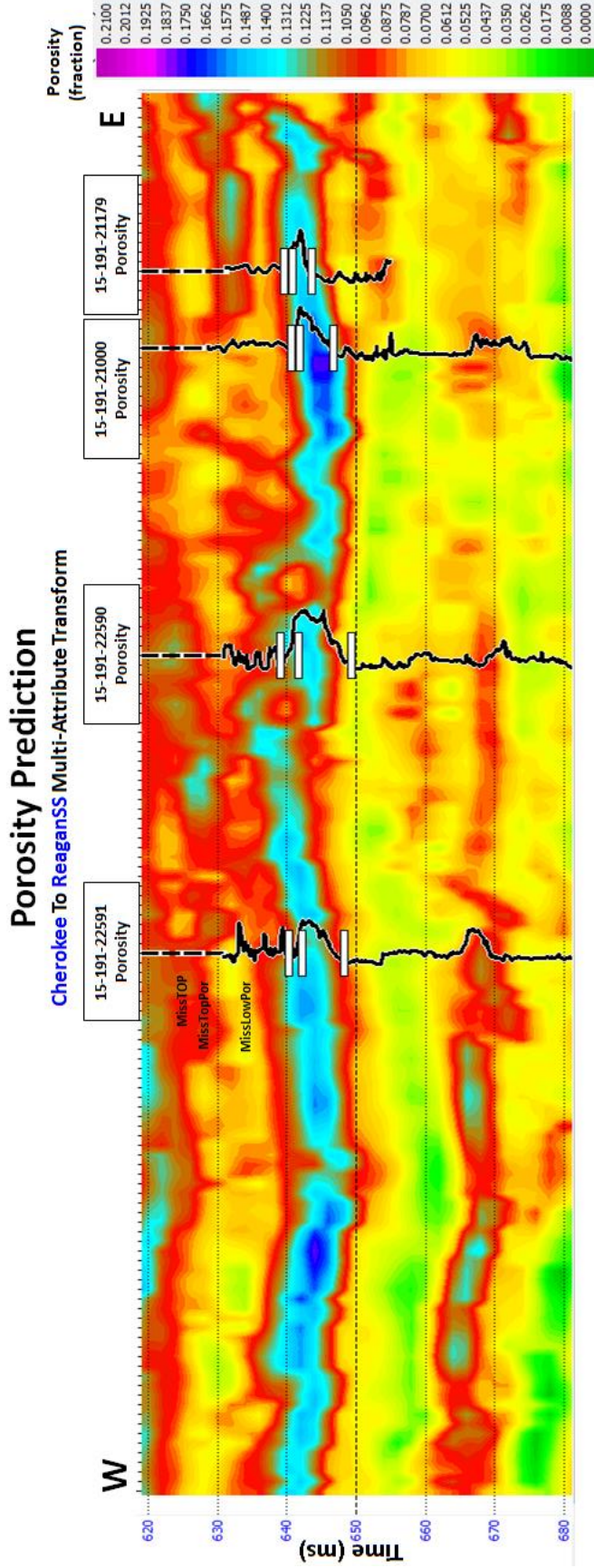
Figure 6.5. Cross section of predicted porosity by the second multi-attribute transform with formation porosity logs posted at well locations. The second multi-attribute transform derived between the Cherokee formation top and the Reagan Sandstone top provides valid results outside the Mississippian chert reservoir. Cross section location is Line A shown in Figure 3.3.
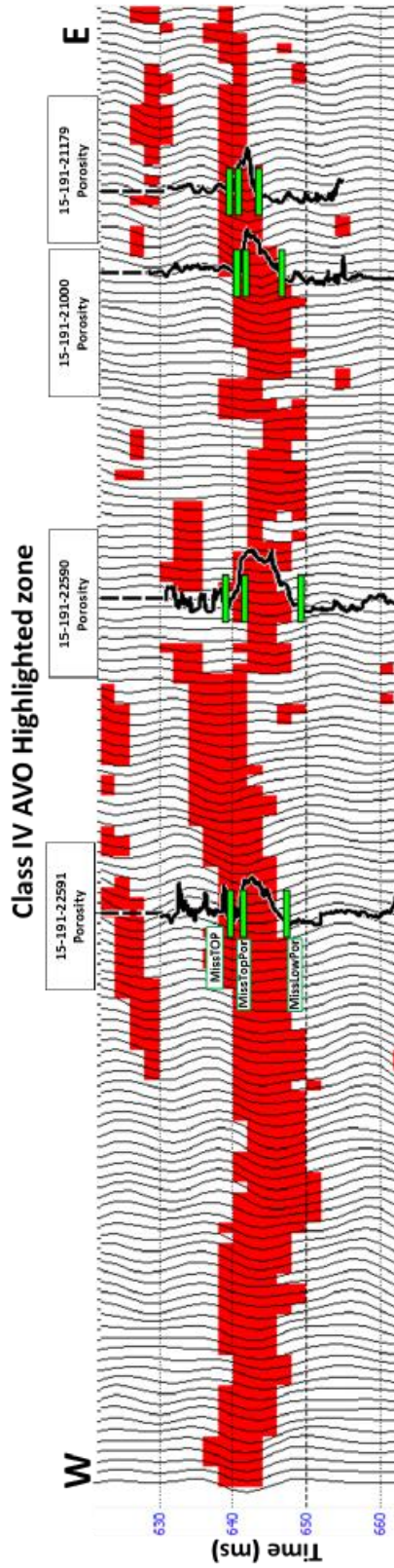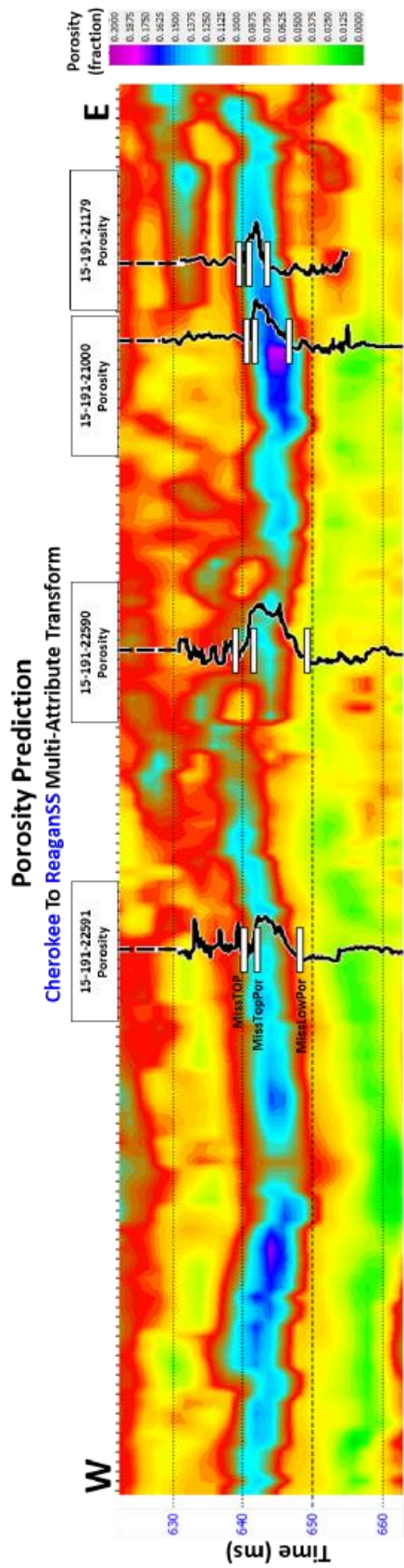
Figure 6.6. (Top) Cross section of predicted porosity by the second multi-attribute transform with formation porosity logs. (Bottom) Cross section of Class IV AVO highlighted zone by the A-B crossploting technique with formation porosity logs. The same Class IV AVO highlighted zone shows high porosity values in the porosity prediction cross section. Cross section location is Line A shown in Figure 3.3.

90

6.3: Arbuckle Group Porosity Prediction

When the multi-attribute transform was derived within the Arbuckle Group only, it resulted in a porosity prediction volume that has high correlation with formation porosity logs at wells #15-121-22590 and #15-121-2259, but the resulting volume did not provide reasonable porosity values away from the two wells. This might be due to limited well control within the Arbuckle. Unlike the Mississippian reservoir, the optimum porosity prediction quality within the Arbuckle was achieved when the multi-attribute transform was derived between the Cherokee Group top and the Reagan Sandstone top using the eleven wells that have formation porosity logs including the wells that did not penetrate the Arbuckle Group.

According to the validation error plot in Figure 6.7, the light blue curve shows that the lowest validation error is achieved when the seven attributes listed in Table 6.3 are used with 5-point convolutional operator for porosity prediction between the Cherokee Group top and the Reagan Sandstone top.

The resulting porosity prediction volume was analyzed within the Arbuckle Group. Figure 6.8 shows the porosity prediction traces (red) and the original formation porosity logs (black) at wells #15-121-22590 and #15-121-2259. The blue markers represent the analysis window between the Arbuckle top and the Reagan Sandstone. The overall correlation of the predicted porosity traces with the original formation porosity logs is 0.67.

The results of the porosity prediction in the Arbuckle show good agreement with the results of the A-B crossplotting technique (Figures 6.9-6.10). In Figures 6.9-6.10, the highlighted Class IV AVO zones show higher porosity values than the zones that were not highlighted on the corresponding porosity prediction sections.

Number of attributes	Seismic Attribute	Prediction Error porosity fraction	Validation error porosity fraction
1	$1/(Z_S)$	0.031697	0.033091
2	$1/(Z_P)$	0.029556	0.032147
3	Filter 35/40-45/50	0.028154	0.030998
4	Instantaneous Phase	0.026858	0.030423
5	Second Derivative	0.026060	0.029963
6	Filter 35/40-45/50 (Z_P)	0.025368	0.029856
7	Average Frequency	0.024891	0.029135

Table 6.3: Attributes of the second multi-attribute transform derived between the Cherokee Group top and the Reagan Sandstone top for porosity prediction. Note that the prediction error decreases with increasing number of attributes. Validation error was used to determine the optimum number of seismic attributes.
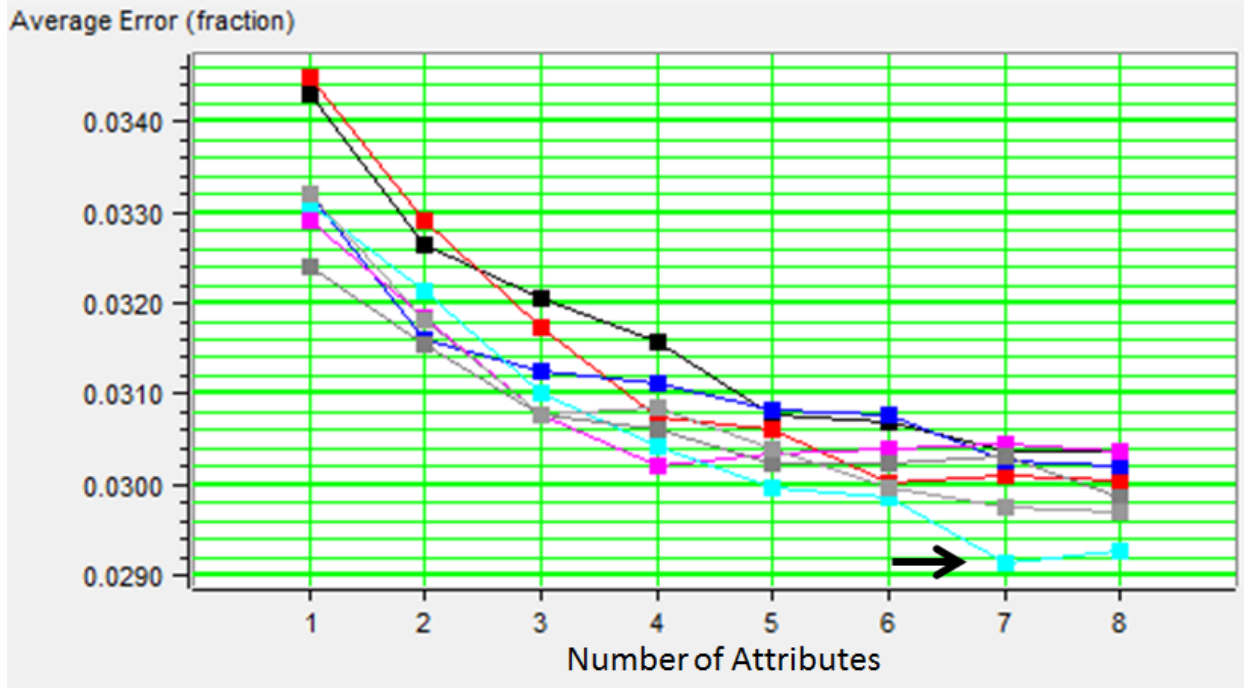
Figure 6.7: Average RMS validation error versus the number of seismic attributes used for deriving multi-attribute transforms between the Cherokee Group top and the Reagan Sandstone top. Each curve represents the convolutional operator length. The lowest RMS validation error is achieved when the seven attributes listed in Table 6.3 are used with 5-point-convolutional operator.
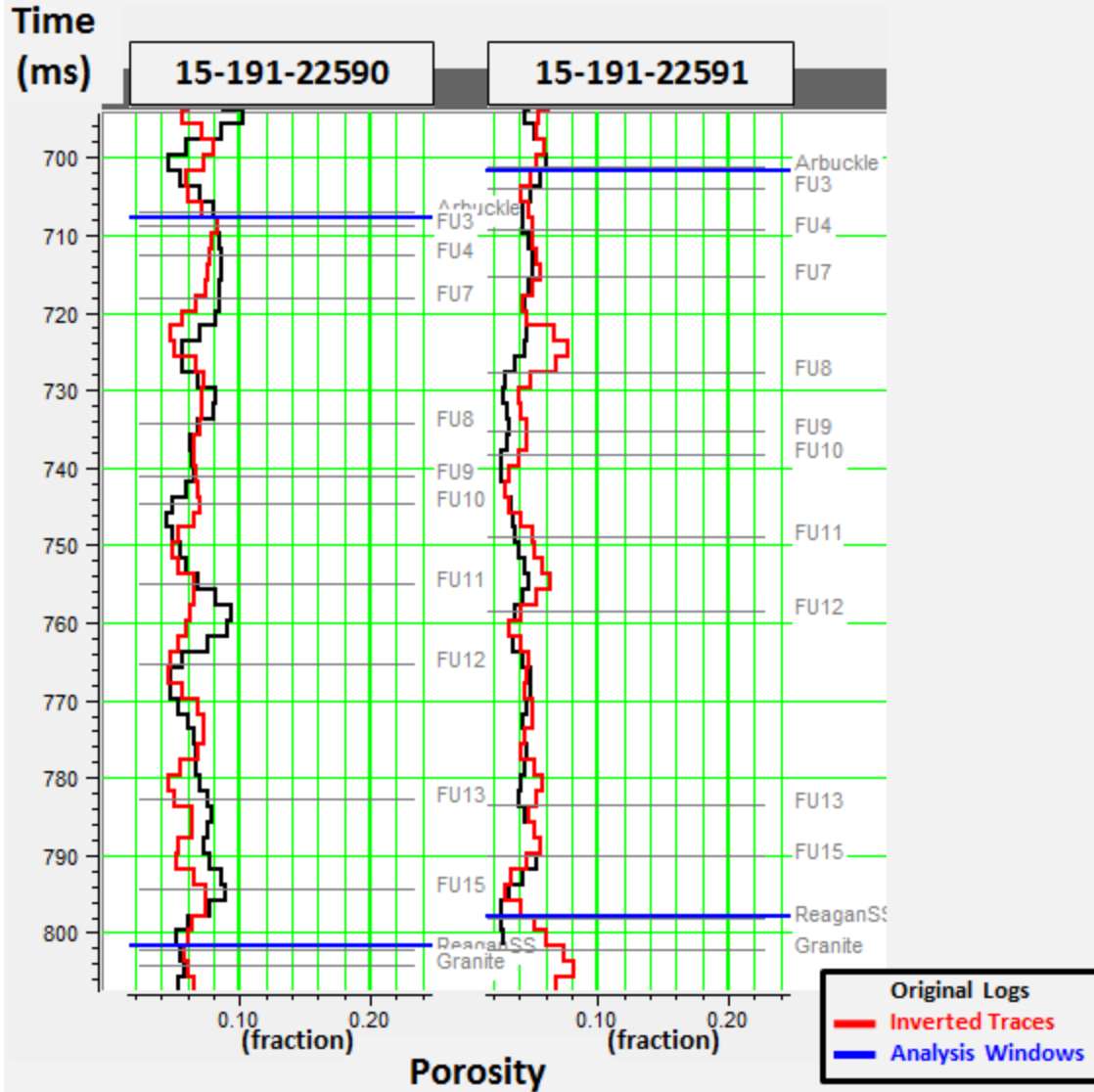
Figure 6.8. Analysis of predicted porosity by the second multi-attribute transform within the Arbuckle Group at wells #15-121-22590 and #15-121-22590. Red curves are predicted porosity traces and black curves are filtered original formation porosity logs. Overall correlation between inverted and original logs is 0.67 for all wells. The total RMS error for all wells is 1.3%.
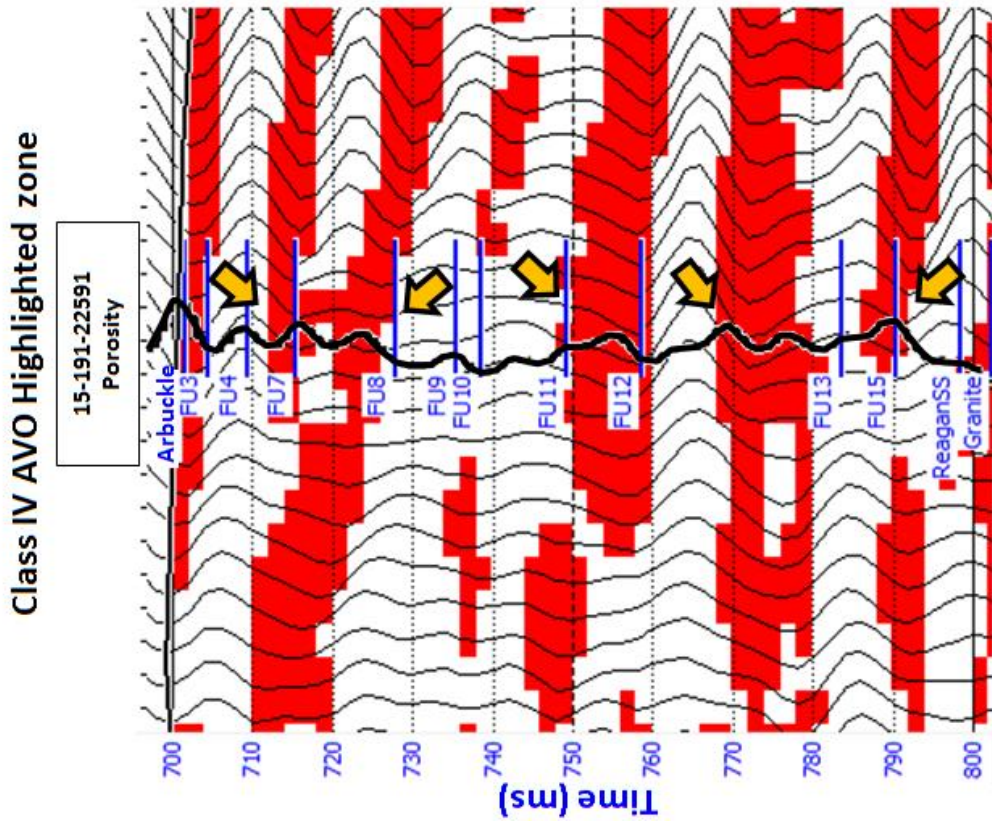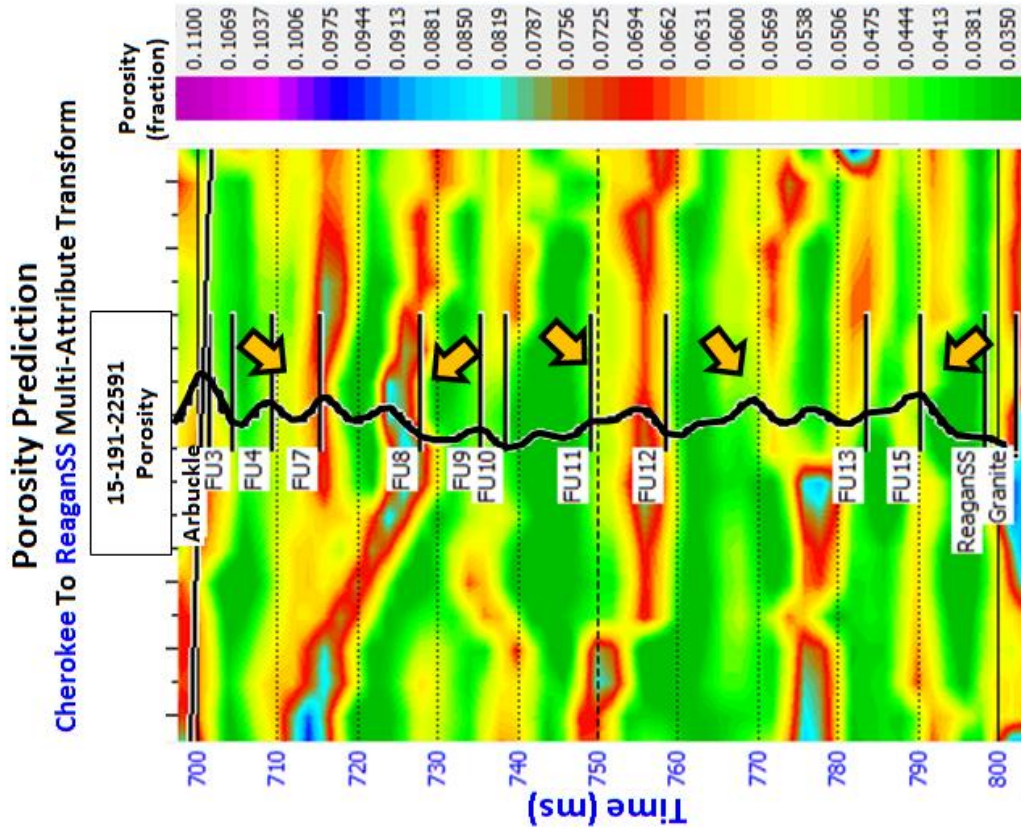
Figure 6.9. (Left) Cross section of Class IV AVO highlighted zone by the A-B crossplotting technique along inline #152. (Right) Cross section of predicted porosity by the second multi-attribute transform along inline #152. The same Class IV AVO highlighted zones show high porosity values in the porosity prediction cross section. Black curves are formation porosity logs of well #15-121-22591.
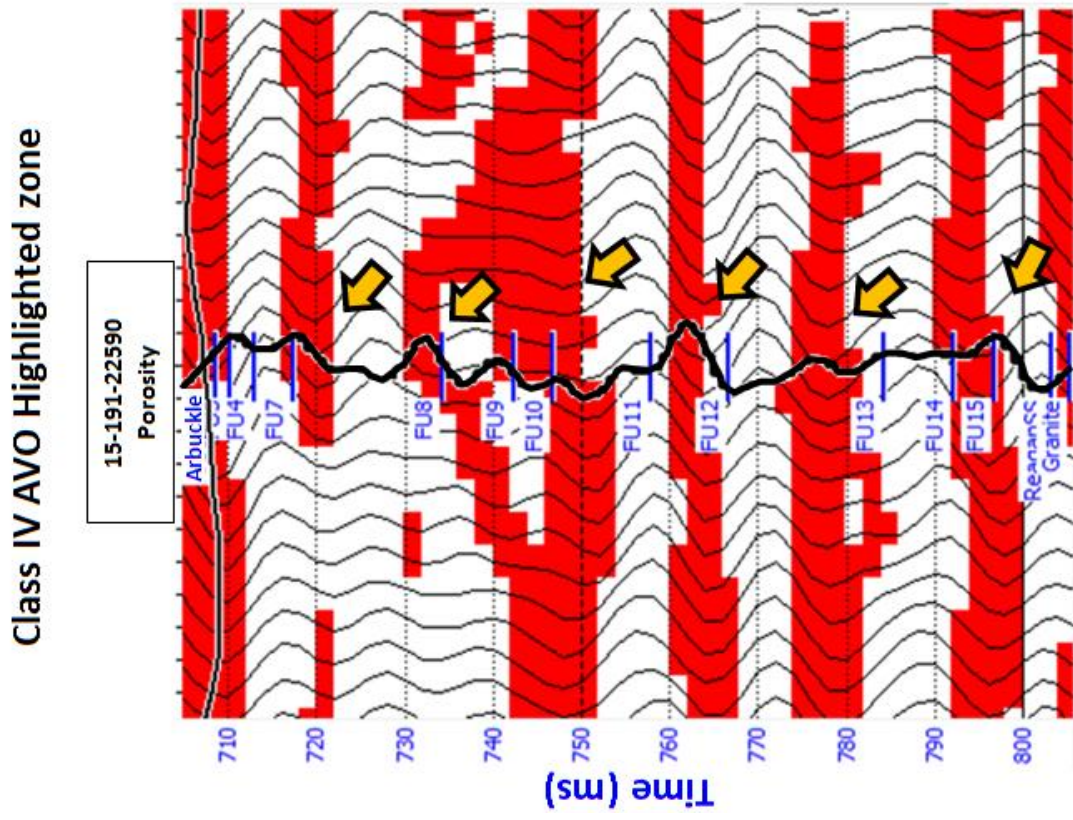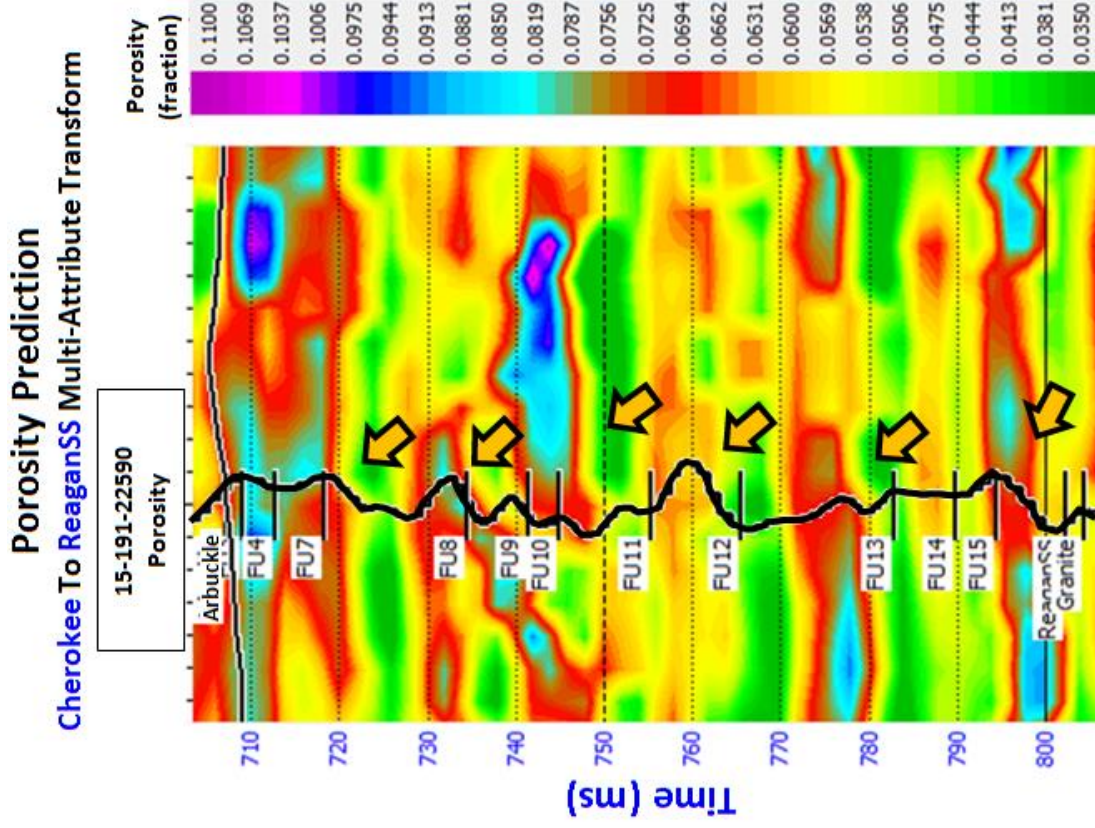
Figure 6.10. (Left) Cross section of Class IV AVO highlighted zones by the A-B crossploting technique along crossline #189. (Right) Cross section of predicted porosity by the second multi-attribute transform along crossline #189. The same Class IV AVO highlighted zones show high porosity values in the porosity prediction cross section. Black curves are formation porosity logs of well #15-121-22590.

CHAPTER 7: CONCLUSIONS

In this study, I employed 3D Pre-stack migrated seismic gathers, post-stack time and depth migrated seismic data, to characterize the Mississippian chert reservoirs and the Arbuckle Group at the Wellington Field. The following conclusions can be drawn from the results presented in the thesis:

1. A post-Mississippian normal fault that is striking NE-SW and dipping SE divides the field diagonally into two parts. This normal fault cuts through the Mississippian and the Arbuckle Group down to the basement. A localized double reflector was developed by the presence of a low impedance layer overlying the Mississippian reservoir that is thick enough to be resolved. This resolvable thickness is attributed to the post-Mississippian normal fault which created more accommodation for thicker sediments to be deposited above the Mississippian reservoir.

2. The good porosity zones in both the Mississippian and the Arbuckle Group exhibit Class IV AVO response which is characterized by negative intercept (A) and positive gradient (B) leading to A-B crossplots located in the fourth quadrant. The A-B crossplotting technique is a powerful technique for identifying reservoirs with good porosity, however, not all high porosity regions are productive due to poor pore connectivity. The A-B crossplotting technique also helps delineate the reservoir top and base.

3. Simultaneous AVO Inversion inverts for P-impedance (Z_P), S-impedance (Z_S) and density (ρ), unlike the post-stack model-based inversion that inverts for P-impedance only. The inverted Z_P by simultaneous AVO Inversion showed better correlation with original P-impedance from well logs and lower RMS inversion error than the inverted P-impedance by the post-stack model-based inversion. Also, Simultaneous AVO Inversion resolved low impedance zones that were not resolved by post-stack model-based inversion.

4. In the Mississippian chert reservoir, Inverted Z_P and Z_S by simultaneous AVO Inversion showed almost similar good inversion quality that depicted the same features in the Mississippian reservoir. The inverted impedances show the expected impedance variation around and within the Mississippian chert reservoir that is characterized by downward gradational porosity decrease, which helps in determining the reservoir top and base except at some places where the overlying layer has impedance values that are equal to the impedance values at the top of the reservoir.

5. Simultaneous AVO Inversion of a variable thickness (wedge) model built at well #15-191-22590 allowed the assessment of vertical resolution of the inversion approach for the gradational impedance increase within the Mississippian reservoir. The Simultaneous AVO Inversion approach recovers reliable impedance information for reservoir thicknesses that are greater than or equal to 10 m, which corresponds to 1/8 of a wavelength.

6. In the Arbuckle, inverted Z_P and Z_S traces at the two well locations that penetrated the Arbuckle showed the same vertical trend that made it easy to trace the tops of the Arbuckle flow units laterally between the different well locations on the inverted data. Generally, the low impedance zones in the inverted Z_P and Z_S volumes show good contrast with the surrounding higher impedance zones, which makes it easy to define and trace the low impedance zones around the Wellington Field.

7. Inverted densities were predicted less reliably than inverted Z_P and Z_S because density recovery mainly depends on the far offset amplitudes that are usually affected by noise and wave attenuation.

8. The well logs have higher resolution than the seismic data due to the difference in frequency content between seismic data and well logs. When the well logs were filtered, inverted traces and filtered well logs showed better agreement, higher correlation, and lower RMS error.

9. For porosity prediction, inverted Z_P and Z_S by simultaneous AVO Inversion were used as external attributes in addition to the internal attributes calculated from the post-stack seismic data by the Hampson Russel EMERGE software. The best porosity prediction within the Mississippian reservoir is achieved when the multi-attribute transform is derived only within the Mississippian reservoir. However, the multi-attribute transform in this case does not provide meaningful porosity values outside the Mississippian reservoir. Using a larger window that includes the surrounding background formation for deriving the multi-attribute transform results in an acceptable porosity prediction within the Mississippian reservoir and around it, which helps identify porosity differences between the Mississippian reservoir and the surrounding formations, and it helps determine the top and the base of the Mississippian reservoir.

10. In the Arbuckle Group, however, a multi-attribute transform that was derived within the Arbuckle Group only provided good porosity prediction at the two well locations that penetrated the Arbuckle, but it did not provide reasonable porosity values away from the two wells. This might be due to limited well control within the Arbuckle. Unlike the Mississippian reservoir, the optimum porosity prediction quality within the Arbuckle was achieved when the multi-attribute transform was derived between the Cherokee Group top and the Reagan Sandstone top using the eleven wells that have formation porosity logs including the wells that did not penetrate the Arbuckle Group.

11. The resultant porosity prediction volume shows good agreement with the results of A-B crossplotting technique for both the Mississippian and the Arbuckle. Class IV AVO zones

highlighted by the A-B crossplotting technique show high porosity values in the porosity prediction volume.

In this study, optimum results using pre-stack data analysis were achieved after careful processing. For valid AVO analysis results, careful processing is extremely important as the amplitude change with offset is very sensitive to noises and processing artifacts. At the beginning of the research, it was frustrating that the real seismic gathers at some well locations did not show the same AVO response as the synthetic seismic gathers built using the well data. It was assumed that the processing operations used to produce the migrated seismic gathers were enough to prepare the data for applying the AVO analysis. However, I identified coherent linear noise that significantly affected the AVO responses. For removing this noise, I used F-K filtering. Also, I needed to apply additional processing operations to compensate for previous processing limitations such as the NMO correction. To perform a reliable AVO analysis, the data needs to be NMO corrected to make the seismic reflections as flat as possible. However, the NMO correction process can have limitations due to the sparse nature of velocity analysis. Also, ignoring higher order terms in NMO correction leaves residual move-out errors (RNMO) that distort the estimation of the gradient and any other related attributes. Therefore, I needed to correct for these errors using the Trim Statics process. I also needed to correct for seismic artifacts caused by previous processing operations. Some seismic operations assume a constant RMS amplitude level from near to far offset even if the amplitude tends to decay with increasing offset resulting in the distortion of the amplitude change with offset. I needed to apply AVO offset scaling to the data for correcting these artifacts and distortions.

Referring to the synthetic seismic gathers to confirm the validity of the real seismic gathers for AVO analysis is an important step since the synthetic gathers give a perfect world

seismic response that is free of noise and processing artifacts. The three important logs for modelling synthetic pre-stack gathers are the P-wave sonic log, S-wave sonic log and density log. The common practice in the industry is measuring P-wave sonic logs and density logs but not S-wave sonic logs. During the research, I compared the modelled S-wave sonic logs with the real measured S-wave sonic logs and there were some differences. Therefore, utilizing S-wave sonic logs is highly recommended for optimum results using AVO analysis.

After applying the additional needed processing operations, we had a volume of seismic gathers with AVO responses that match the responses of synthetic seismic gathers. Also, the different layers started to show consistent AVO responses laterally around the field. This has made it possible to identify the dolomitic reservoirs of the Mississippian and the Arbuckle around the Wellington field based on their AVO response (Class IV). Also, applying the simultaneous AVO inversion to the processed data resulted in reliable impedance volumes that showed good agreement with real well logs. The simultaneous AVO inversion provided better results than the post-stack model based inversion by showing better agreement with well log data. The inversion results were incorporated into the multi-attribute linear regression analysis that allowed the prediction of Mississippian and Arbuckle reservoir porosities and the delineation of the reservoir zones around the Wellington field.

The results of this study will not only benefit similar dolomitic reservoirs that have Class IV AVO response, but also it will help in identifying any type of reservoir whether it is carbonate or clastic that has different AVO response from the surrounding formation after applying careful processing that results in the right AVO responses for the different formations within the seismic volume.

According to the estimated porosity volume, the Mississippian reservoir is thinner in the northwestern part of the Wellington field. Based on well logs, most of the wells located to the northwest of the post-Mississippian fault show thinner Mississippian reservoir overlain by thick reworked Mississippian chert indicating long subaerial exposure. On the other hand, the Mississippian reservoir based on the porosity prediction volume and well logs is thicker to the southeast of the post-Mississippian normal fault, and the well logs show that the Mississippian reservoir is overlain by thinner reworked Mississippian chert indicating shorter subaerial exposure. It can be inferred that after the deposition and the development of the Mississippian reservoir, the post-Mississippian normal fault lowered the southeastern part of the Wellington field area that remained underwater, which helped in the preservation of thicker Mississippian reservoir, while the northwestern part of the Wellington which represents the foot wall of the post-Mississippian normal fault was exposed resulting in the thinning of the Mississippian reservoir by erosion, and the deposition of thicker reworked Mississippian chert. Generally, the porosity prediction volume shows that the Mississippian reservoir in the Wellington field has good porosity across the Wellington field which is consistent with the available formation porosity logs. Therefore, I believe that there is currently enough well control for the Mississippian reservoir in the Wellington field area because there are a large number of wells that penetrate the Mississippian reservoir.

In the Arbuckle Group, there are five main low impedance zones that show high porosity values in the porosity prediction volume, and they show Class IV AVO response. The simultaneous AVO inversion impedance volumes provide better representation of these low impedance zones than inverted impedance by post-stack model based inversion. Therefore, the five porous low impedance zones can be mapped using the inverted impedance volumes by

simultaneous AVO inversion. These zones extend laterally across the Wellington field. They are separated vertically by high impedance and low porosity zones that have some limited low impedance and high porosity pockets. The five porous low impedance zones are almost parallel to each other and have the same geometry trend. They are generally higher in the western and northwestern parts of the Wellington field, and they are deeper in the eastern and southeastern parts of the Wellington field. Therefore, for the CO_2 sequestration plan in the Arbuckle, I recommend drilling wells in the eastern and southeastern parts of the Wellington field. Also, drilling wells in the eastern and southeastern parts of Wellington field provides a higher chance to penetrate thicker Mississippian reservoir. The depth change of the five zones in the Wellington field is attributed to the post-Mississippian normal fault.

Further analysis on the Mississippian and the Arbuckle can be done using PP and PS pre-stack data for finding additional attributes. The joint simultaneous inversion of PP and PS angle gathers method described by Hampson et al. (2013) can be applied for analyzing the Mississippian and the Arbuckle. The joint simultaneous inversion uses both the PP and PS pre-stack data at the same time to invert for P-impedance, S-impedance and density. The inversion results can be evaluated and compared with the current available inverted data of the Wellington field to see if the method can provide better results. Also, the joint simultaneous inversion results can be incorporated in the multi-attribute regression analysis for porosity prediction to see if they can improve the porosity prediction in the Wellington field.

APPENDIX A: F-K Filtering

Low-frequency coherent linear noise was noticed in the seismic gather data (Figure A-1). This kind of noise affects significantly amplitude variation with offset analysis. It made the AVO (Amplitude versus offset) crossplots more scattered and less reliable (Figure A-2). For good AVO analysis, the amplitude variation with offset needs to be as accurate as possible. Therefore, F-K filtering was used to remove this noise. Figure A-3 is a flowchart of F-K filtering. The F-K filter can isolate this low-frequency coherent linear noise from the reflection energy in the (f, k) space. This is done by first transforming the migrated seismic gathers to frequency-wavenumber (f, k) space using the 2-D Fourier Transform (Figure A-4). Then, the low-frequency coherent noise is identified because it becomes clearly isolated from the reflection energy in the (f, k) space. After that, a fan reject zone that includes the noise is defined to zero-out the transform within the reject zone (Figure A-5). Then, the data is transformed back to the time domain by the 2-D inverse Fourier transform resulting in F-K filtered data (Yilmaz O., 1987). The F-K filtering was applied on the Wellington Field data using the Vista processing software. For checking the removed noise, an F-K filtered gather was subtracted from the same gather before F-K filtering to show the removed noise (Figure A-6). After applying the F-K filter, the linear coherent noise was removed, and the AVO crossplots became more closely spaced and more genuine (Figure A-7).
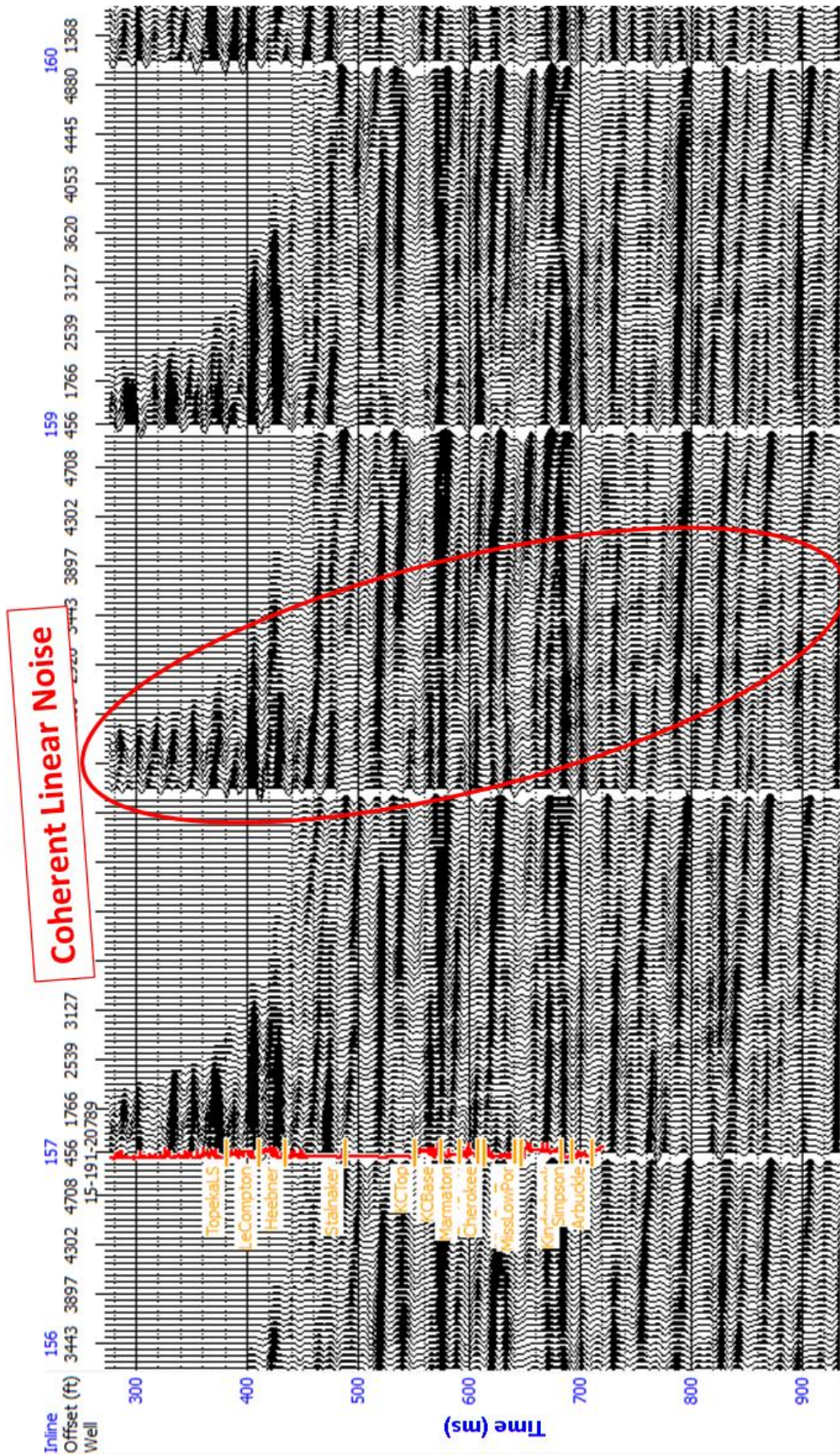
Figure A-1. Migrated seismic gathers at crossline #213. The figure shows the low-frequency coherent linear noise in the seismic gathers.
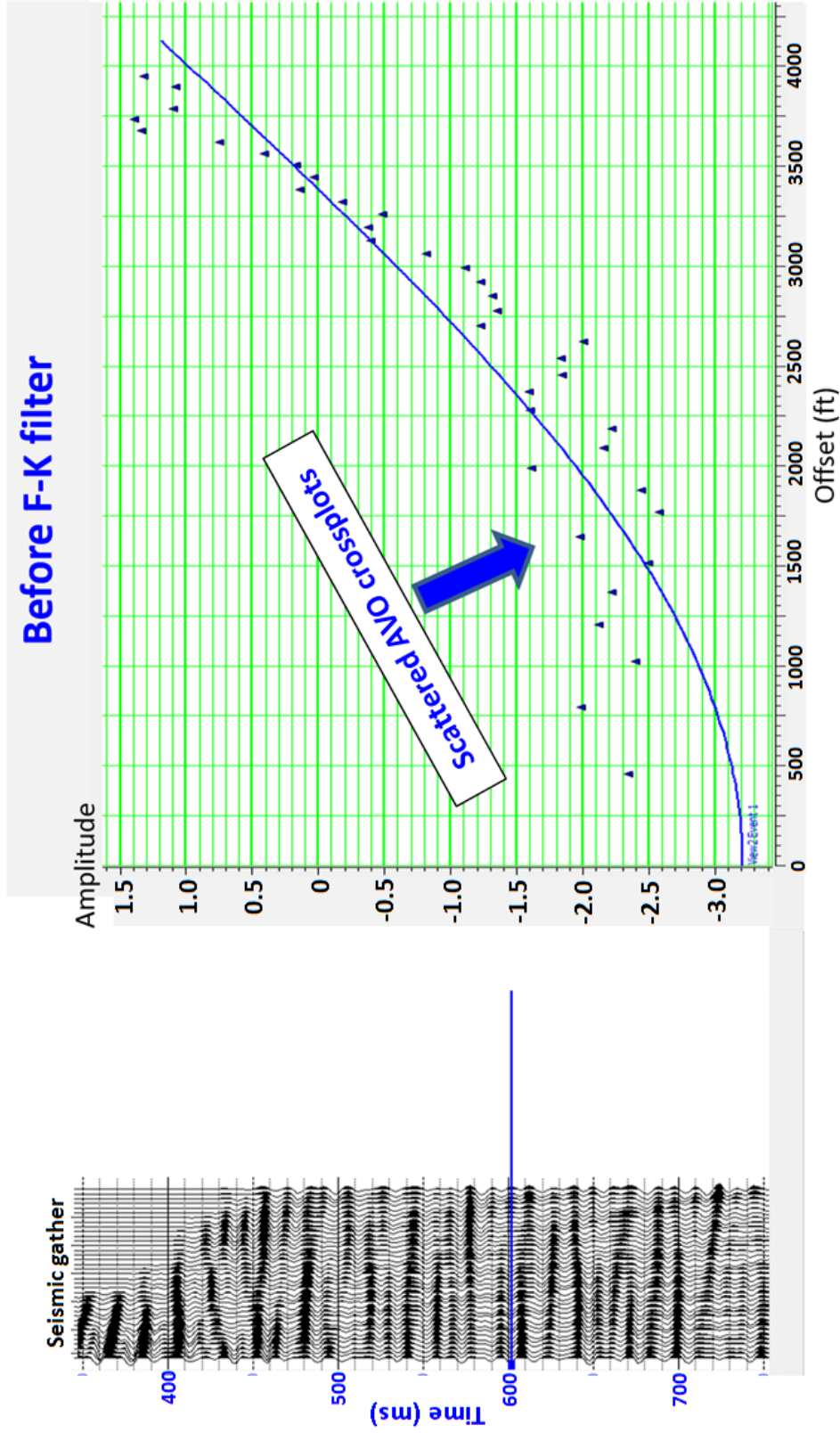
Figure A-2. AVO crossplots of the picked event in the seismic gather to the left that has linear coherent noise. The AVO crossplots are scattered due to the noise.
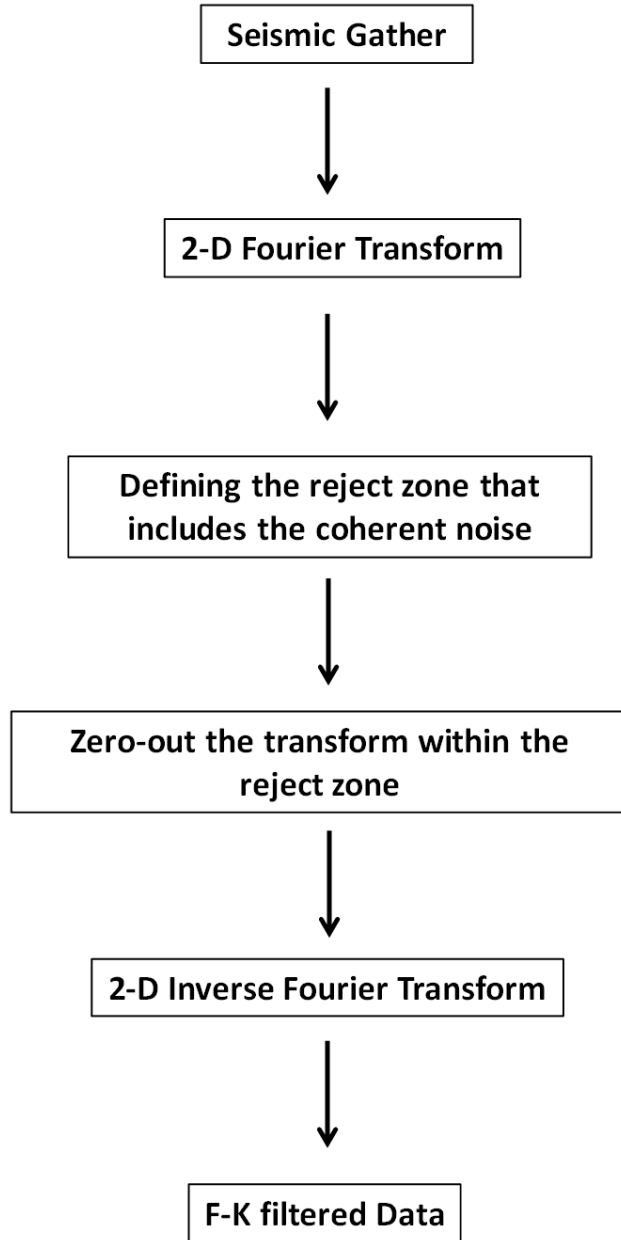
Figure A-3. F-K filtering flow chart. Modified from Yilmaz (1987).

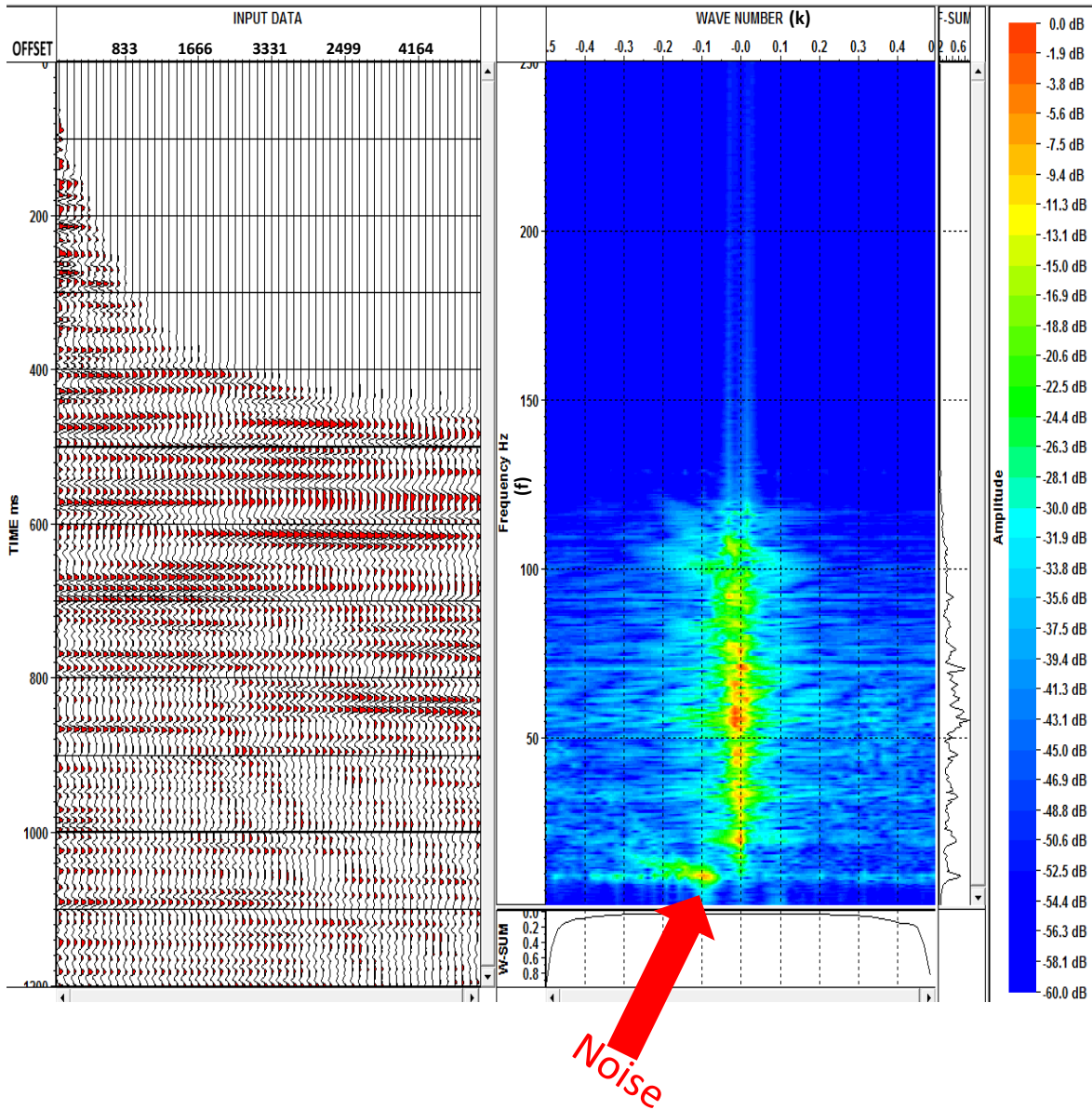Figure A-4. Seismic gather (left) that was transformed from the time domain to the *(f, k)* space (right). The red arrow points at the coherent noise that was successfully isolated from the reflection energy in the *(f, k)* space.
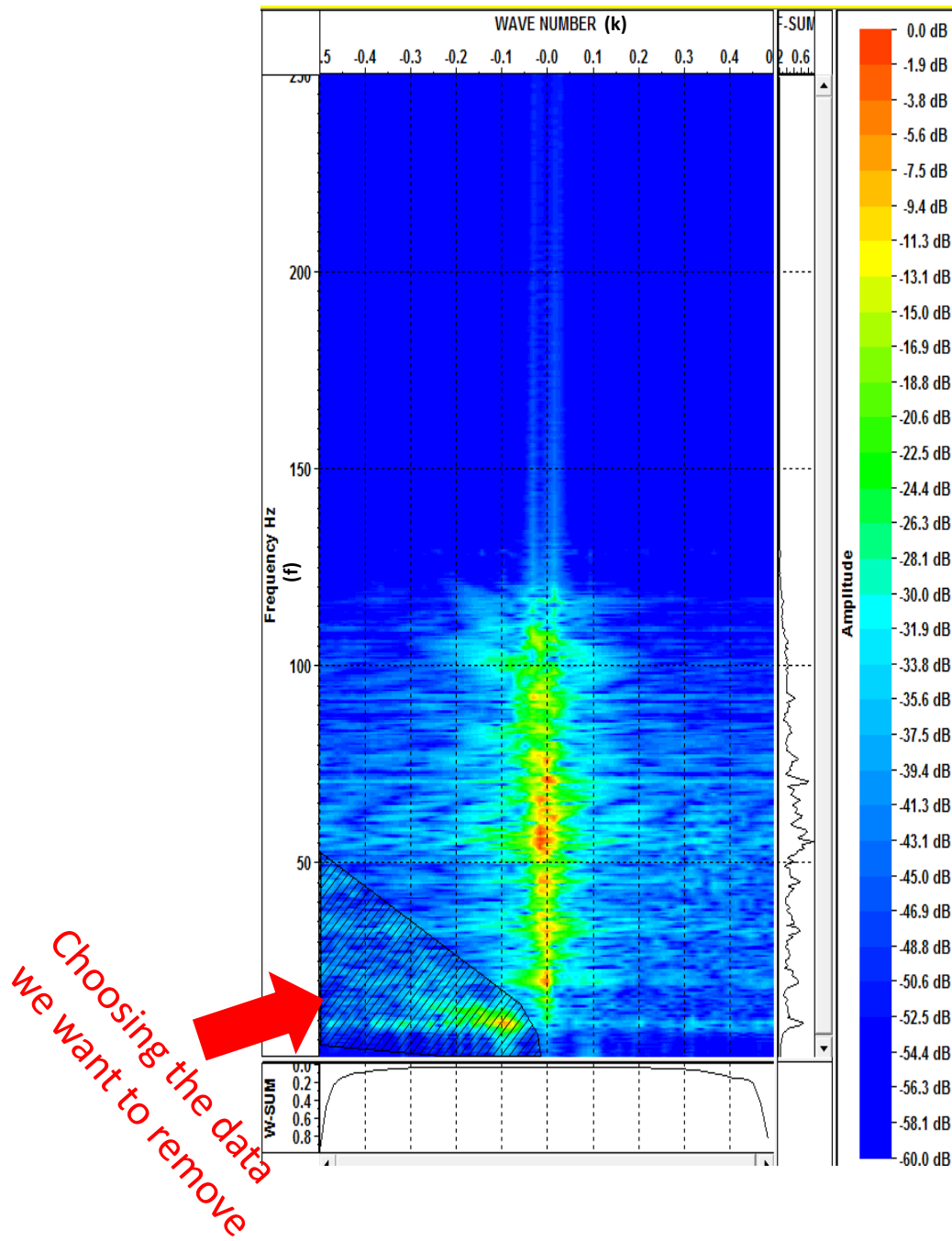
Figure A-5. Defining the reject zone that includes the coherent noise to zero-out the noise in the *(f, k)* space before transforming the data back to the time domain by the 2-D transform.
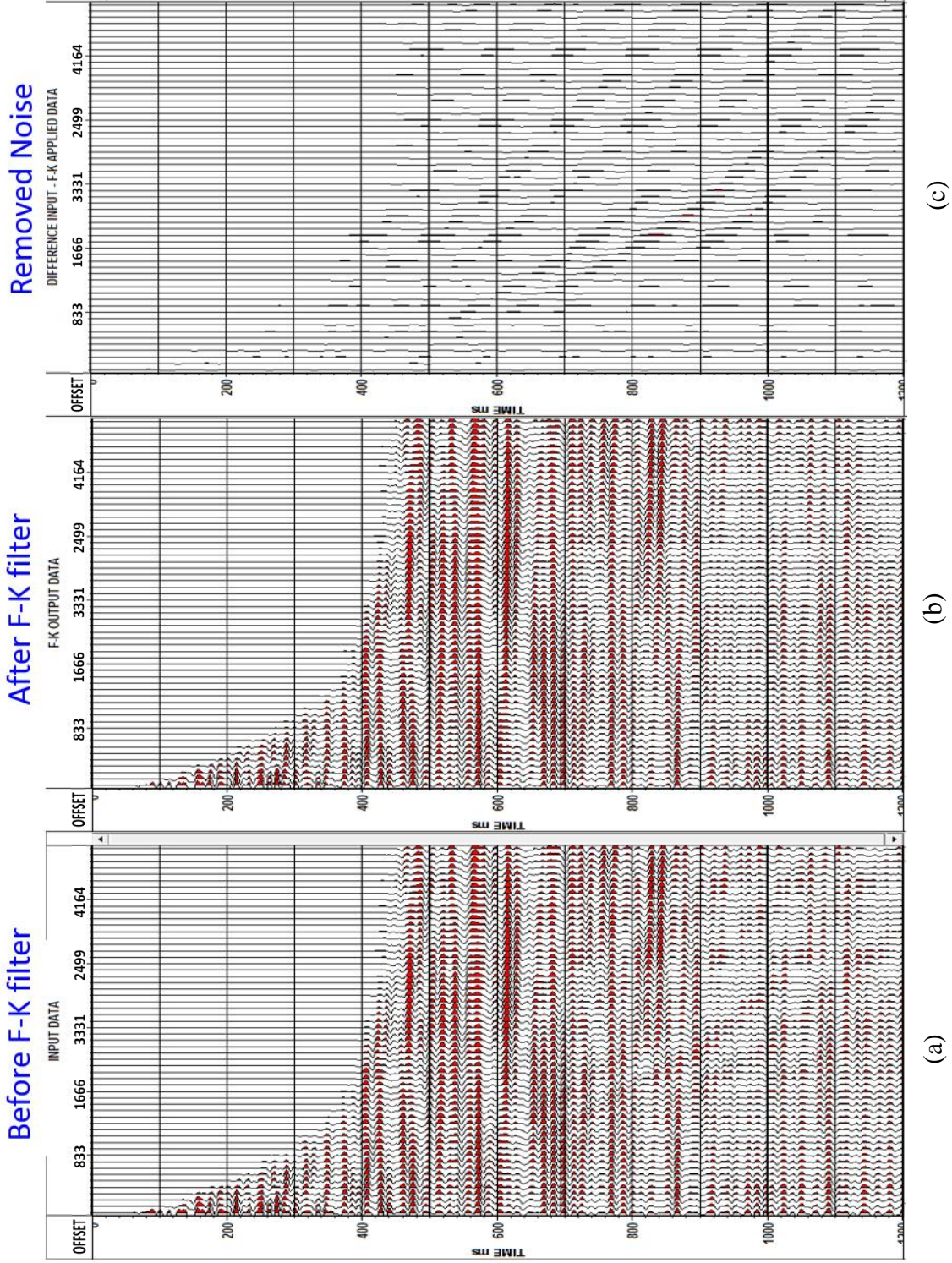
Figure A-6. a) seismic gather before applying the F-K filter. b) Seismic gather after applying the F-K filter. c) removed noise by the F-K filter.

110
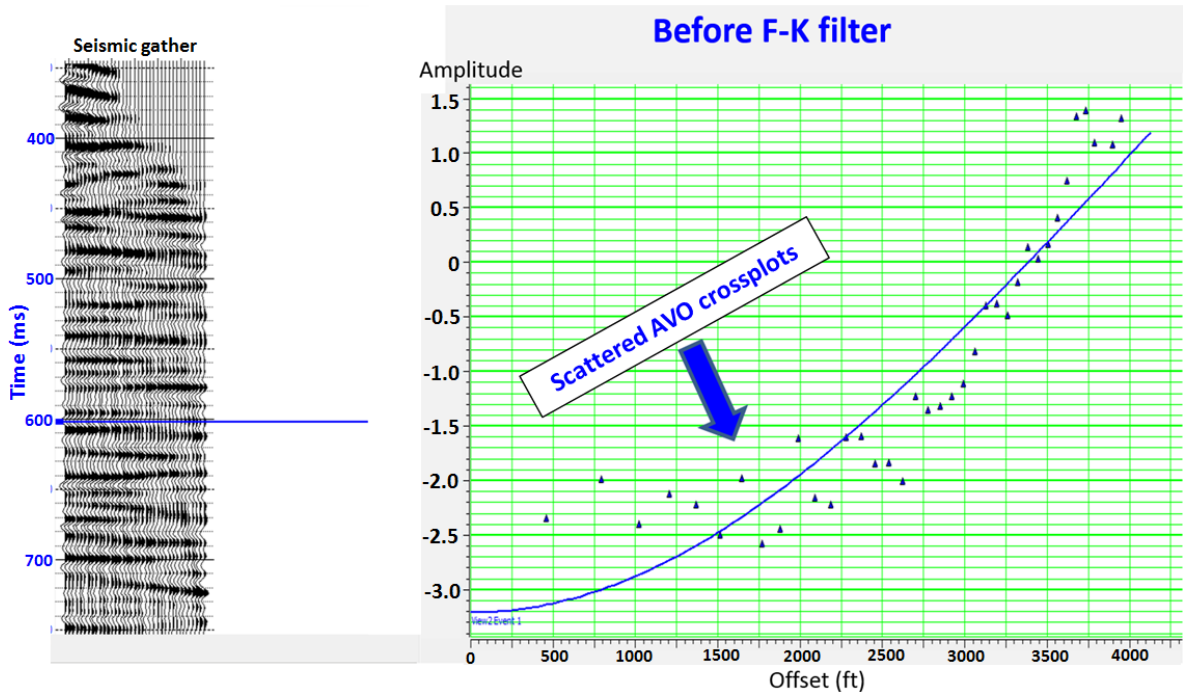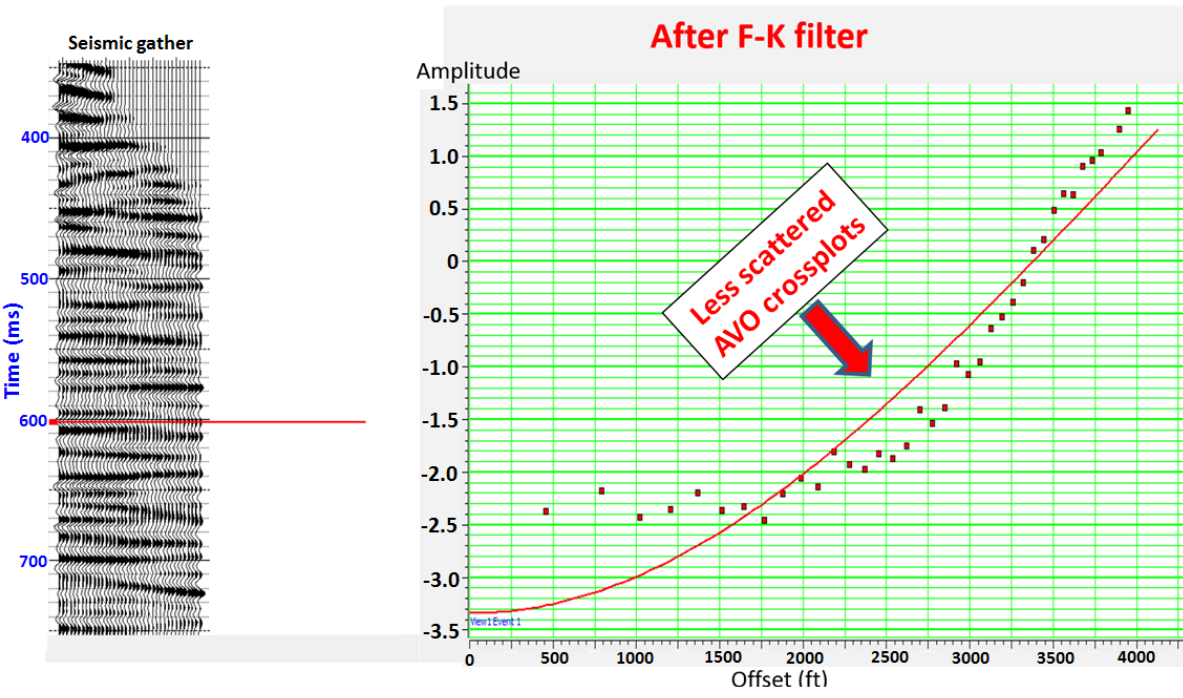
Figure A-7. (a) AVO crossplots of the picked event in the seismic gather to the left before applying the F-K filter. (b) AVO crossplots of the same event after applying the F-K filter. The red AVO crossplots are more closely spaced providing more genuine representation AVO variation.

APPENDIX B: Trim Statics

Trim Statics process corrects for errors on pre-stack seismic gathers that were already NMO corrected. These errors are called RNMO (residual move-out errors). RNMO distorts the estimation of the gradient and any other related attributes (Figure B-1; Ratcliffe et al., 2003). The Trim Statics correction tool available in the Hampson-Russell software creates a pilot trace which is usually the stacked trace of each gather. Then, each trace in the pre-stack gather is correlated with this pilot trace using a group of sliding windows. The cross correlations in each window are used for calculating optimal time shift for that window. Then, the shifts for all the windows are interpolated to make a time-variant stretch of the trace resulting in aligned events (Figure B-2).

(a)   (b)
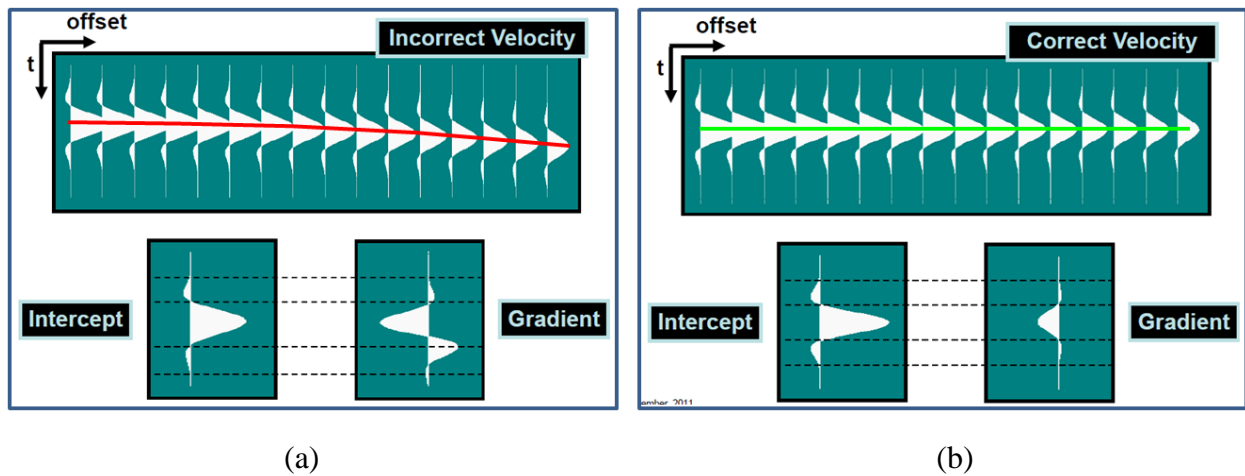
Figure B-1. a) A Reflection event with residual move-out error. b) The reflection event correctly flattened. Notice the difference in intercept and gradient for both events due to the residual move-out error. Modified from Ratcliffe et al. (2003).

(a)   (b)

Figure B-2. Seismic gather at well #15-191-20789. a) Seismic gather before Trim Statics correction with residual move-out. b) Seismic gather after Trim Statics correction with flatter reflections.

APPENDIX C: AVO Offset Scaling

The AVO offset scaling tool available in the Hampson-Russell software corrects for seismic data processing artifacts caused by the previous processing steps because some processing steps usually assume a constant RMS amplitude level from near to far offset even if the amplitude tends to decay with increasi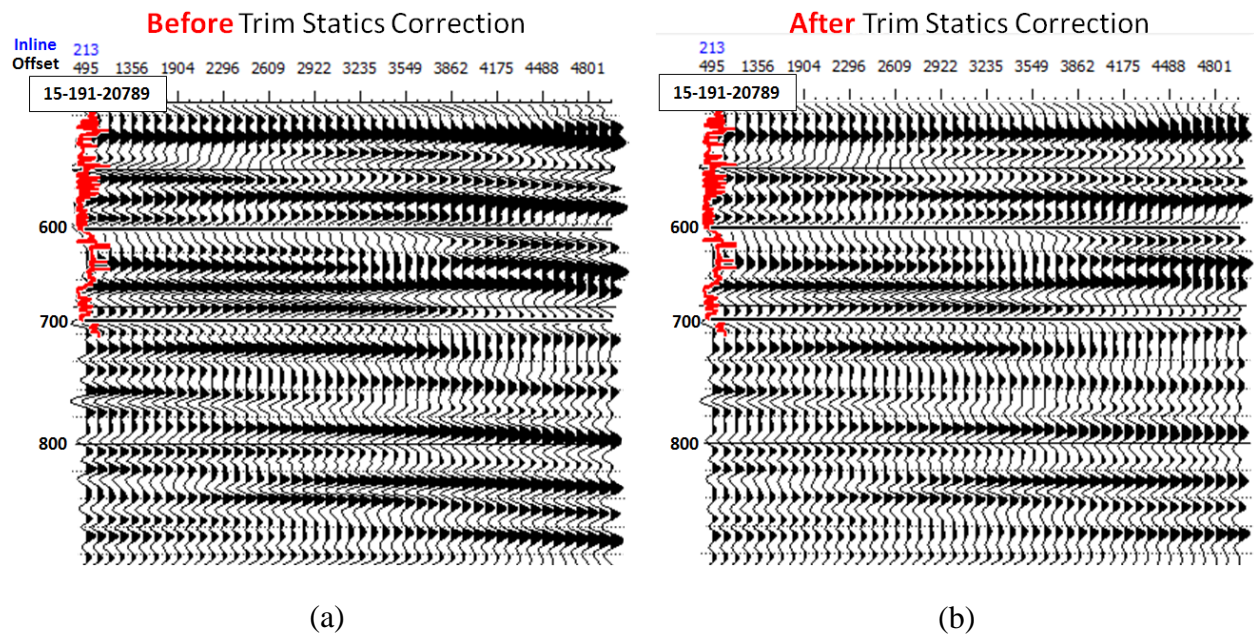ng offset resulting in amplitude change distortion. Also, previous processing steps might have made very little correction or very much overcorrection. AVO offset scaling corrects for these processing artifacts and distortions.

In the AVO offset scaling process, the mean global intercept (A) and gradient (B) is calculated for all real seismic gathers within a non-target zone which was designed to be from 0 ms to 590 ms for the Wellington Field data volume because the Mississippian the Arbuckle is between 620 ms and 820 ms. Also, the mean intercept (A) and gradient (B) for the modeled synthetic offset gather of well #15-191-22591 were calculated for the same time zone. As shown in Figure C-1, the mean gradient trend of the real data does not match the mean gradient of the synthetic model. Therefore, offset dependent scalars are calculated and applied to the real gathers to make the real gathers mean trend match the mean trend of the synthetic gather. Figure C-2 shows that the real gather AVO gradient of the Mississippian reservoir event at well #15-191-22591 has Class III response before AVO offset scaling, unlike the AVO gradient of the same event in the modelled synthetic gather that shows a Class IV response. After AVO offset scaling, the real gather AVO trend of the Mississippian reservoir shows a Class IV AVO response. After applying the AVO offset scaling, the data is ready for inversion and analysis.
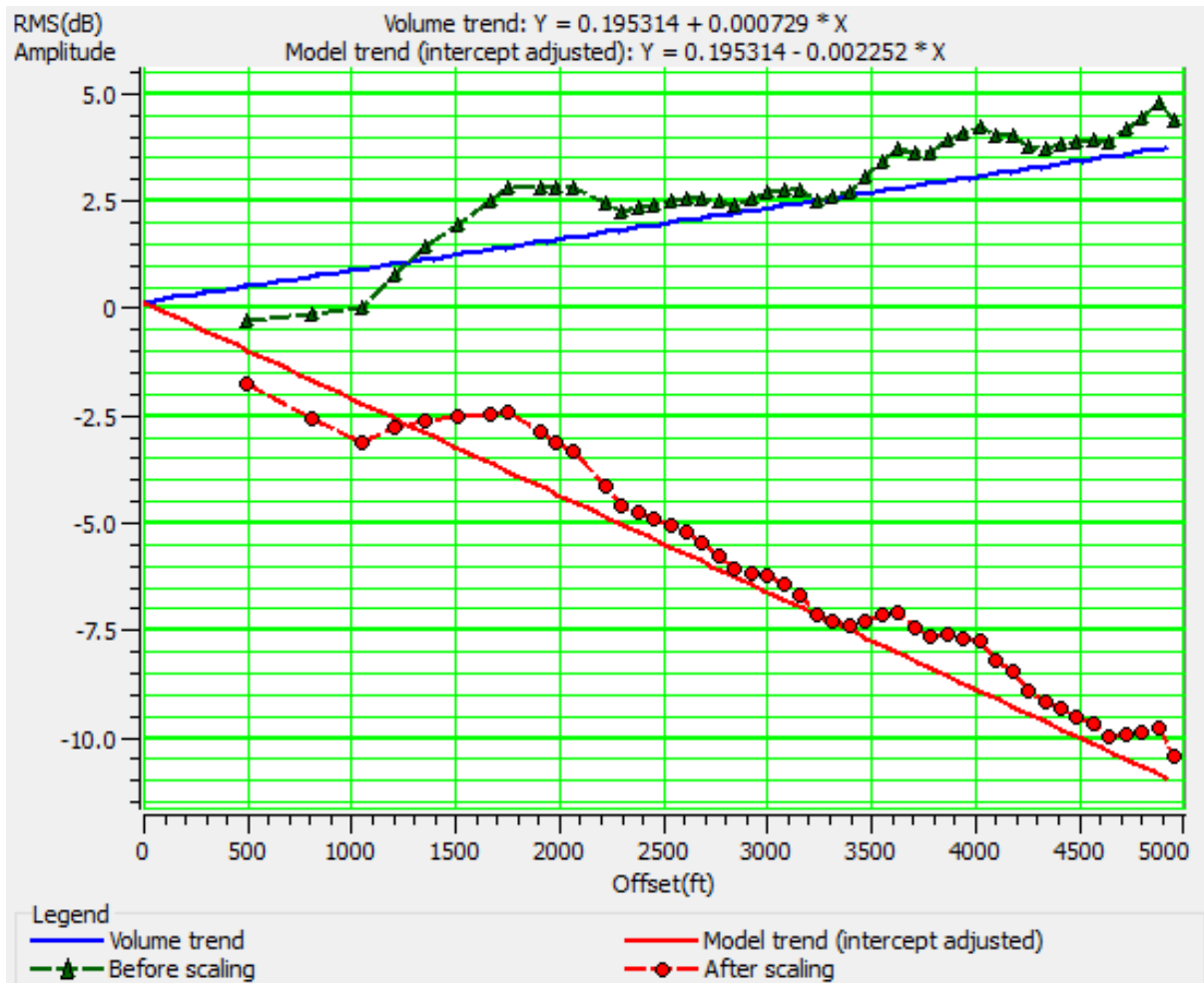
Figure C-1. Mean gradient trend of the real data before AVO offset scaling (green) the mean gradient of the real data after AVO offset scaling (red).
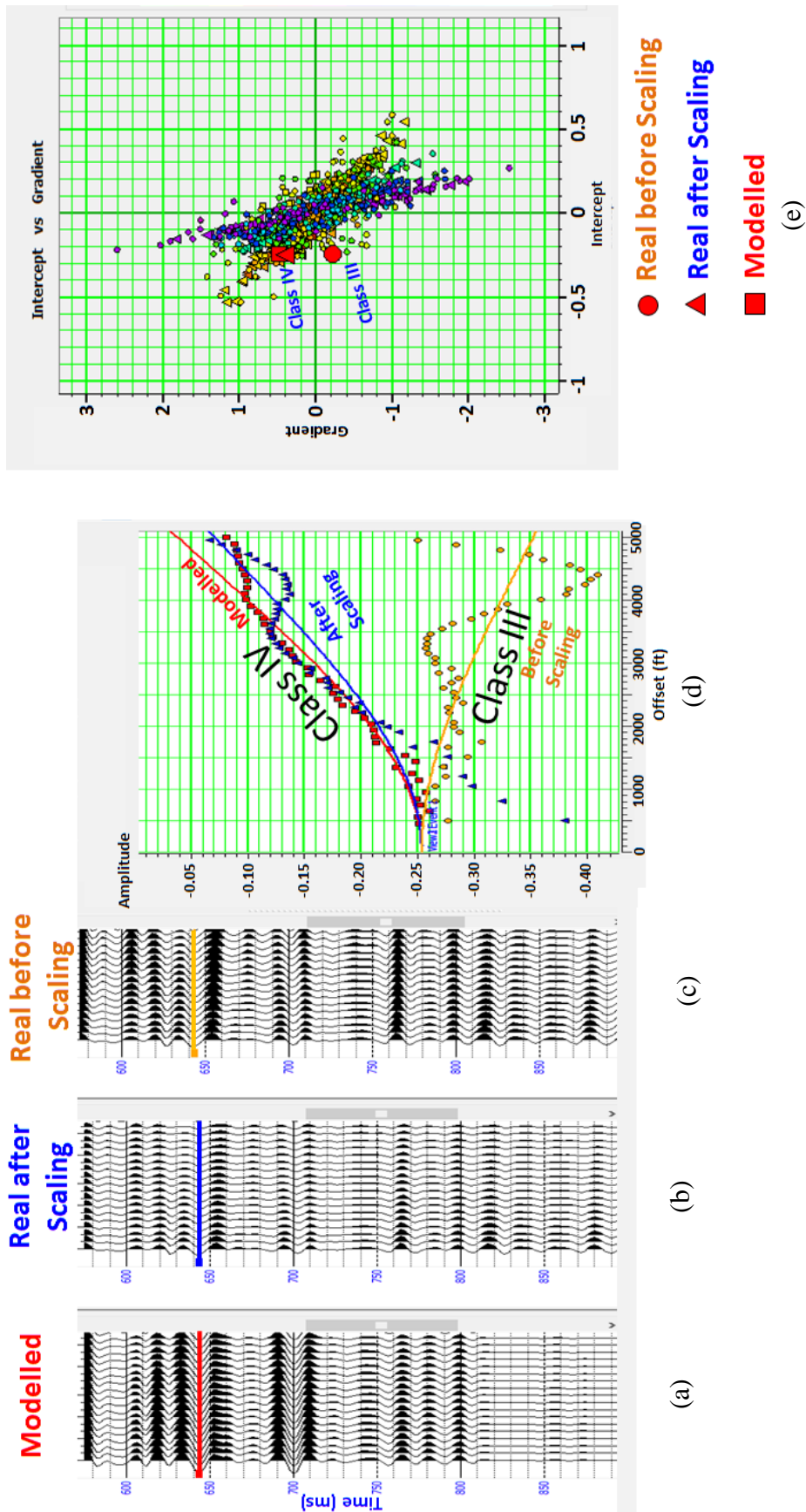
Figure C-2. (a) Modelled synthetic gather of well #15-191-22591. The red line is picking the trough event at the Mississippian reservoir. (b) Real seismic gather after scaling at the location of well #15-191-22591. The blue line is picking the trough event at the Mississippian reservoir. (c) Real seismic gather after scaling at the location of well #15-191-22591. The yellow line is picking the trough event at the Mississippian reservoir. (d) AVO crossplots of the picked traces of the Mississippian reservoir in the gathers. (e) A-B crossplots of the AVO trendlines of the Mississippian reservoir in the synthetic gather, the real gather before scaling, and the real gather after scaling at well #15-191-22591 location.

REFERENCES

Avseth, P., Mukerji, T. and Mavko, G., 2005, Quantitative Seismic Interpretation: Applying rock physics to reduce interpretation risk, Cambridge

Chopra, S., Lines, L., Schmitt, D.R., Batzle, M.L., 2010, Heavy Oils: Reservoir Characterization and Production Monitoring, SEG Geophysical Developments Series No. 13, p.34

Fatti, J. L., P. J. Vail, G. C. Smith, P. J. Strauss, and P. R. Levitt, 1994, Detection of gas in sandstone reservoirs using AVO analysis: A 3D seismic case history using the Geostack technique: Geophysics, 59, 1362–1376.

Franseen, E. K. 2006, Mississippian (Osagean) Shallow-water, mid-latitude siliceous sponge spicule and heterozoan carbonate facies: An example from Kansas with implications for regional controls and distribution of potential reservoir facies: Current Research in Earth Sciences Bulletin 252, part 1.

Franseen, E.K., 2000, A Review of Arbuckle Group Strata in Kansas from a Sedimentologic Perspective: Insights for Future Research from Past and Recent Studies: The Compass, Journal of Earth Sciences Sigma Gamma Epsilon, vol. 75, nos. 2 and 3, p. 68-89.

Franseen, E.K., Byrnes, A.P., Cansler, J. R., Steinhauff, D.M., Carr, T.R., and Dubois, M.K., 2003, Geologic Controls on Variable Character of Arbuckle Reservoirs in Kansas: An Emerging Picture: Kansas Geological Survey Open-file Report 2003-59, 30 p.

Hampson, D. P., Schuelke, J. S., and Quirein, J. A., 2001, Use of multiattribute transforms to predict log properties from seismic data: Geophysics, v. 66, no. 1, p. 220-236.

Hampson, D. P. and Russell, B. H., 2013, Joint simultaneous inversion of PP and PS angle gathers, CSEG Recorder, 38, 32-39

Hampson, D., Russell, B., and Bankhead, B., 2005, Simultaneous inversion of pre-stack seismic data: Ann. Mtg. Abstracts, Society of Exploration Geophysicists.

Jorgensen, D. G., 1989, Paleohydrology of the Anadarko Basin, Central United States. Oklahoma Geological Survey Circular 90: 179-193.

Kalkomey, C. T., 1997, Potential risks when using seismic attributes as predictors of reservoir properties: The Leading Edge, 16, 247–251.

Kansas Geological Survey website, 2014, <http://www.kgs.ku.edu> Accessed June, 2014.

Merriam, D.F., 1963, The geologic history of Kansas: Kansas Geol. Survey, Bull. 162, 317 p.

Montgomery, S. L., Mullarkey, J. C., Longman, M. W., Colleary, W. M., and Rogers, J. P., 1998, Mississippian ―chat‖ reservoirs, south Kansas-Low-resistivity pay in a complex chert reservoir: AAPG Bulletin, v. 82, p. 187-205.

Nissen, S. E., Carr, T. R., Marfurt, K. J., and E. C. Sullivan, 2009, Using 3-D seismic volumetric curvature attributes to identify fracture trends in a depleted Mississippian carbonate reservoir: implications for assessing candidates for CO2 sequestration, in M. Grobe, J. C. Pashin, and R. L. Dodge, eds., Carbon dioxide sequestration in geological media—State of the science: AAPG Studies in Geology 59, p. 297–319.

Rahimpour-Bonab, H., Mehrabi H., Navidtalab, A., Izadi-Mazidi., E., 2012, Flow unit distribution and reservoir modelling in cretaceous carbonates of the Sarvak Formation, Abteymour Oilfield, Dezful Embayment, SW Iran: Journal of Petroleum Geology, v. 35(3), July 2012, p. 213-236

Ratcliffe, A. and Roberts, G., 2003, Robust, automatic, continuous velocity analysis, 73rd Ann. Internat. Mtg.: Soc. of Expl. Geophys., 2080-2083.

Simmons, J.L. and Backus, M.M., 1996, Waveform-based AVO inversion and AVO prediction-error: Geophysics, 61, 1575-1588.

Sirazhiev, A., 2012, Seismic Attribute Analysis of the Mississippian Chert at the Wellington Field, south-central Kansas. University of Kansas master's thesis

Watney, W. L., Rush, J., Wreath, D., Scheffer, A., FazelAlavi, M., Doveton, J., Barker, R., Newell, K. D., Datta, S., Roberts, J. and Fowle, D., 2013, Paleozoic Anchor Core in South-Central Kansas—Berexco Wellington KGS #1-32, Sumner County in Dubois, M.K., and Watney, W.L., conveners, and Tollefson, ed., Mid-continent Core Workshop: from Source to Reservoir to Seal: AAPG Mid-Continent Section Meeting.

Watney, W. L., Guy, W. J., and Byrnes, A. P., 2001, Characterization of the Mississippian chat in south-central Kansas: AAPG Bulletin, v. 85, no.1, p. 85-113.

Yilmaz O., 1987. Seismic Data Processing, Society of Exploration Geophysicists. Tulsa.